



Virginia Commonwealth University
VCU Scholars Compass

Theses and Dissertations

Graduate School

2018

Graphene as a Solid-state Ligand for Palladium Catalyzed Cross-coupling Reactions

Yuan Yang
Virginia Commonwealth University

Follow this and additional works at: <https://scholarscompass.vcu.edu/etd>

 Part of the [Catalysis and Reaction Engineering Commons](#), and the [Nanoscience and Nanotechnology Commons](#)

© Yuan Yang

Downloaded from

<https://scholarscompass.vcu.edu/etd/5488>

This Dissertation is brought to you for free and open access by the Graduate School at VCU Scholars Compass. It has been accepted for inclusion in Theses and Dissertations by an authorized administrator of VCU Scholars Compass. For more information, please contact libcompass@vcu.edu.

© Copyright by Yuan Yang, 2018 All Rights Reserved

Graphene as a Solid-state Ligand for Palladium- Catalyzed Cross-coupling Reactions

A Dissertation Submitted in Partial Fulfillment of the Requirements for the Degree of Doctor of
Philosophy in Chemical Engineering at Virginia Commonwealth University

By

Yuan Yang

Director: B. FRANK GUPTON, PH.D.

Floyd D. Gottwald Jr. Chair and chair, Department of Chemical and Life Science Engineering

Virginia Commonwealth University Richmond, Virginia

April 2018

Contents

List of Figure.....	v
Abstraction.....	ix
Chapter I Introduction	1
1.1 Carbon-carbon cross-coupling reaction	1
1.2 Heterogonous vs. Homogeneous	4
1.3 Solid support catalysts in Suzuki reaction	6
1.4 Use density functional theory (DFT) to understand heterogeneous catalysis.....	9
Chapter II DFT study of the stability of Palladium on graphene catalyst	13
2.1 Introduction.....	13
2.2 Method	15
2.3 Result and discussion.....	15
2.3.1 Stability of free Pd clusters	15
2.3.2 Pd cluster supported on pristine and O, N, B, Si-doped graphene	18
2.3.3 Interaction between Pd clusters and epoxy and hydroxyl group on graphene.....	23
2.3.4 Pd cluster binding to vacancy defects on graphene	25
2.4 Conclusion	33
Chapter III DFT study of the full reaction cycle of Suzuki reaction catalyzed by palladium on graphene catalysyt.....	35
3.1 Introduction.....	35

3.2 Method	36
3.3 Result and discussion.....	37
3.3.1 Activation energy of full reaction cycle of Suzuki reaction	37
3.3.2 Structure effects on the activation energy.....	39
3.3.3 Charge effects on the activation energy.....	45
3.3.4 Bonding and antibonding state effects on the activation energy	48
3.4 Conclusion	50
Chapter IV DFT study of different transition metal clusters supported on defected graphene for cross-coupling reaction	52
4.1 Introduction.....	52
4.2 Method	53
4.3 Result and discussion.....	54
4.3.1 Stability of Ni, Cu, and Fe cluster supported on defected graphene.....	54
4.3.2 Electronic structure change after deposition.....	57
4.3.3 Full reaction cycle of Fe _n , Cu _n , Ni _n clusters catalyzed Suzuki reaction.....	61
4.4 Conclusion	71
Chapter V Pd nanoparticles/clusters supported on graphene as an efficient and sustainable catalyst for Suzuki reaction.....	72
5.1 Introduction.....	72
5.2 Method	73

5.3 Result and discussion.....	78
5.3.1 Synthesis Pd on graphene via different methods	78
5.3.2 Kinetic evaluation and turn over frequency test	81
5.3.3 Heterogeneity test	84
5.3.4 Recyclability test.....	88
5.4 Conclusion	91
Chapter VI Ni-Pd @ Graphene-nanotube hybrids as robust catalysts in cross-coupling reactions	
.....	92
6.1 Introduction.....	92
6.2 Experimental method	94
6.3 Result and discussion.....	94
6.3.1 Synthesis the CNT/GNP support substrate	94
6.3.2 Immobilize the Pd nanoparticle on the Ni-CNT-GNP hybrid	100
6.4 Conclusion	103
Chapter VII Conclusion and direction of future work.....	104
Appendix.....	106
Appendix A The binding energy of Pd ₁₋₄ bound to various sizes and structures of vacancy defected graphene are listed, along with the spin multiplicity.....	106
Appendix B Individual Pd atom charge states in double vacancy defected graphene supported Pd _n clusters (n=1-14)	107

Appendix C Charge state of free and supported Pd _n cluster and phenylboronic acid in transmetallation step.	108
Appendix D Different structure of Pd _n Cluster n=2-14 supported on double vacancy defected graphene. ΔE is the energy difference from the ground state.	110
Appendix E Different structure of Pd _n Cluster n=4-14. ΔE is the energy difference from the ground state.	112
Appendix F Charge state in oxidative addition step.	113
Reference:	115

List of Figures

Figure 1-1 Pharmaceutical application of Suzuki reaction.....	2
Figure 1-2 (A) Cross-coupling reaction catalyzed by Pd catalyst. (B) A number of publication and patents on Cross-coupling reaction.	3
Figure 1-3 Different strategies to immobilize metal on the support substrate.....	6
Figure 1-4 (A) Pd nanoparticle on ordered silica, (B) Pd nanoparticle on γ -alumina, (C) Pd nanoparticle on graphite and (D) Pd nanoparticle on activated carbon.	7
Figure 1-5 Defect site in graphene. (A) Stone-wales defected site. (B) A double vacated defect in graphene.....	10
Figure 1-6 Fe_{13} and Al_{13} clusters supported on single vacancy defected graphene.....	11
Figure Figure 2-1 The ground state atomic structures, magnetic moment and selected bond length of free Pd_{2-14} clusters.....	16
Figure 2-2 Structures, binding energies, and magnetic moments of Pd atom and Pd_n ($n = 2, 3, 4, 5,$ and 13) clusters supported on pristine graphene. The binding energy of the cluster to graphene is calculated as $B_{\text{binding}} = E_{\text{Pd}_n} + E_{\text{(graphene)}} - E_{\text{(Pd+graphene)}}$	19
Figure 2-3 The structures and binding energies of Pristine and B, N, O and doped graphene as well as the structure and binding energies of Pd atom and Pd_{13} cluster supported on Pristine and B, N, O and doped graphene.....	21
Figure 2-4 The structures and binding energies of epoxy and a hydroxyl group on the graphene as well as the structure and binding energies of Pd atom and Pd_{13} cluster to the epoxy and hydroxyl group on the graphene.	23
Figure 2-5 (A) DFT calculations on the magnetic moment and the nature of the polygons around the defected site. (B) HR-TEM image shows double vacancy defect site on graphene. (C) HR-	

TEM images show Stone-Wales defect. (D) TEM images show large voids sizing 1-40 nm in the lattice of graphene.	27
Figure 2-6 Pd ₁₋₅ bound to various size and structure of vacancy defected graphene.....	29
Figure 2-7 Stability cluster of Pd _n bond covalently to defected graphene.....	30
Figure 2-8 Incremental energies of free and supported Pd _n n=1-14 clusters.....	33
Figure 3-1 Reaction mechanism of Suzuki reaction catalyzed by Pd ₄ cluster.....	36
Figure 3-2 (A) Activation energy of free and supported Pd _n clusters (n=1, 4, 13, and 14, and Pd(PMe ₃)) in the three Suzuki reaction steps. (B) Full reaction pathways for Pd ₄ and Pd ₄ /G....	38
Figure 3-3 Pd _n cluster size (A) and coordination (B) effect on activation energy in reductive elimination step. Pd cluster with lower coordination number and the smaller size is relatively more active in this step. (C) Lower coordination of Pd _n clusters (adjacent Pd less than 4) is more active in oxidative addition and reductive elimination step. (D) Higher coordination of Pd _n clusters (adjacent Pd more than 3) is less active in oxidative addition and reductive elimination step.	41
Figure 3-4 The microscopic mechanism of breaking the Br-C bond from the initial state to transition state on the Pd ₄ and Pd ₁₃ clusters.....	42
Figure 3-5 Different coordination of Pd _n cluster with biaryl complexes of Pd ₁ (A), Pd ₄ (B), Pd ₁₃ (C), and supported Pd ₁₃ (D). Fig (E) shows the activation energies for different biaryl-Pd ₄ conformer. And isomerization energy requires transform to another conformer.	43
Figure 3-6 (A) Correlation between initial biaryl-Pd _n binding energy and the activation energy. (B) Correlation between the initial C-C distance of biaryl and activation energy.....	45
Figure 3-7 Charge transfer and activation energy for free and supported Pd _n , and Pd(PMe ₃) during transmetallation step.....	47

Figure 3-8 Charge transfer and activation energy for free and supported Pd_n, and Pd(PMe₃) during (A) transmetallation, (B) oxidative addition and (C) reductive elimination. (D) Enhance Br and P binding energy correlated to the distance from the Pd active site to the lattice of graphene..... 47

Figure 3-9 The 4d Pd atom at the active site, C, and Br orbital electron density of states of the Pd atom at the active site at the transition state of free Pd₄, Pd₁₃ and supported Pd₄ and Pd₁₃ respectively in an oxidative addition reaction. 49

Figure 3-10 Density of States (DOS) and bonding/antibonding orbitals at the transition state for the reductive elimination of Pd₄ and Pd₄/G. (ba= benzoic acid, bz= benzene). 50

Figure 4-1 Binding energies of Au₁₃, Ni₁₃, Fe₁₃, Mo₁₃, Cu₁₃ and Ru₁₃ clusters supported on the double vacancy defect on graphene. 55

Figure 4-2 Structure, selected bond length, binding energies to graphene and density of state of supported Cu₁₃ (A), Ni₁₃ (B), Fe₁₃ (C), and Pd₁₃ (D). Figure (E) shows charge density deformation of the Pd₁₃ cluster before and after deposition on graphene..... 56

Figure 4-3 (A) D band center and the work function of free and supported Fe₁₃, Cu₁₃, Ni₁₃ and Pd₁₃ clusters. (B) D band center shift and work function change as a function of charge flow to graphene after deposit Fe₁₃, Cu₁₃, Ni₁₃ and Pd₁₃ clusters on defected graphene..... 59

Figure 4-4 (A) Bromine and trimethylphosphine binding energy of free and supported Fe₁₃, Cu₁₃, Ni₁₃ and Pd₁₃ clusters correspond to work function of the metal clusters. (B) Bromine and benzoic acid binding energy of free and supported Fe₁₃, Cu₁₃, Ni₁₃ and Pd₁₃ clusters as a function of metal D band center. 60

Figure 4-5 (A) Reaction mechanism of Suzuki reaction. (B) Activation energies of free and supported Fe, Cu, Ni and Pd clusters in full reaction cycle. (C) Structure of intermedia of free and supported Ni ₁₃ cluster.....	62
Figure 4-6 Activation energies of free and supported Fe, Cu, Ni and Pd clusters correspond to work function of the cluster (A) and charge transfer to the 4-bromobenzoic acid reagent in the transition state (B) in oxidative addition step. (C) Metal cluster D band center shifts, bromine binding energy changes and net energy gain changes affect the activation energy of the metal cluster after deposition in oxidative addition step. (D) Activation energies of free and supported Fe, Cu, Ni and Pd clusters correspond to work function of the cluster. The activation energy changes are controlled by metal D band center shift and metal-Br binding energy change after deposition in reductive elimination (E) and transmetallation (F) step.....	65
Figure 4-7 The sterically hindered C ₂ -Ni-Ni-C ₂ structure obstacles the breaking of Br-C bond in the free and supported Ni ₄ cluster.	67
Figure 4-8 The normalized total energies and the atomic structures of the free and supported Ni ₄ clusters in the Suzuki reaction.	68
Figure 4-9 Structure of Pd ₂ Ni ₂ cluster and the two corresponding supported Pd ₂ Ni ₂ clusters.....	70
Figure 5-1 Pd based solid support catalyst conversion at different temperature in Suzuki reaction using 4-bromobenzoic acid and phenylboronic acid.	76
Figure 5-2 TEM image and particle size distribution of Pd/graphene catalyst fabricated by (A) co-reduction method, (B) SEA method and (C) Post solventless microwave heating method (SEA-MW).....	79
Figure 5-3 (A) atomic survey on the surface of Pd/G catalyst measured by x-ray photoelectron spectroscopy. (B) SAED shows the crystalline structure of Pd.....	79

Figure 5-4 TEM images show isolated vacancy defect site on the graphene sheet, vacancy site that accommodating Pd nanoparticles, as well as Pd nanoparticle embedded in the graphene.

Catalyst generated via solventless microwave method..... 81

Figure 5-5 SEM images of commercially available Pd on activated carbon..... 81

Figure 5-6 Activation energy and TOF of the catalysts in Suzuki reaction..... 83

Figure 5-7 Hot filtration test of Pd on graphene catalyst..... 88

Figure 5-8 The model Suzuki reaction tested in the recyclability test..... 89

Figure 5-9 Recyclability of three Pd on graphene catalyst prepared by the different method. 91

Figure 6-1 The strategy of the synthesis of the CNT/GNP hybrid and immobilizing the Pd nanoparticles on the 3-D CNT/GNP substrate..... 94

Figure 6-2 Left figure shows the Ni-graphene mixture after ball milling. Right figures show the growth of carbon nanotube on the graphene under microwave irradiation. 95

Figure 6-3 Fig (A) shows the length of the carbon nanotube as a function of and temperature after 10 mins of the microwave irradiation. Fig (B) shows the length of the carbon nanotube as a function of time after the microwave irradiation at 130 °C..... 96

Figure 6-4 Graphene-carbon nanotube-Ni nanostructure generated using ball milling and domestic microwave. 97

Figure 6-5 Ni@GNP generated using ball milling and domestic microwave. 98

Figure 6-6 XPS result shows the different Ni and Pd peaks in the sample (A) Ni@GNP BM, (B)Ni@GNP BM-KMW2MIN and (C) Pd@CNT-GNP Hydrazine and Microwave reduction 100

Figure 6-7 Model Suzuki reaction catalyzed by the Pd@GNP-CNT catalyst..... 102

Abstraction

GRAPHENE AS A SOLID-STATE LIGAND FOR PALLADIUM-CATALYZED CROSS-COUPLING REACTIONS

By Yuan Yang, Ph.D.

A dissertation submitted in partial fulfillment of the requirements for the degree of Doctor of Philosophy at Virginia Commonwealth University.

Virginia Commonwealth University, 2018

Major Director: B. FRANK GUPTON, PH.D.

Floyd D. Gottwald Jr. Professor and Chair, Department of Chemical and Life Science
Engineering

Virginia Commonwealth University Richmond, Virginia

Palladium-catalyzed carbon-carbon cross-coupling reactions have emerged a broadly useful, selective and widely applicable method to synthesize pharmaceutical active ingredients. As currently practiced in the pharmaceutical industry, homogeneous Pd catalysts are typically used in cross-coupling reactions. The rational development of heterogeneous catalysts for cross-coupling reactions is critical for overcoming the major drawbacks of homogeneous catalysis including difficulties in the separation, purification, and quality control process in drug production. In order to apply heterogeneous catalysis to flow reactors that may overcome this limitation, the catalyst must be strongly bound to a support, highly stable with respect to leaching, and highly active. While the primary role of supports in catalysis has been to anchor metal particles to prevent sintering and leaching, supports can also activate catalytic processes. In this study, by using a

combined theoretical and experimental method, we probed the effect of graphene as support in the complex reaction cycle of Suzuki reactions.

The density functional theory study provides a fundamental understanding of how a graphene support strongly binds the Pd nanoparticles and act as both an efficient charge donor and acceptor in oxidation and reduction reaction steps. Theoretical investigations prove that the Pd-graphene interaction promotes electron flow between the metal cluster and the defected graphene to reduce reaction barrier. The ability for graphene to both accept and donate charge makes graphene an unusually suitable support for multi-step catalytic processes that involve both oxidation and reduction steps. The computer-aided catalyst design with the atomic precise accuracy demonstrates the Pd/graphene catalyst can be further optimized and the first-row transition metal nanoparticles have great potential to replace Pd to catalyze the Suzuki reaction.

The corresponding experimental study shows that the method to immobilize the Pd nanoparticles on the graphene is crucial to increasing the reactivity and stability of the resulted catalyst. A comparison of the activation energy and turn over frequency for a series of supported and homogeneous catalysts indicates that exposing palladium-graphene to defect inducing microwave radiation results in dramatically lower activation energies and higher turnover frequencies. Furthermore, the heterogeneity tests demonstrate the Suzuki reactions are carried out on the surface of the immobilized Pd nanoparticle agreeing with the theoretical results. A method to engineer the 2-D graphene support to a 3-D structure to minimize the re-stacking and agglomeration of the graphene lattice will also be introduced in this study.

Chapter I Introduction

1.1 Carbon-carbon cross-coupling reaction

Chemistry has occupied a unique position in the industrialization of the civilization. The development of the modern catalytic technologies in the chemical industry has fundamentally reformed the life of humanity. Catalysis is the vital technology that allows cost-effective and environmentally benign manufacture (1). Statistics reveal that about 30%-40% global GDP relies on the use of catalysts and 85% of all chemical products include at least one catalytic step in the synthesis processes (2). To the end of the environment protection, one of the fundamental principles of green chemistry is the replacement of stoichiometric reactions with catalytic ones (3).

The importance of catalysis in the pharmaceutical industry has increased steadily over the past two decades owing to the increasing demands for regulatory oversight, environmental protections, and the reduction of costs in drug development and manufacture (3). A variety of materials have been implemented as catalysts in the pharmaceutical industry: metal oxides, metal complexes, acids and bases, organic and inorganic polymers, as well as manifold biocatalysts and photocatalysts. Transition metal catalyzed cross-coupling reactions have produced a collectively broadly useful, selective and widely applicable method to produce the active pharmaceutical ingredients (API) (4). For instance, Singulair is a multi-billion dollar asthma and allergy drug marketed by Merck. Its active ingredient, montelukast sodium, is synthesized via a Heck reaction using aryl-halide catalyzed by a Pd catalyst (5-7). Boscalid, a broadly used fungicide, which also adopted the Suzuki reaction catalyzed by Pd as a key synthetic step is manufactured by BASF for thousands of tons per year (8-10).

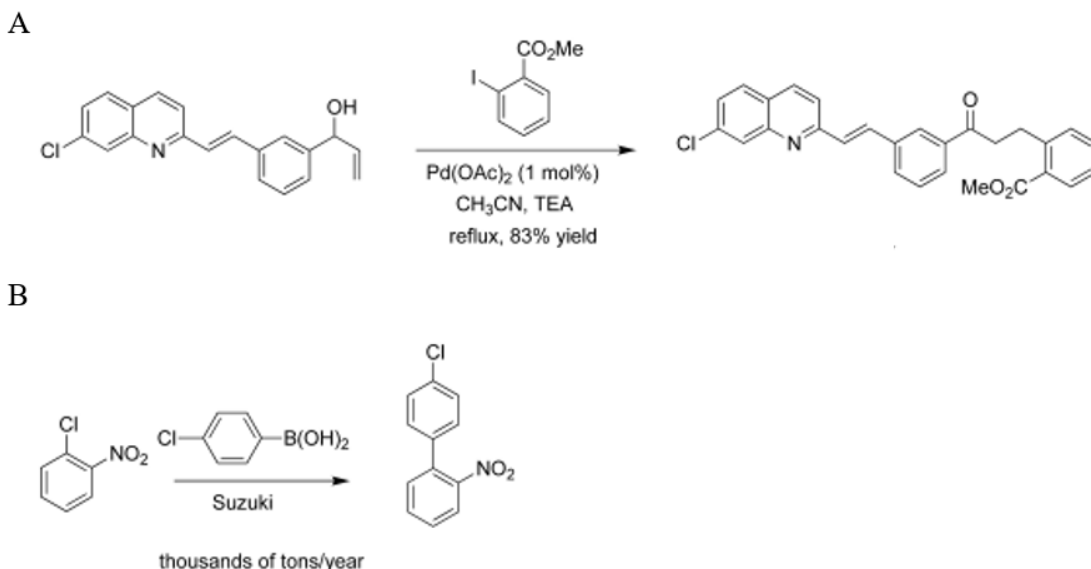
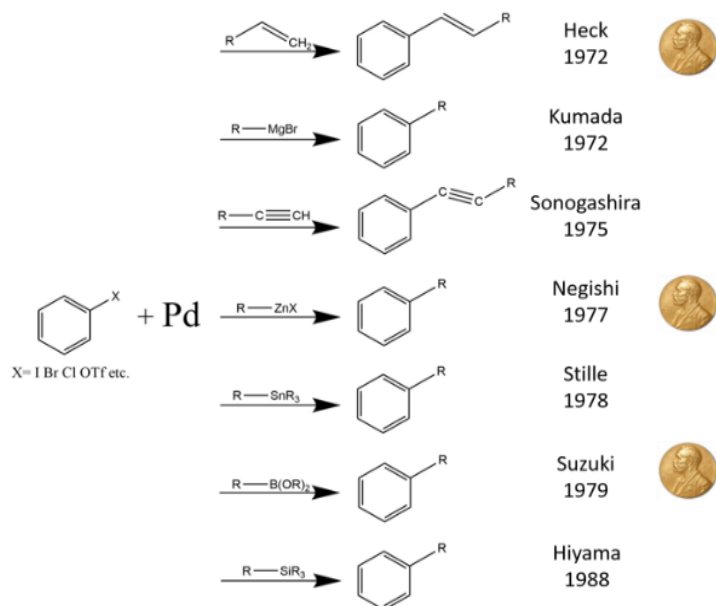


Figure 1-1 Pharmaceutical application of Suzuki reaction. The key steps in the synthesis of (A) montelukast sodium, a multi-billion dollar asthma, and allergy drug, using Heck reaction and (B) Boscalid via Suzuki reaction.

The history of using a transition metal as the catalyst for coupling reaction can be traced back to the late 19th century (11). A well-known example is the Ullmann reaction which converts two equivalents aryl halide to one equivalent biphenyl species via copper catalysis (12-14). Several carbon-heteroatom coupling reactions catalyzed by copper have also been reported in the early 20th century (15). Copper catalysts had dominated the coupling reaction until a copper/palladium catalyst was first introduced to the coupling reaction by Professor Richard Frederick Heck in 1968 (16). Nickel, distinguished by reacting with the Grignard reagent, catalyzed Kumada reaction was also developed at the same time (17, 18). Through the 70s' and 80s', along with the ascent of Pd catalyst and the discovery of using different organometallic reagents, various novel Pd based cross-coupling processes had been discovered, as shown in Fig. 1.2 A (19-26). For their assiduous contribution to the Pd catalyzed C-C bond forming reactions, 2010 Nobel Prize in chemistry was awarded to Professors Richard F. Heck, Akira Suzuki, and Ei-ichi Negishi (27).

A



B

Total number of publications and patents on cross coupling reaction

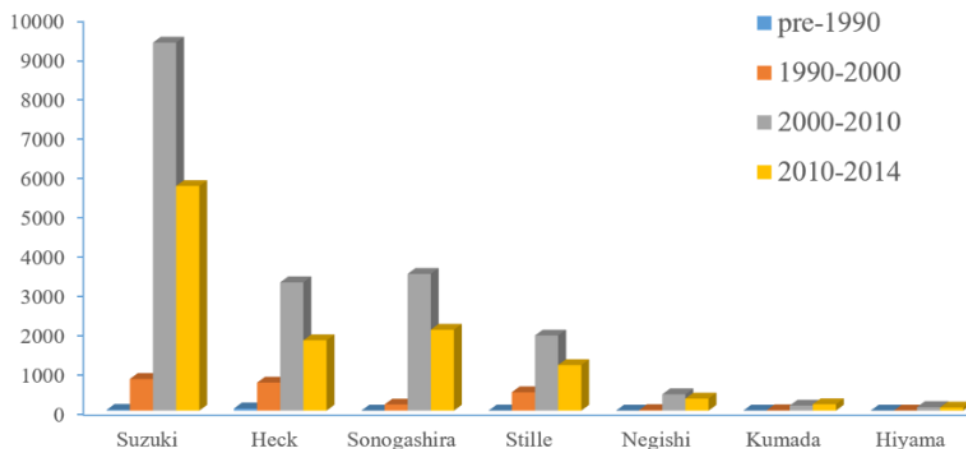


Figure 1-2 (A) Cross-coupling reaction catalyzed by Pd catalyst. (B) A number of publication and patents on Cross-coupling reaction (28).

The development of cross-coupling reactions in the past two decades has made subsequent improvements: more sophisticated ligands design for better reactivity and selectivity, the extension

of coupling substrate scope, a widely functional group tolerance, a fundamental understanding of the reaction mechanism, and environmentally benign processes (29, 30). However, many potential opportunities in cross-coupling reactions are still waiting for the challengers (31). C-H functionalization offers a powerful new strategy in organic synthesis. This new strategy relies on the selected activation of specific C-H bond using transition metals (32). The construction of alkyl-alkyl bond using cross-coupling reaction is another challenge facing the chemical society. The formation of C-C bonds between sp^3 hybridization carbons has been hindered for a long period due to the competitive and facile β -elimination of the alkyl-metal complexes and the control of the stereochemistry (33). Instead of using expensive Pd, developing coupling reactions catalyzed by earth-abundant metal, such as Ni, Cu, and Fe, is also an intense topic in the discovery of new routes of cross-coupling reaction (18, 34-40). Moreover, the rational and effective heterogenization of the non-reusable homogenous Pd catalysts is another topic of great interest in developing novel cross-coupling processes.

1.2 Heterogeneous vs. Homogeneous

As currently practiced in pharmaceutical industry, the cross-coupling reactions typically are implemented by using a homogeneous Pd/ligand catalyst (41). The homogeneous catalysts have been proven to be reactive and efficient for many coupling reactions. And the property of the catalyst can be further tuned by modifying the ligands. The recently developed dialkyl(biaryl)phosphine is a class of phosphine ligands that has been demonstrated to activate highly sterically hindered cross-coupling reagents (42). However, there are several obvious limitations in homogeneous catalysis: the non-reusable nature of the expensive noble metal catalysts and ligands, slow and costly purification and quality control processes are required to remove the metal from the contaminated product in the API manufacture (4, 43-45). Five to ten

units operations are usually required to purify the product to meet FDA standards. Thus, there is a significant demand for effective heterogenization of the Pd catalyst.

Although the exact nature of many heterogeneous catalytic processes remains veiled today, the history of using heterogeneous catalyst is surprisingly long-standing. The first formal scientific records of use heterogeneous metal catalyst were reported by Joseph Priestly and Martinus van Marum separately on the dehydrogenation of ethyl alcohol in the year of 1800, although both of them failed to recognize that metal is the true active species in their catalyst (46). From the dawn of the 20th century, numerous world-known heterogeneously catalytic processes have been developed. Some of those processes had made tremendous impact in the chemical industry since their discovery: Fischer–Tropsch synthesis (FTS), a process which converts H₂ and CO to liquid fuels and valuable chemicals catalyzed by heterogeneous Fe and Co catalyst, and Haber–Bosch process which is an artificial nitrogen fixation reaction to produce fertilizer catalyzed by Fe supported on metal oxides (47-50). Over the past decades, more sophisticated strategies to immobilize the metal onto a solid support have been developed and utilized in the chemical industry. The most widely implemented strategies include covalently or ionically binding the metal complexes to the support, adsorbing metal particles on the support and encapsulating the metal particle into polymer or dendrimer network, as illustrated in Fig 1.3 (46, 51, 52). Immobilizing the metal nanoparticles or clusters onto a supporting substrate is one of the most important approaches to prepare heterogeneous catalysts due to the significant advantages of this strategy which include the versatility for different metals and supports, easy to scale up, and the extraordinary reactivity of the metal nanoparticles. Many synthetic protocols, such as impregnation, precipitation, coprecipitation, adsorption, and ion exchange have been implemented to prepare nanoparticles immobilized on solid support catalyst (46, 51).

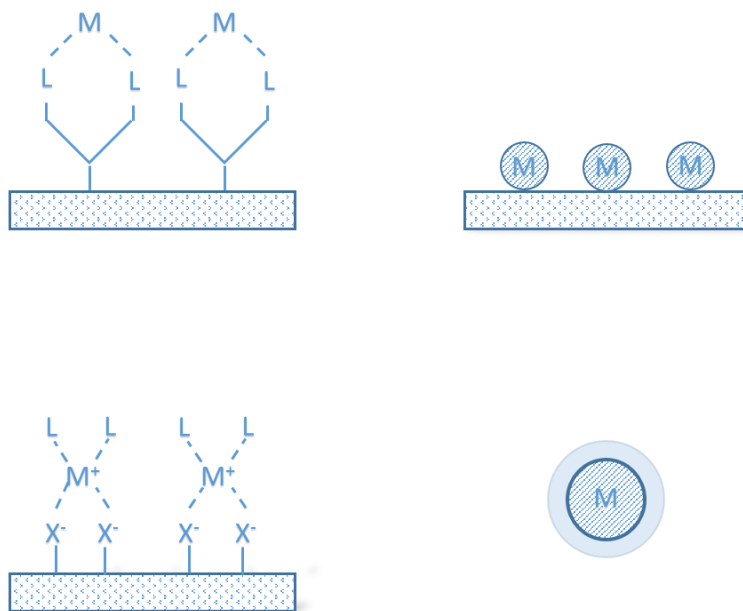


Figure 1-3 Different strategies to immobilize metal on the support substrate.

1.3 Solid support catalysts in Suzuki reaction

A variety of support substrates has been reported to immobilize Pd nanoparticles to prepare the solid-support catalyst. To catalyze the cross-coupling reactions, general support materials to immobilize Pd nanoparticles include carbon-based support (activated carbon, graphite, carbon nanotube, graphene), metal oxide (Al_2O_3 , SiO_2 , MgO , ZnO , TiO_2 , ZrO_2 , NaY , CeO_2), alkali and alkaline earth salts (BaCO_3 , SrCO_3 , CaCO_3 , BaSO_4), Zeolites, polymers, chitosan and other porous materials (53-55). A series of Pd nanoparticles supported on alumina-based catalysts for Suzuki reaction with satisfying yield have been reported by A Gniewek et al (56). Nanoparticles sized between 4-10 nm were successfully obtained and captured on the alumina support. However, no turnover frequency (TOF) or heterogeneity test was reported for the same catalyst. The TOF which is described as molar of product generated by per molar of catalyst in a finite time is an indication of the robustness of the catalyst. Silica as another broadly implemented support material has been reported to immobilize Pd nanoparticles as well as covalently bound Pd complexes. Several reports

indicate that, when covalently bonding Pd complexes with ligands to silica support, the catalysts can provide good yield and selectivity for cross-coupling reaction. Moreover, the heterogeneity test for that catalyst suggested a majority of heterogeneous catalysis in the reaction (57-59). Activated Carbon, generated by further treatment of charcoal to increase porosity, has also been used as support material for decades. Pd nanoparticles supported on activated Carbon catalyst with remarkable turnover frequency was reported by Köhler et al along with the comparison to other five types of support system (55). Scheuermann et al took one more step forward on the carbon-based support system: a novel Pd nanoparticles (4-100 nm) supported on graphite oxide catalyst for Suzuki reaction with 39,000 h⁻¹ TOF was reported (60). Shortly after the Nobel Prize was dedicated to the discovery of graphene in 2010, a new generation of graphene supported Pd nanoparticle catalyst was reported by the Gupton group (61, 62). This novel catalyst is distinguished by the extremely high turnover frequency (230,000 h⁻¹) in catalyzing Suzuki reactions which is at least an order of magnitude higher than other supported Pd catalysts. The remarkable recyclability of the Pd on graphene catalysts is also reported: for a C-H activation reaction, the solid supported catalyst can be recycled more than twenty times without losing the reactivity.

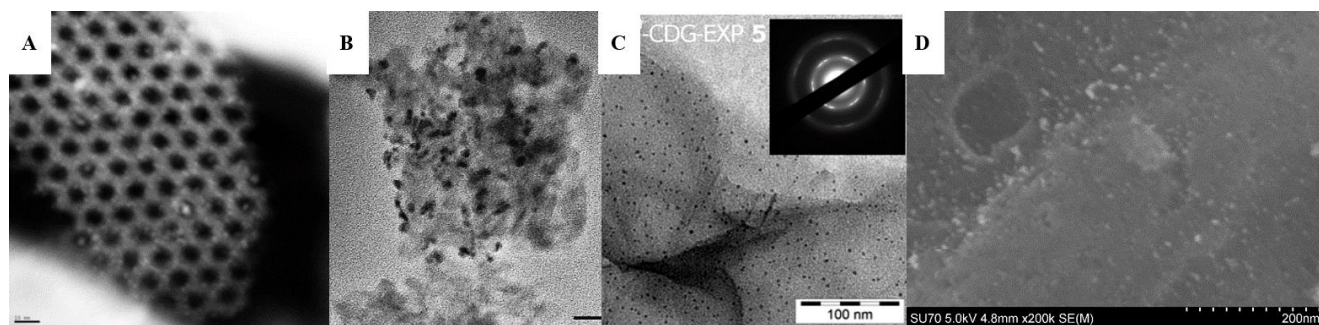


Figure 1-4 (A) Pd nanoparticle on ordered silica, (B) Pd nanoparticle on g-alumina, (C) Pd nanoparticle on graphite and (D) Pd nanoparticle on activated carbon.

A comparison of the reactivity of different supported Pd catalysts in catalyzing Suzuki reaction is shown in the following table by listing the turnover frequencies. The defected graphene supported Pd catalyst exhibits extraordinary catalytic activity. The unconventional heating method used in preparing the catalyst is thought to be one of the key factors that boosted the reactivity of the catalyst. However, the exact active Pd species in the catalytic process is still under debate (43). For several reports, the leached soluble Pd atom or small clusters are thought to be the true active Pd species. Other publications clearly reported the opposite observation that the supported Pd nanoparticle is the genuine active species. It is important to be aware that catalysts with different sizes, shape and supports may not only have dramatically different activities, but these effects may even change whether the catalyst acts as a homogeneous or heterogeneous catalyst. To further optimize the heterogeneous catalyst, it is important to understand the origin of the dramatic variation of catalytic reactivities in different support systems. Several fastidious experiments which use the Pd nanoparticles coated probe tip of atomic force microscope (AFM) as the reaction catalysts were conducted to understand the reaction mechanism in several heterogeneity tests, such as three-phase test, hot filtration test, and poison test, have been developed to address this issue. Other than meticulously designed experiments, computational chemistry is a robust tool study surface interaction and kinetics in catalysis.

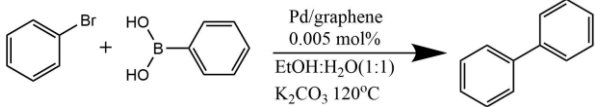
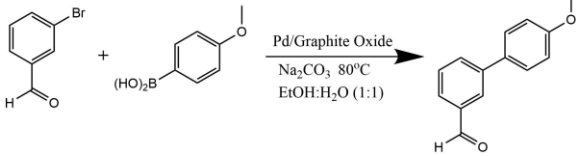
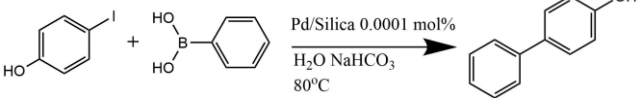
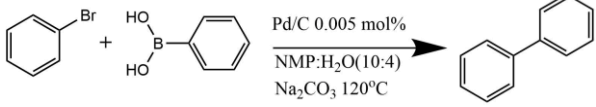
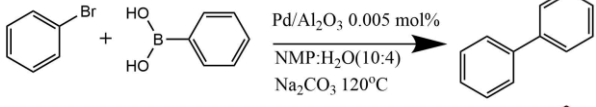
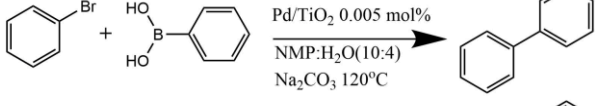
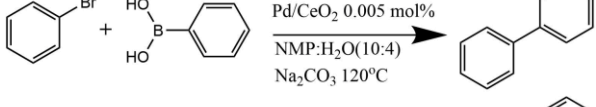
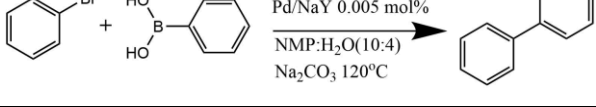
Solid Support	Turnover Frequency (h^{-1})	Reaction Condition
Defected graphene(62)	230,000	
Graphite Oxide(60)	39,000	
Silica(63)	25,000	
Activated Carbon(55)	16,600	
Al ₂ O ₃ (55)	9,600	
TiO ₂ (55)	9,700	
CeO ₂ (55)	4,100	
NaY(55)	4,100	

Table 1.1 Turnover frequency of Pd nanoparticle immobilized on different support substrates in Suzuki reaction.

1.4 Use density functional theory (DFT) to understand heterogeneous catalysis

The study of heterogeneous nanocatalysis is still obstructed in many aspects mainly due to the small size of the nanocatalyst and the complex nature of the heterogeneous catalysis process. The computer-aided theoretical study is an important tool to probe the exact structure of the solid supported nanoparticle catalyst within the atomic-level accuracy and acquire a fundamental understanding of the reaction mechanism of the heterogeneous catalysis. Over the past decade, the theoretical description for surface reaction underwent tremendous growth (64, 65). As the

advancement of density functional theory as well as the calculation capability of modern supercomputers, it is possible for the theoretical calculation to probe the catalytic reaction at surfaces with sufficient accuracy that to compare with experiments result. Density Functional Theory (DFT), as one of the most important *ab initio* methods, has had an immense influence on the identification of the quantum state of atoms, molecules and solid.

The rudiment of DFT was gestated by the theory of Thomas and Fermi after the year of 1927 (66). Modern DFT was established on the Hohenberg-Kohn-Sham theory and the local-density approximation in the 1960s (67). Since then, DFT was not just another way to solve the Schrödinger equation. The use DFT calculations were common in solid state physics. However, it was not until the 90s' when several modern exchange-correlation functionals (GGA and Hybrids) were introduced that DFT was broadly implemented in chemistry. In the new millennium, DFT has become a more powerful tool used in the material science, geology, astrophysics, soil science, protein engineering, and biology.

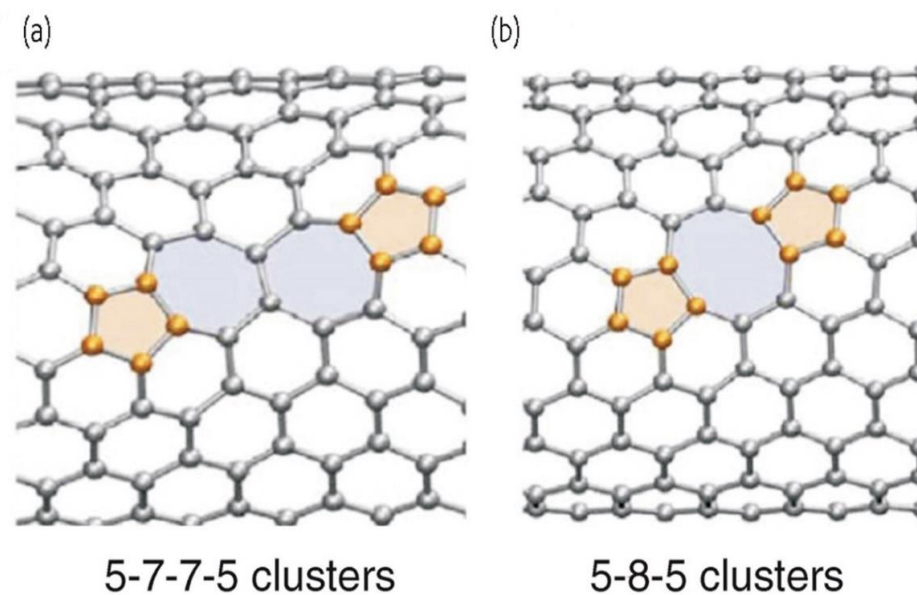


Figure 1-5 Defect site in graphene. (A) Stone-wales defected site. (B) A double vacated defect in graphene (68).

To understand the catalysis process, the DFT calculation can provide valuable insights, such as the electronic structure of catalyst, the presence of the reaction intermediates, kinetic and mechanism of reactions, the coordination of the active site, as well as the function of the support substrates (65). Many problems in the realm of surface catalysis have also been solved through theoretical calculation. Several important studies focused on understanding the selectivity of the reaction (69-72), the trends of catalytic activity of different metals and alloys on the surface (73, 74), and heterogeneous hydrogenation and oxidation reaction (73, 75-78) have been published recently. One of the ultimate goals of the theoretical calculation for surface catalysis is to conduct computer-based catalyst design with predictive catalytic behavior.

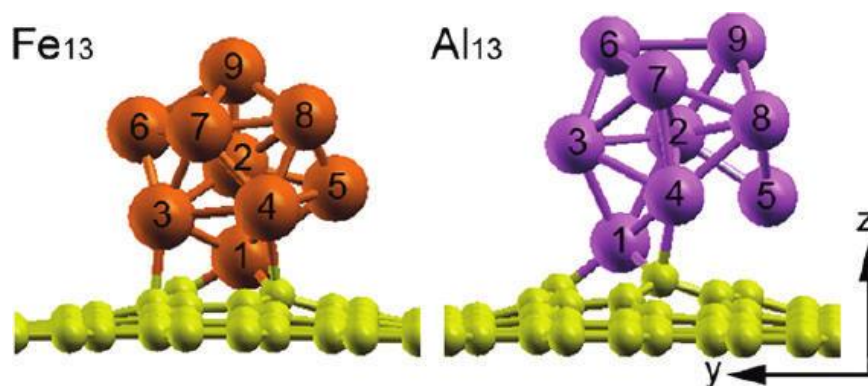


Figure 1-6 Fe₁₃ and Al₁₃ clusters supported on single vacancy defected graphene (79).

To study Pd nanoparticles supported on graphene catalysts using DFT, several previous theoretical works on the property of the graphene, graphene oxide, doped graphene as well as the formation and transformation of a variety of defect sites on graphene have laid the groundwork for this research (68, 80, 81). Since the pristine graphene is almost chemically inert for many reactions, the reactivities of different types of defect sites on the graphene are a key factor that affects the property of graphene. The adsorption of heteroatoms, such as H, O, N, B, F, and S, to the graphene lattice has been well-studied by computational chemists (82, 83). Several theoretical studies also

suggested the presence of the foreign atom impurity and dopant in the graphene endows it with modified electromagnetic, physicochemical, optical, and structural properties (84, 85). For the purpose of using graphene as a support substrate for catalysis, the presence of the impurities is also a critical point to immobilize the metal particles. Different transition metals absorbed on graphene is of particular interest due to the modified catalytic and magnetic properties resulting from graphene-metal interaction (86). A study focused on Fe and Al clusters bound to defected graphene were carried out using DFT. The results indicating a strong interaction between the metal cluster and the graphene support is due to strong hybridization of the nanoparticles with the sp^2 hybridized neighboring carbons near the vacancy. Several studies concentrated on Pd decorated graphene and defected graphene for hydrogen storage were also be published recently (87-90). It is important to note that most of DFT studies can only partially solve the problem with a certain approximation. The corresponding experiments are the key to validate the calculation.

Chapter II DFT study of the stability of Palladium on graphene catalyst

2.1 Introduction

Carbon materials (activated carbon, carbon nanotubes, graphite, and graphene) are widely used as catalyst supports in heterogeneous catalysis for a variety of chemical reactions. This is mostly due to their high surface area, chemical stability, and conductivity (91-94). Only recently has graphene, a two-dimensional carbon lattice, been considered as a potential support system for metal nanoparticles and clusters (60, 95-97). The extraordinary electronic, optical, thermal and mechanical properties, such as high specific surface area ($2630 \text{ m}^2/\text{g}$), high thermal conductivity ($\sim 5000 \text{ W/mK}$), fast charged carrier mobility ($\sim 200\,000 \text{ cm}^2 \text{ V}^{-1}\text{s}^{-1}$) and strong Young's modulus ($\sim 1 \text{ TPa}$), have been well documented (98). Pd nanoparticles supported on graphene (Pd/G) has been reported to be used as a catalyst in cross-coupling reactions. In some examples, the Pd/G nanocatalysts were prepared by employing non-traditional heating methods such as microwave irradiation (MWI) or photo-excitation by laser irradiation (61, 62). Recent research indicates such methods can generate vacancy defect sites in the graphene sheet which could potentially serve as the anchor sites to bind metal particles. In both cases, the catalysts exhibited remarkable catalytic activity as compared to other support systems. Furthermore, negligible metal leaching was observed when these materials were used in Suzuki cross-coupling reactions ($<300 \text{ ppb Pd}$ in the reaction mixture) and the catalysts could be recovered and recycled multiple times without measurable loss of catalytic activity. The enhanced catalytic activity along with the apparently strong binding of Pd clusters to the graphene support suggest that a unique interfacial interaction is occurring between Pd clusters and graphene that is not understood and would benefit from further investigation.

In this chapter, using an *ab initio* DFT method, we investigated the stability of Pd clusters/nanoparticles supported on graphene by different anchoring strategies. Since pristine graphene is stable and almost chemically inert to the binding of metal clusters except at the edges of the graphene lattice, the binding of Pd clusters to a variety of defect sites was performed. Defects are broadly classified as structural defects and impurity defects are a key factor in immobilizing Pd clusters on the graphene surface. Structure defects in crystals (graphene has a crystalline structure) are identified as the disturbance of the crystalline order without the presence of foreign atoms. For a two dimensional graphene lattice, the structure defect includes three forms: 1) Stone-Wales defect which is the rearrangement of sp^2 carbon network to form non-hexagonal rings, 2) single vacancy defect on the graphene which is a zero-dimension defect resulting from the absence of carbon atoms, 3) and stacking faults that extend in two dimensions, while inclusions and voids have a finite size in all three dimensions (80, 99-101). The impurity defect is another class of defect that includes foreign atom substitution and foreign adatom. Graphene doping is an application of foreign atoms substitution to activate the graphene and tune the band gap of the graphene. The broadly-used foreign atom for the graphene doping includes B, N, O, and Si. The foreign adatom is also generally observed in graphene oxide where hydroxyl, epoxy and carboxylic acid functional groups covalently bond to the graphene lattice. In graphene, it is well-known that defects are not stationary and that their migration can have an important influence on the binding of metal clusters. The migration is generally determined by an activation barrier which depends on the defect type and therefore increases exponentially with temperature. As shown in the following section, we compared the stability of Pd atom and clusters bound to pristine graphene, O, N, B, Si-doped graphene, hydroxyl, and epoxy group on the graphene and vacancy defect site of graphene. The

result showed that vacancy defected on graphene can provide the strongest binding to the metal cluster. And the electronic structures of Pd clusters are modified after deposition on graphene.

2.2 Method

The theoretical studies used a gradient corrected density functional proposed by Perdew et al (102). The VASP code was used, and the Kohn–Sham orbitals were expanded using a plane wave basis set and the cutoff was set to 400 eV. The projector-augmented wave method was used to treat electron-ion interactions (103). Van der Waals correction (DFT-D2) was applied (104). A dipole correction was incorporated along the z-axis of the slab, and only a mesh of Gamma point is used for Brillouin zone integration. We carried out geometry optimizations using a conjugate-gradient algorithm, and the structures were not considered optimized until the forces on the atoms were minimized to 0.01 eV/Å or less. Since small Pd_n clusters carry magnetic moments, various spin states were investigated to determine the ground state. Bader charges were used to determine the charge of the individual atoms.

2.3 Result and discussion

2.3.1 Stability of free Pd clusters

Before investigating the interaction between Pd clusters and graphene support, we started the research by understanding the stability and electron structure of free Pd clusters. Fig 2.1 shows the ground states of Pd₂₋₁₄ cluster. We stopped at the fourteenth cluster mainly due to the feasibility and time consumption of the calculation and the fact that Pd₁₄ cluster is approaching the nanometer size which is close to the experimental result. Different possible structures were also calculated. The non-ground state structures and energies are listed in the appendix. We then calculated the average binding energy (ABE) per atom using the expression

$$\text{Avg} = (nE(\text{Pd}) - E(\text{Pd}_n))/n$$

where $E(\text{Pd}_n)$ is the total energy of the cluster of n atoms, and $E(\text{Pd})$ is the atomic energy. We also calculated the vertical ionization potential (VIP)

$$\text{VIP} = E(\text{Pd}_n^+) - E(\text{Pd}_n)$$

as the difference in energy between the ground state of the neutral and that of the cation in the neutral ground state geometry. The results of different binding energies are shown in Tab. 2.1.

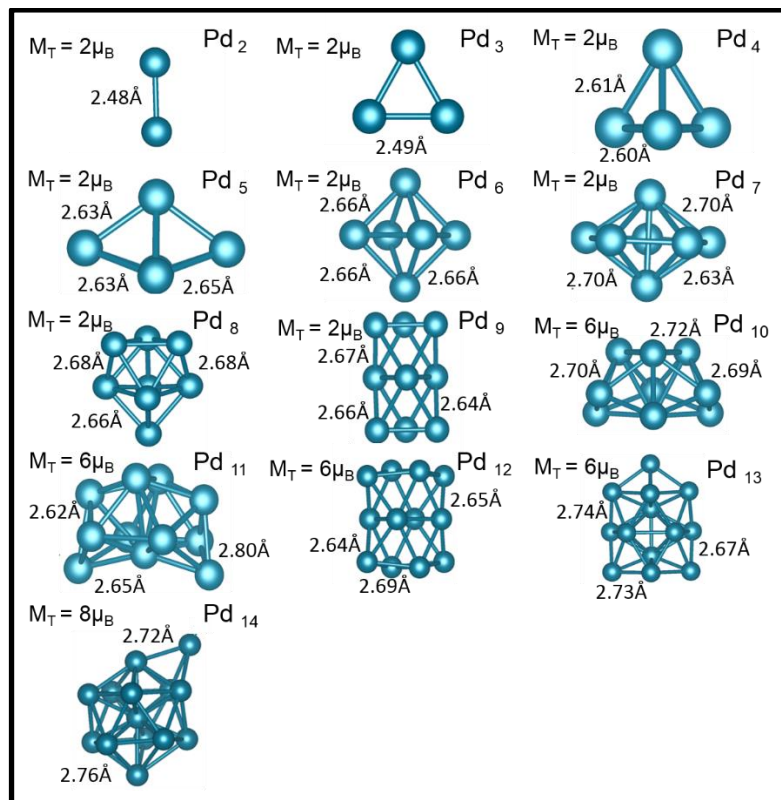


Figure Figure 2-1 The ground state atomic structures, magnetic moment and selected bond length of free Pd₂₋₁₄ clusters.

Pd cluster	Avg. Binding energy (eV)	Spin multiplicity	Ionization potential (eV)
1	-	1	8.80
2	0.65	3	7.77
3	1.27	3	7.81
4	1.68	3	6.78
5	1.81	3	6.62
6	1.89	3	6.41
7	2.01	3	6.37
8	2.11	3	6.18
9	2.20	3	6.15
10	2.24	7	6.19
11	2.29	7	6.22
12	2.35	7	6.21
13	2.41	7	5.95
14	2.43	9	5.91

Table 2.1 Average binding energy, spin multiplicity and the vertical ionization potential of Pd₁₋₁₄ cluster are listed.

The results suggest the average binding energies are increased as the number of atoms increasing in the cluster which indicates large clusters and nanoparticles are generally more stable than small ones. However, certain cluster Pd_n with specific size and structure may be significantly more stable than its neighboring Pd_{n-1} and Pd_{n+1} clusters. While Pd atom and bulk Pd possess no magnetic moment, small clusters carry certain Spin multiplicities and the magnetic moment of the small clusters escalates from two to six as the number of atoms in the cluster increased from nine to ten. It is important to note that the Spin multiplicities of the clusters are not only controlled by the size of the cluster. Different structures of the Pd_n cluster also affect the unpaired electrons in the cluster. The vertical ionization potentials of clusters indicate the energy difference between a neutral cluster and a cation cluster, which is an important parameter in understanding the reactivity and chemical hardness of the material. Considering the incremental energies of the Pd_n clusters, the relatively more stable clusters are Pd₄, Pd₆ and Pd₁₃. It is important to note that the ground state of the Pd₁₃ cluster is a bilayer structure. The total energy of icosahedron Pd₁₃ (*105*, *106*), which

has been considered as a ground state by many previous researchers, is 0.21 eV higher than the bi-layer ground state.

2.3.2 Pd cluster supported on pristine and O, N, B, Si-doped graphene

Due to the chemical inertness of the pristine graphene, it is more difficult to integrate metal nanoparticles with the surface of the pristine graphene than immobilizing metal nanoparticles to graphene oxide or heteroatom-doped graphene. However, use pristine graphene as support to integrate metal nanoparticle still attract considerable attention, since graphene oxide has lower electronic conductivity resulting from the presence of heteroatom sp^3 hybridization sites disrupts the perfectly ordered sp^2 arrangement of carbon atoms in the graphitic system. Several studies reported the successfully immobilizing of the Cu, Ag, Au, and Pd nanoparticles on pristine graphene and the excellent reusability of the supported system (107-109).

One of the most efficient methods to modify the reactivity of the pristine graphene as well as tailor its electronic, optical and mechanical property towards specific application is through heteroatom doping the graphene. Si, O, N, and B are the most widely used heteroatom for such application. Previously reported using direct synthesis method or post-treatment method to dope the pristine graphene. In the direct synthesis method, the heteroatoms were introduced to the system before the fabrication of the graphene. In contrast, in the post-treatment method, the pristine graphene was fabricated first, and the doping agents were chemically induced to the pristine graphene. The post-treatment method is a versatile and facile protocol that can be further categorized into wet doping and dry doping. Two types of doped graphene, p-type or n-type, can be achieved by using different dopants. The doped graphene has been extensively studied and applied in the field of sensors, semiconductor, fuel cell, hydrogen storage and heterogeneous catalysis (82, 110-112).

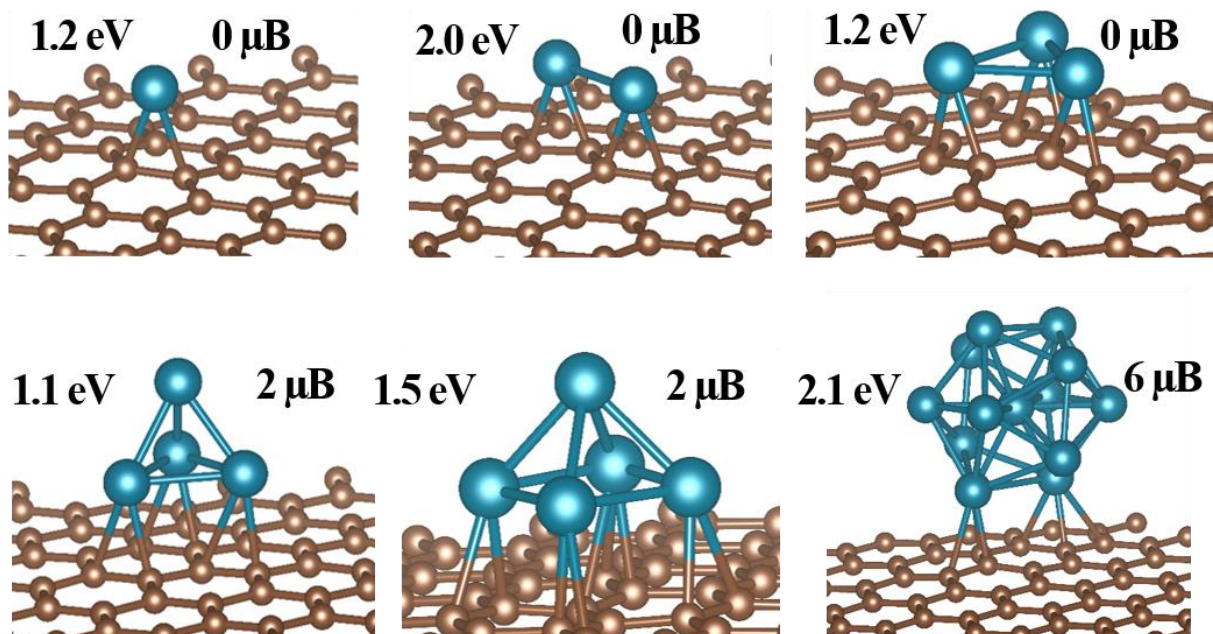


Figure 2-2 Structures, binding energies, and magnetic moments of Pd atom and Pd_n (n = 2, 3, 4, 5, and 13) clusters supported on pristine graphene. The binding energy of the cluster to graphene is calculated as $B_{\text{binding}} = E_{\text{Pd}_n} + E_{\text{(graphene)}} - E_{\text{(Pd+graphene)}}$

We started our study by investigating the binding between pristine graphene and Pd_n (n=1, 2, 3, 4, 5 and 13) clusters as shown in Fig 2.3. For Pd_n cluster (n = 1, 2, 3), the Pd cluster is a 2-D monolayer structure supported by graphene. However, after the number of atoms in the cluster exceeds three, the Pd cluster forms 3-D structure. It is not surprising since the mild binding between Pd cluster and pristine graphene is unlikely to generate uniformly distributed monolayer Pd sheet on the graphene. The most stable structure of Pd atom integrated with pristine graphene is when Pd atom bind to the apex of the sp² carbon-carbon bond. The binding energy of the calculated Pd clusters to graphene is varied based on the size and the geometrical structure of the Pd cluster. However, the maximum binding energy is only 2.1 eV when Pd₁₃ bound to the pristine graphene. It is also important to note that the binding energy of the Pd cluster to the graphene is not increased significantly as the number of anchored Pd increased. For the small Pd_n clusters

where $n= 1-5$, the Pd cluster binding energies to the pristine graphene is close to than the average binding energies of the corresponding free clusters. For the large Pd₁₃ cluster, the binding energy of Pd₁₃ to the pristine graphene is about 0.5 eV lower than the average binding energy of the free Pd₁₃ cluster. It is indicated, for the large cluster of nanoparticles, other than the Ostwald ripening process which described as the transfer of individual atoms from the small nanoparticles to the big nanoparticle, the leaching mechanism of the pristine graphene supported the Pd nanoparticles is preferred the detachment of the entire metal nanoparticle.

The charge analysis on the pristine graphene supported Pd_n clusters shows charges ($0.21e^-$ to $0.35e^-$) flow from Pd_n clusters to the pristine graphene sheet. The charge flow also quenched the magnetic moment in small Pd_n clusters ($n = 1, 2$ and 3) and reduced the magnetic moment of large Pd clusters ($n = 4, 5$ and 13). It is reasonable since the small Pd_n is a monolayer structure and all the Pd atom in the cluster is in contact with the graphene lattice. The charge flow between the metal cluster and the graphene lattice could be an essential factor affect the electronic property and catalytic reactivity of the supported metal.

Then we studied different heteroatom-doped graphene. When a heteroatom is doped into the graphene lattice several, several possible integrated structures could be formed. The quaternary or graphitic substitution is one of the most common integration when the heteroatom is doped on a site that is distant from the edge and vacancy defects of graphene. As shown in fig 2.4, we compared structures and binding energies of O, Si, N, and B doped graphene as well as Pd clusters supported on the doped graphene. Note that boron is a group III element and forms P-type doping for the graphene lattice. In contrast, the group V element, nitrogen, will form n-type doing site. For the N doped graphene, in our calculation, the N-C bond is 1.4192 angstrom and the experimental data is 1.42 angstrom(113).

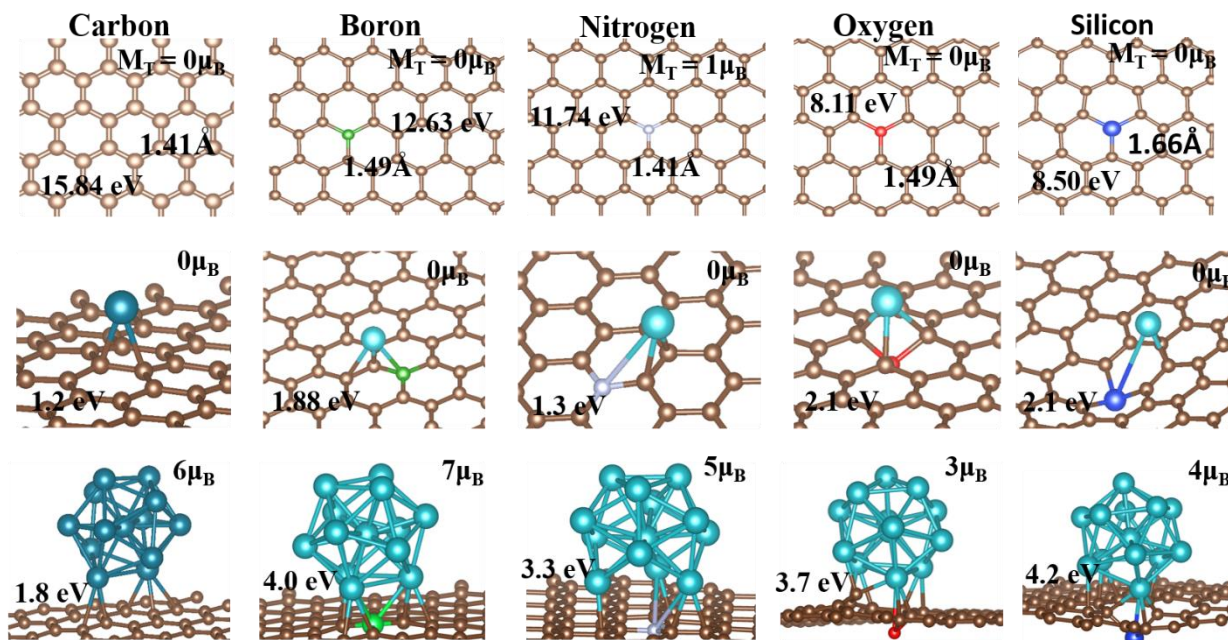


Figure 2-3 The structures and binding energies of Pristine and B, N, O and doped graphene as well as the structure and binding energies of Pd atom and Pd₁₃ cluster supported on Pristine and B, N, O and doped graphene

For different elements doped graphene, the binding energies of the heteroatoms to the graphene varies significantly. The dopants with the atomic radius close to C, such as B and N which are the closest neighbor of C, have the highest binding energy to the graphene lattice. The spin multiplicity for most of the doped graphene is singular except for N-doped graphene whereas the spin multiplicity is two. The charge analysis for the doped graphene also provided important information of the dopants. B and Si donate all the charge to the graphene lattice. In contrast, N and O acquire charges from nearing carbons. One would assume that O gain considerable more charge than N since the electronic negativity of O is lower than N. However, the calculation shows the opposite result: The N doping atom withdraws $2.7 e^-$ charge from graphene comparing $1.2 e^-$ in O doped graphene. This interesting observation results from the fact that N form sp^2 hybridization with the surrounded carbons, in contrast, the sp^3 hybridization formed by O and C

disturbing the charge transfer through the doped graphene. Both of the n-type and p-type doping open the band gap of the graphene.

Then we investigated the interaction between the doped graphene and Pd atom as well as a Pd₁₃ cluster. For the individual Pd atom, all the binding energies of Pd atom to the doped graphene are greater than the binding energy of Pd atom to pristine graphene. However, the binding energy of Pd atom to N-doped graphene is only lifted by 0.1 eV comparing with pristine graphene. It is interesting that, for the N and Si-doped graphene, the Pd atom is more stable whereas Pd bound to the apex of the neighboring carbon rather than Pd directly bound to the dopant atoms: when Pd atom bound to the apex of the C-N bond, the binding energy is only 0.73 eV which is even less than the binding energy of Pd to a pristine graphene. Furthermore, the magnetic moment of the Pd atom decorated doped and pristine graphene is zero. And the charging analysis indicates Pd atom donated 0.25 e⁻, 0.1 e⁻, 0.29 e⁻, and 0.25 e⁻ to the B, N, O and Si-doped graphene, respectively. Both the binding energy and the charge flow results indicate that graphene becomes a better charge donor after the N doping. Unlike the case when single Pd atom bound to the doped graphene where the binding energies increase are not significant compared to the binding with pristine graphene, doped graphene significantly enhance the binding energy of Pd₁₃ cluster to the graphene. The increase of the binding energy is due to the fact increasing the number of Pd anchor sites on pristine graphene has a negligible effect on the overall binding energy of the whole cluster to the graphene. In contrast, raising the number of anchor Pd site on the doped graphene almost linearly boosts the binding energy of the cluster to the graphene. The magnetic moment of the decorated doped Pd₁₃ clusters varies based on the dopants. And the charging analysis indicates Pd₁₃ cluster donated 0.47 e⁻, 0.14 e⁻, 0.59 e⁻, and 0.55 e⁻ to the B, N, O, and Si-doped graphene, respectively.

The charge withdrawn by the N-doped graphene is less than the pristine graphene which is consistent with the previous finding when the Pd atom absorbed on the N-doped graphene.

2.3.3 Interaction between Pd clusters and epoxy and hydroxyl groups on graphene

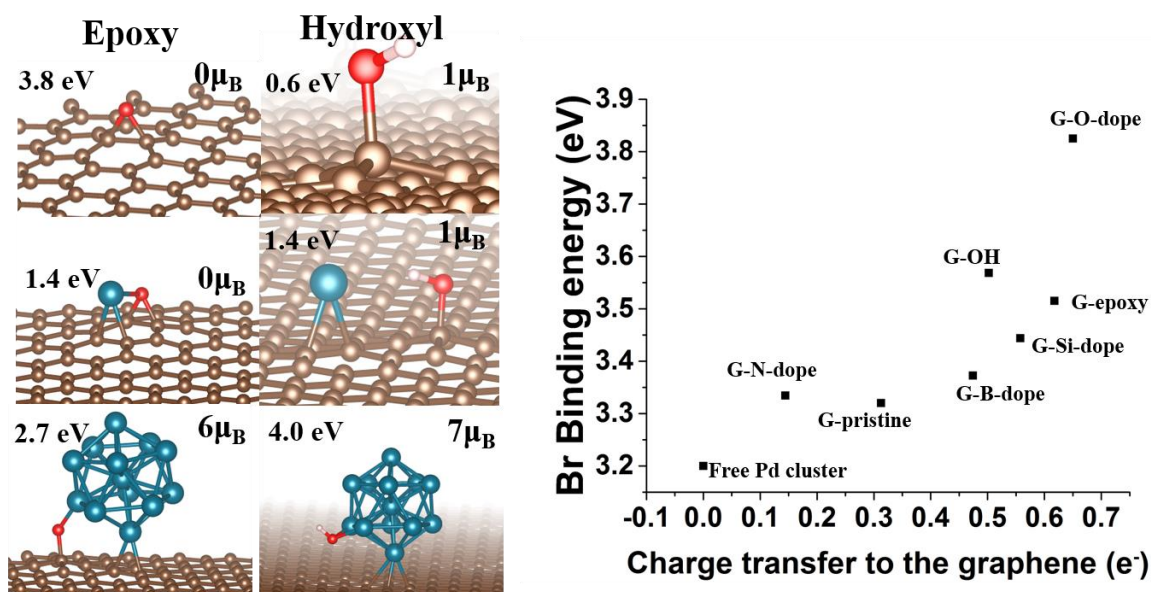


Figure 2-4 Left figure shows the structures and binding energies of epoxy and a hydroxyl group on the graphene as well as the structure and binding energies of Pd atom and Pd₁₃ cluster to the epoxy and hydroxyl group on the graphene. On the right, the figure shows the bromine binding energy to Pd₁₃ cluster supported on different impurity doped graphene as a function of the charge transferred from the Pd₁₃ cluster to the graphene.

Graphene oxide (GO) is another support substrate of great interesting. The dominated function groups on graphene oxide are epoxy and hydroxyl group that forming a single C-O bond. Carbonyl and carboxylic groups, forming C=O bond, mainly exist on the edge of the graphene lattice. The ratio of the C-O functional group reaches to 95% of all the O functionality based on different oxidation methods (114). Recent research also suggested that those C-O functional groups tend to form an aggregated island, instead of evenly distributed on the graphene surface (115). The oxygen content in GO can reach to 60% and about 10-20% in the reduced graphene oxide (rGO) which is

the supporting substrate used in many previously reported Pd/graphene catalysts. Understanding the interaction between the functional groups and Pd atoms and clusters provides the vital information in understanding the stability of the Pd/graphene catalyst as well as the initial nucleation process when the metal precursor and the GO are reduced at the same time.

The left graph of Fig 2.5 shows the structure and binding energy of the epoxy and hydroxyl group bound to the pristine graphene. The binding energy of the epoxy group is significantly higher than the binding energy of the hydroxyl group. The two kinds of oxygen-based function groups possess the similar binding energy to the Pd atom which is 0.2 eV higher than the binding energy of one Pd atom bound to a pristine graphene. This result also suggests that during the initial nucleation process when the Pd nanoparticles started to grow on the graphene, the oxygen-based functional groups would serve as the anchor point to bind the Pd atom and form the nuclei. One observation for the case of hydroxyl group suggest the C-O-Pd bonds are not stable: when the Pd atom approaching from the oxygen side, the -OH group tends to detach from the graphene and form a graphene-Pd-(OH) complex. As a result, the Pd is more stable to bind the neighboring C-C bond of the hydroxyl group. This observation is consistent with the situation when Pd₁₃ cluster bound to the hydroxyl site where the Pd cluster pulled the -OH group from the graphene sheet. The magnetic analyzes suggest that the epoxy decorated graphene has no magnetic moment. In contrast, the spin multiplicity of the hydroxyl group decorated graphene is two. The oxygen content of the graphene oxide can be reduced by a variety of reduction methods, such as chemical reduction by a strong reducing agent, photo-catalysis reduction, electrochemical reduction and thermal reduction. And the C=O functional groups are more difficult to be reduced reported by several recently published works. One report using microwave irradiation as reduction treatment for graphene oxide suggested that microwave is an extremely efficient method to remove the

oxygen functional group. It is also suggested that the formation of certain vacancy defected site on graphene is associated with the reduction of hydroxyl and epoxy group (116).

To understand the change of the electron donating capability of the Pd cluster after supported on different graphene lattice, we tested the bromine binding energy of the supported Pd cluster as an indication. The bromine group is a charge acceptor and commonly used in the cross-coupling reaction as in the leaving group in the aryl-halide reagent. As shown in fig 2.5 B, after deposit the Pd₁₃ clusters on different pristine and doped graphene sheets, the binding energies of a bromine atom to the metal cluster are increased. It is particularly interesting that increases in the bromine binding energies after deposition are also corresponding to the amount of charge withdrawn by the graphene lattice from the Pd cluster. It is generally assumed that charge donation capability is diminished after a neutral cluster becomes positively charged. However, the bromine binding energy analysis shows the exact opposite trend: Pd clusters donated the largest amount of charge to the oxygen doped graphene and became the most positively charged supported cluster. In the meantime, the binding energy of bromine to this supported cluster is more than 3.8 eV which is 0.6 eV higher than the Br binding energy of free Pd₁₃ cluster. This opposite trend indicates the graphene supports to enhance the charge donation capability of the supported metal cluster and more strong interaction between the supported metal and the graphene lattice results in a more significant enhancement in bromine binding energy.

2.3.4 Pd cluster binding to vacancy defects on graphene

Graphene, obtained by the reduction of graphene oxide, contains defects of various types and sizes. Several papers published recently also suggested that vacancy defects can be generated through microwave irradiation of the metal-graphene complex (117). These defect sites have the potential to strongly bind palladium clusters. Consequently, we first undertook a study of the

properties of various defects including defects obtained by removing a varying number of C atoms as well as Stone-Wales defects that do not involve the removal of atoms. For each defect, the sites surrounding the defect locations were optimized by calculating the force on atoms and moving atoms in the direction of forces till the forces dropped below a threshold value of 0.01 eV/Å. The defects are labeled by the size of the polygons surrounding the defected region. Figure 2.6 shows the spin magnetic moment and the nature of the polygons around the defected site and in Table 2.3, we list the nature and size of the defect and the associated spin multiplicity. And the defect energy (E_d) calculated as

$$E_d = (E_{\text{defect graphene}} + nE_{\text{carbon}}) - E_{\text{pristine graphene}}$$

Where $E_{\text{defect graphene}}$ is the total energy of defected graphene, n is the number of removed carbon and $E_{\text{pristine graphene}}$ is the energy of pristine graphene.

The defect energies are increased as the number of missed carbon increased. However, the average energies of removing one carbon are decreased which indicates the defects is less stable as the size of the vacancy grows. The double vacancy defect site is a particularly interesting structure. The double vacancy can be formed either by coalescence of two single vacancy defect or remove two neighboring carbon atoms. A previous study suggested that the double vacancy is more thermally stable than the single vacancy defect and is also frequently observed by electron microscopic experiments (100). Note that while the smaller defects have singlet ground states, multiplicities of 7 and higher emerge as the size of the defect increases beyond 6.7Å. These findings agree with previous studies as shown in Fig 2.3 B, C, and D.

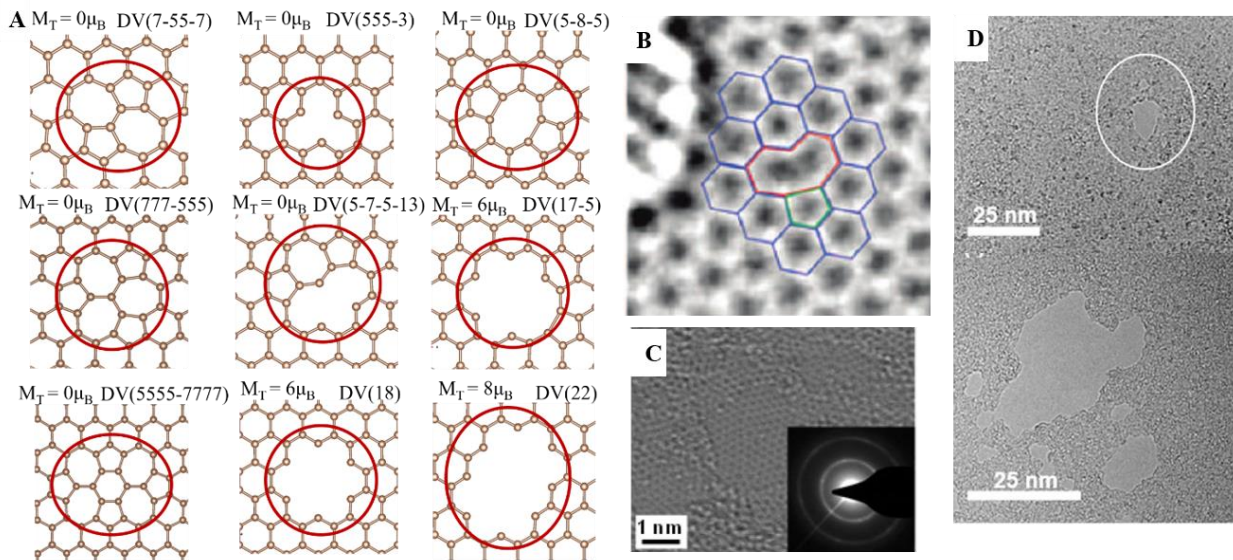


Figure 2-5 (A) DFT calculations on the magnetic moment and the nature of the polygons around the defected site. (B) HR-TEM image shows double vacancy defect site on graphene (*100*). (C) HR-TEM images show Stone-Wales defect (*115*). (D) TEM images show large voids sizing 1-40 nm in the lattice of graphene (*101*).

Defected graphene	Size of Vacancy (Num. of C)	Size of Vacancy (Å)	Defect energy (eV)	Spin multiplicity
DV(7-55-7)	0	3.2	5.11	1
DV(555-3)	1	4.4	17.12	1
DV(7777-5555)	2	3.2	25.82	1
DV(777-555)	2	3.2	26.17	1
DV(5-8-5)	2	5.0	26.36	1
DV(5-7-5-13)	3	5.5	40.97	1
DV(18)	6	6.7	72.97	7
DV(17-5)	7	7.0	83.67	7
DV(22)	10	8.6	115.97	9
DV(24)	13	9.0	148.56	11

Table 2.2 the nature and size of the defect and the associated spin multiplicity.

Depending on the size of the void, we next investigated the binding energy of the Pd atom and Pd_n clusters to the defected site. Fig. 2.4 shows the atomic structure of the ground state and in the

table in Appendix A lists the binding energy of the Pd site to the defect. The Pd binding energy (E_{binding}) is calculated as

$$E_{\text{binding}} = E_{\text{Pd}} + E_{\text{(defect graphene)}} - E_{\text{(Pd+graphene)}}$$

For all the defects, the spin of the ground state is a singlet. This is particularly interesting for DV(18) as the isolated vacancy had a spin multiplicity of 7 and the addition of Pd quenches the spin moment even though the Pd atom is linked to only two carbon sites. The Pd binding energy also shows large variations in the nature of the defect. One can broadly classify the binding sites into two categories: (1) defect sites where the graphene sheet heals to fill the void and forming three, five, or seven-member rings and (2) the cases where the relaxed structure has a larger central hole that can accommodate an individual Pd atom or multiple sites associated with a cluster. For the former which has a defect size no larger than 3.5 Å, the Pd binding energy ranges from 1.72 to 2.13 eV compared to 1.26 eV for the pristine graphene. This shows that even the Stone-Wales defects bind Pd more strongly than the pristine graphene. The binding energy is however considerably enhanced to 7.28 eV as the defect size increased to 6.7 Å as in DV(18). This is clearly seen in Fig. 2.5 A that shows the binding energy of the atom on different defect sizes.

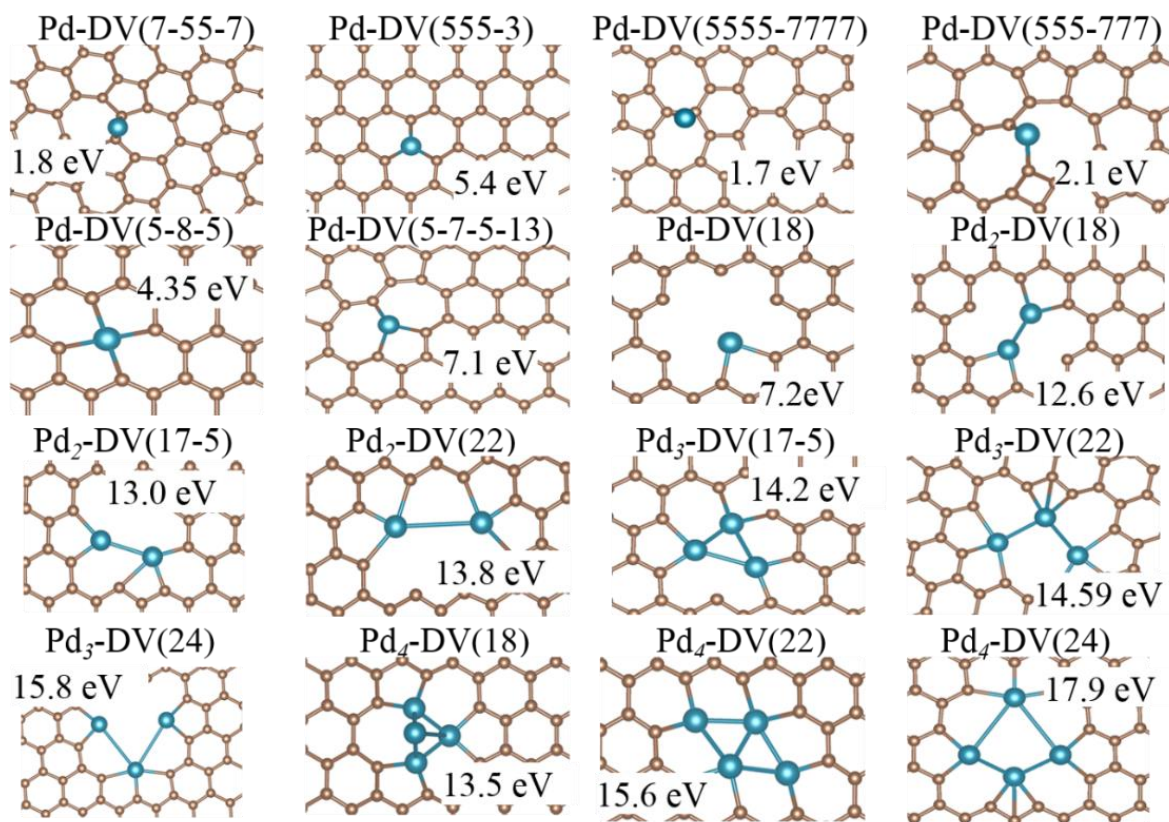


Figure 2-6 Pd₁₋₅ bound to various size and structure of vacancy defected graphene.

As the large defect site is capable of accommodating more Pd atoms, we also calculated the binding energy of multiple anchored Pd_n clusters to the defect. By binding palladium clusters to a larger void, the binding energy increased to 13.8 eV, 15.8 eV and 17.9 eV for 2, 3, 4 anchored Pd_n clusters respectively. As shown in Fig 2a, there is almost a linear correlation between the number of anchored Pd sites and binding energy, and a further correlation to the size of the void. These trends indicate that the size of the void is important for strongly binding the Pd_n clusters since large voids allow the formation of multiple Pd-C bonds that increase the binding.

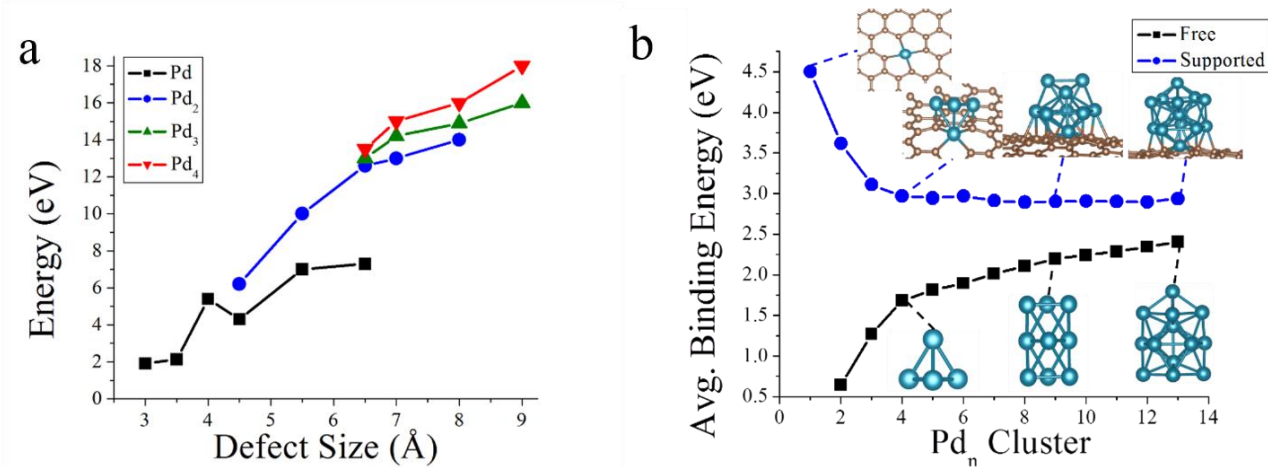
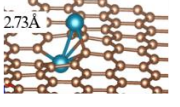
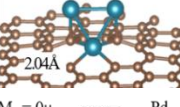
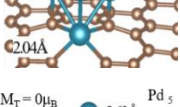
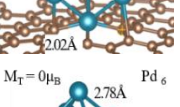
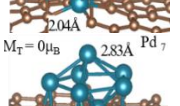
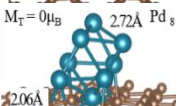
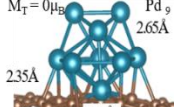
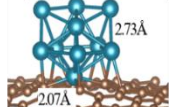
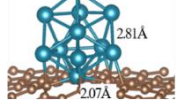


Figure 2-7 Stability cluster of Pd_n bond covalently to defected graphene. (A) The binding energy of Pd_n, n=1-4 on differently sized graphene defects. (B) The average atomization energy of free Pd_n clusters and Pd_n on defected graphene.

Then we investigated the growth of the Pd cluster on a double vacancy defected site, as shown in tab 2.5. Other possible structure of the supported Pd_n cluster also calculated as shown in the appendix. The ground state geometries are generally compact and in special cases, there are significant changes in the shape of the cluster. For example, for Pd₁₃, the ground state of the free cluster is a bi-layer structure while the ground state of the deposited species is a slightly distorted icosahedral structure. The change in structure can be related to the charging of the cluster and the effect of the support that can affect the ground state. Starting from Pd₄, the binding energy to the defect generally increases with cluster size and a Pd₁₃ is bound by almost 7.4 eV compared to 5.4 eV for Pd₄. The increase in binding is accompanied by the larger charge donated to the surface and almost half the charge donated to the surface is derived from the Pd sites anchoring the cluster to the surface. The Avg. Pd Binding energy (eV) was calculated as:

$$\text{Avg } E = (E_{(\text{Pd}_n/\text{graphene})} - nE_{(\text{Pd})} - E_{(\text{graphene})})/n$$

Where $E_{(Pd_n/graphene)}$ is the total energy of the cluster and graphene, $E_{(graphene)}$ is the energy of graphene and $E_{(Pd)}$ is the atomic energy.

Pd cluster	Avg. Pd Binding energy (eV)	Binding energy to defected graphene(eV)	Spin multiplicity	Charge on Pd cluster	Charge on anchor Pd
$M_T = 0\mu_B$ Pd ₂ 	3.62	6.24	1	0.80	0.48
$M_T = 0\mu_B$ Pd ₃ 	3.11	5.52	1	0.78	0.58
$M_T = 0\mu_B$ Pd ₄ 	2.97	5.39	1	0.76	0.57
$M_T = 0\mu_B$ Pd ₅ 	2.94	5.82	1	0.90	0.59
$M_T = 0\mu_B$ Pd ₆ 	2.97	6.04	1	0.92	0.60
$M_T = 0\mu_B$ Pd ₇ 	2.91	6.43	1	1.09	0.59
$M_T = 0\mu_B$ Pd ₈ 	2.89	6.38	1	1.02	0.60
$M_T = 0\mu_B$ Pd ₉ 	2.90	6.35	1	1.09	0.58
$M_T = 2\mu_B$ Pd ₁₀ 	2.91	7.11	3	1.10	0.58
$M_T = 2\mu_B$ Pd ₁₁ 	2.90	7.34	3	1.13	0.58

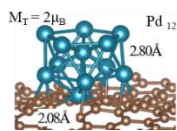
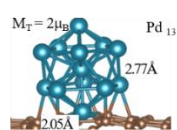
	2.90	7.04	3	1.14	0.59
	2.94	7.42	3	1.10	0.57

Table 2.3 Binding energy, spin multiplicity and charge state of Pd₂₋₁₃ cluster are listed. Average binding energy is in the form of binding energy per Pd atom. The binding energy to the defect is the binding energy between the cluster defected graphene.

It is interesting that after depositing the Pd clusters on the graphene, the magic number of the clusters which indicates a more stable structure also are changed as shown in Fig 2.7. The more stable supported Pd clusters, Pd₆ and Pd₁₃, are both closed shell structure. Besides the incremental energies, the binding within the cluster is also enhanced upon deposition. This is shown in Fig. 2.5 B where we compare the average binding energy of free and supported clusters. The stronger binding results in reduced leaching of the catalyst, and higher recyclability. Furthermore, the trend of average binding energy for the free and supported clusters are expected to converge at a larger cluster size. This indicates that the binding enhancement of individual Pd atom in the cluster after deposition is only achievable once it reaches a certain cluster size. Other than the binding energy and geometric structure change, the electronic structure also shifted significantly after deposit the metal cluster on the graphene lattice. Individual Pd atom charge states in double vacancy defected graphene supported Pd_n clusters (n=1-14) are shown in the appendix. Anchor Pd is marked by large electrons transfer to graphene substrate. Bottom layer Pd atoms show a slightly positive charge in some structure. Upper layer Pd, on the other hand, is neutral.

In summary, the Pd atom and clusters on defected graphene bind strongly to the vacancy defects and voids that are generated either by reduction of the graphene oxide or removal of carbon atoms in lattice via thermal or laser irritation. And large voids can provide strong binding to large clusters

or nanoparticle which reduce the possibility of the cluster detaching from the graphene lattice to the solution phase during the reaction. However, since the vacancies and voids in the graphene lattice are mobile, the case that Pd clusters jump from one defect site to another is not fully studied. The average individual Pd atom binding energies within the cluster after deposition also increased comparing with free clusters which tend to minimize the possibility of leaching a single atom. However, the leaching of Pd in a specific reaction may affect the selection of reagent, solvent, additive and reaction temperature.

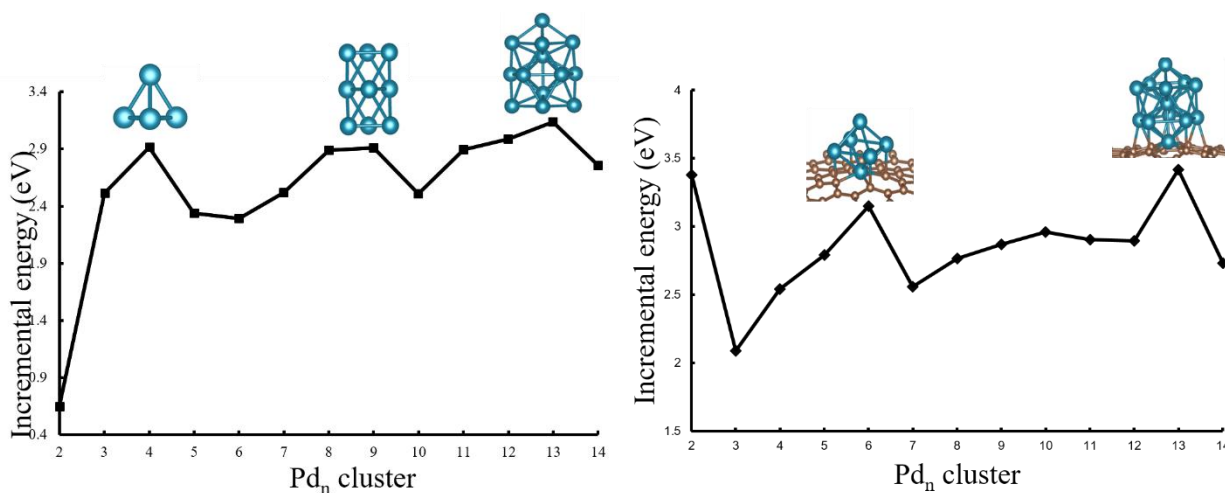


Figure 2-8 Incremental energies of free and supported Pd_n n=1-14 clusters.

2.4 Conclusion

After comparing different strategies, binding via oxygen functional groups, surface doping, and vacancy/void defects, to immobilize the Pd clusters, the defect site on graphene provide the strongest binding of the metal cluster to the graphene lattice. This is also consistent with previous experiments examining Pd/G catalyst, reduced via microwave irradiation and laser irritation to generate the defect site on graphene, for a variety of Suzuki, Heck, and Sonogashira reactions that showed that the catalyst can be recycled more than six times with high activity. It should also be noted that the microwave irradiation (MWI) method used for the preparation of these catalysts is

similar in nature to the recently reported method used to produce well-defined defect sites on graphene surfaces. In contrast, some Pd/G catalysts reduced by hydrogen in a mild condition, which generated fewer vacancies or voids, still have significant leaching issue (60).

Chapter III DFT study of the full reaction cycle of Suzuki reaction catalyzed by palladium on graphene catalyst

3.1 Introduction

The Suzuki reaction follows a three-step pathway of oxidative addition, transmetalation, and reductive elimination (118). For using DFT to study homogeneous catalysis, several publications include detailed studies for the full reaction cycle have been published in the past decades (118-121). Computational studies focused on ligand effects on oxidative addition and reductive elimination step of Suzuki reaction were also carried out (122-125). The enantioselectivity of Suzuki reaction was also studied using DFT to elucidate the chirality of the transfer (126). The effects of the base were studied to illustrate the thermodynamic preference in the different proposed pathways in the transmetalation step (127). An illustrative research project tried to compare the cross-coupling reaction catalyzed by Pd^{II}/Pd^{IV} redox system with traditional Pd⁰/Pd^{II} (128). The complex interaction between Pd precursors and ligands to produce the Pd⁰ was reported in 2017 (129). However, the reported research on the reaction mechanism of Pd catalyzed Suzuki reaction only focused on the homogeneous process. The understanding of the mechanism of Pd clusters of nanoparticles catalyzing the reaction is astoundingly limited.

In our theoretical calculation, we used 4-bromobenzoic acid and phenylboronic acid as the reagents as shown in Fig 3.1. In the oxidative addition step, the Br-C bond of 4-bromobenzoic acid is cleaved by a Pd cluster/atom which requires a charge donation from the catalyst and support (Fig. 3.1 blue arrows). The second step, transmetalation, begins with the bromine-palladium complex being substituted by a hydroxyl group forming the aryl-Pd_n-OH intermediate. The aryl-Pd_n-OH intermediate then reacts with the phenylboronic acid and the carbon-boron bond is cleaved

to form a biaryl-Pd_n-B(OH)₃ complex. During the transmetallation step charge flows towards the phenylboronic acid when breaking the carbon-boron bond, and then flows back when forming the palladium-boron bond. The other possible route for transmetallation involves forming an aryl-B(OH)₃⁺ complex in the presence of base firstly, is also investigated. However, this route is energetically unfavorable due to the unstable aryl-B(OH)₃⁺ intermediate which is consistent with recent findings. In the reductive elimination step, the carbon-carbon bond is formed and the product is released from the palladium surface. This process involves charge flowing back from the biaryl complex to the catalyst (Fig. 3.1 red arrow). Thus, different steps of the catalytic cycle for the Suzuki cross-coupling reaction requires the catalyst to serve alternately as both an efficient charge donor and acceptor.

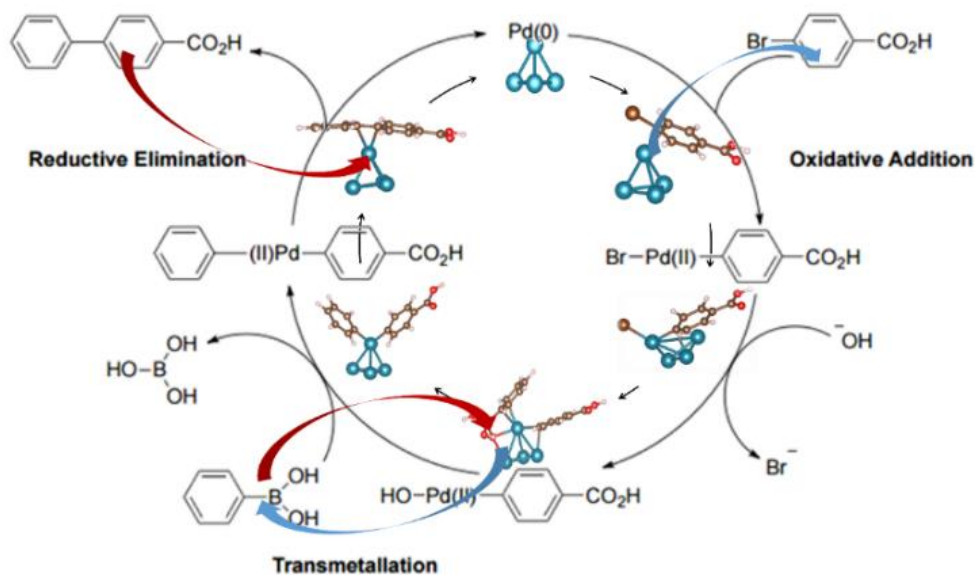


Figure 3-1 Reaction mechanism of Suzuki reaction catalyzed by Pd₄ cluster.

3.2 Method

The theoretical studies used a gradient corrected functional proposed by Perdew et al.^{Cite} The VASP code was used, and the Kohn–Sham orbitals were expanded using a plane wave basis set

and the cutoff was set to 400 eV. The projector-augmented wave method was used to treat electron-ion interactions. Van der Waals correction (DFT-D2) was applied. A dipole correction was incorporated along the z-axis of the slab, and the Gamma point is used for Brillouin zone integration. Since small Pd_n clusters carry magnetic moments, various spin states were investigated to determine the ground state. Bader charges were used to determine the charge of the individual atoms. Nudge elastic band method was applied to optimize the reaction pathway.

3.3 Result and discussion

3.3.1 Activation energy of full reaction cycle of Suzuki reaction

Firstly, the individual steps and overall reaction activation energies for free Pd_n clusters (n=1, 4, 13, and 14) were examined to understand properties that enhance activity in homogeneous catalysts. The Pd atom^(130, 131) and Pd₄ clusters were selected based on earlier studies⁽¹³²⁾ which found that the presence of Pd₁ or Pd₄ fragments in solution were critical for cross-coupling reactions. Pd₁₃ and Pd₁₄ clusters were selected as Pd₁₃ is the first cluster with a complete geometric shell,⁽¹³³⁾ while Pd₁₄ has one additional atom past a filled geometric shell which mimics a protruding low coordination site for enhanced activity ⁽¹³⁰⁾.

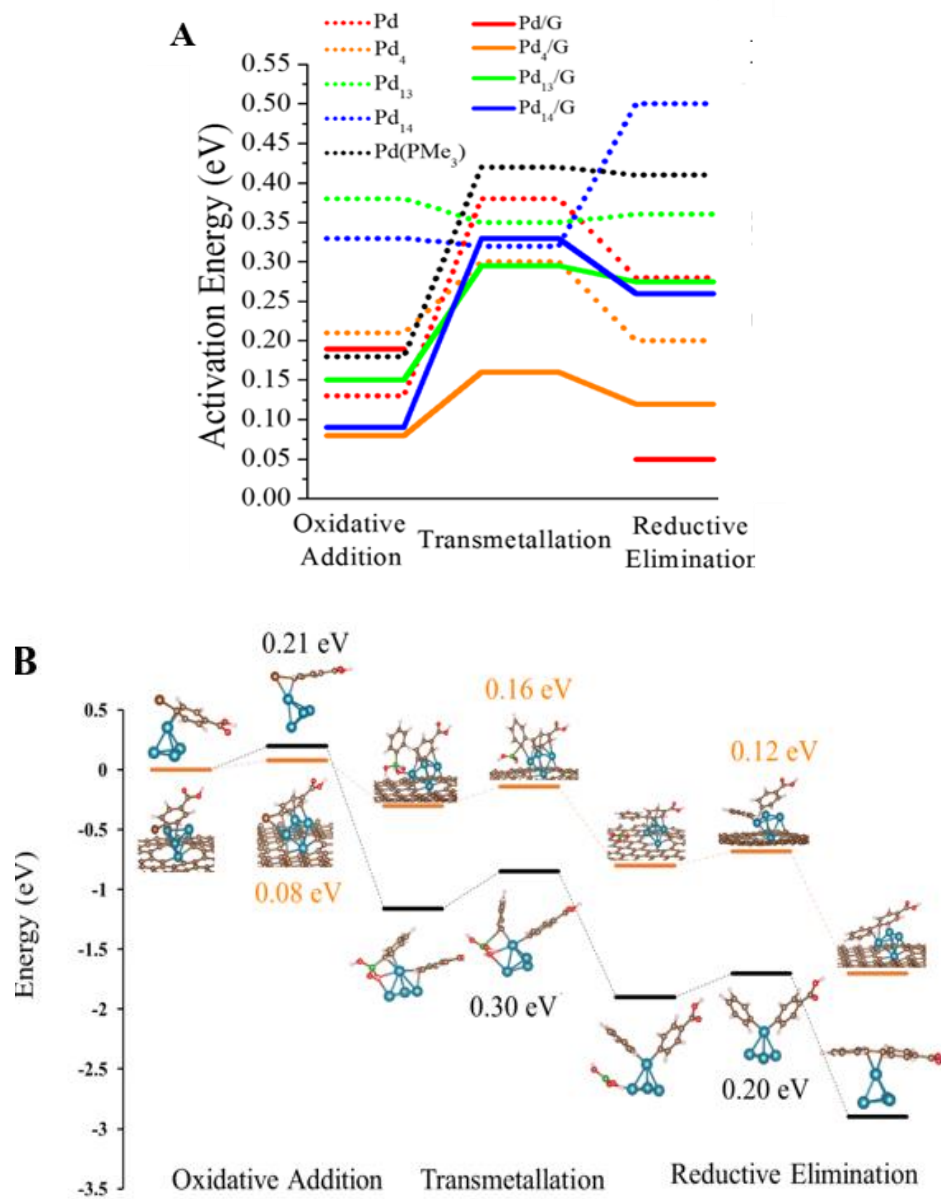


Figure 3-2 (A) Activation energy of free and supported Pd_n clusters (n=1, 4, 13, and 14, and Pd(PMe₃)) in the three Suzuki reaction steps. (B) Full reaction pathways for Pd₄ and Pd₄/G.

Pd Cluster	Oxidative addition (eV)	Transmetallation (eV)	Reductive elimination(eV)
	Charge donor	Charge donor&acceptor	Charge acceptor
Pd ₁	0.13	0.38	0.28
Pd ₄	0.21	0.3	0.20
Pd ₁₃	0.38	0.35	0.36
Pd ₁₄	0.33(break)	0.32	0.5(break)

Supported Pd1	0.19	-	0.05
Supported Pd4	0.08	0.16	0.12
Supported Pd13	0.15	0.3	0.28
Supported Pd14	0.09	0.33	0.26
Pd/P(Me) ₃	0.18	0.42	0.41

Table 3.1 Activation energies in full reaction cycle for free and supported Pd_n cluster (n=1, 4, 13, and 14) and ligated Pd.

The activation energy of Pd_n clusters bound to double atom vacancy sites in the graphene sheet was calculated to understand the effect of the strong Pd-support interaction on the electronic property of the metal clusters. For comparison, we have also calculated activation energies for a Pd atom ligated by P(Me)₃ as a model of a ligated homogeneous catalyst. For Pd₄, Pd₁₃, and Pd₁₄, the activation energies for clusters supported on reduced graphene are all lower than those for the corresponding free clusters, which indicates that the strong Pd-support interaction enhances Pd_n cluster reactivity in each step. The full Suzuki reaction pathway for Pd₄ and Pd₄/G is shown in Fig. 3.2 B. For the single Pd atom that bound to a vacancy, steric effects prevented the transmetallation step from proceeding (131). In a free Pd₁₄ cluster, the adatom that protrudes from the cluster is removed from the cluster during the oxidative addition and reductive elimination steps indicating that the reaction etches the cluster. However, the supported Pd₁₄ adatom is not etched showing that the strong support interaction reduces Pd leaching with the support also enhancing the intra-cluster binding (134). These results strongly suggest that supported Pd clusters are more effective catalysts because of lower activation energies resulting from the electronic interaction with the graphene support.

3.3.2 Structure effects on the activation energy

After a closer scrutiny on the activation energy of the oxidative addition and reductive elimination step, it was revealed that the size and structure of the Pd cluster drastically affect the

activation energies in those two steps as shown in Fig 3.3 A and B, although the support and ligands also play a significant role. Pd_n clusters with smaller size have low activation energy in the reductive elimination step. However, a glance at the correlation between the size of cluster and activation energies could be misleading. The small clusters usually have the lower coordination of Pd active site which is the determining factor affecting the carbon-carbon bond formation in this step. Pd clusters with a low coordination Pd active site have a lower activation energy than Pd with a higher coordination. This is believed to result from the adjacent Pd trapping the reagents which obstructs the formation of the transition state intermediate. The lower and higher coordination of Pd is described in Fig 3.3 C and D. The Pd atom in a Pd dimer cluster, trimer, and tetrahedron Pd₄ cluster, as well as the protrude site on Pd₁₄ cluster has less than four neighboring Pd atoms are considered as low coordination site. In contrast, a high Pd coordinated site means this Pd has more than four adjacent Pd atoms which are commonly observed in large clusters and ordered crystallinities.

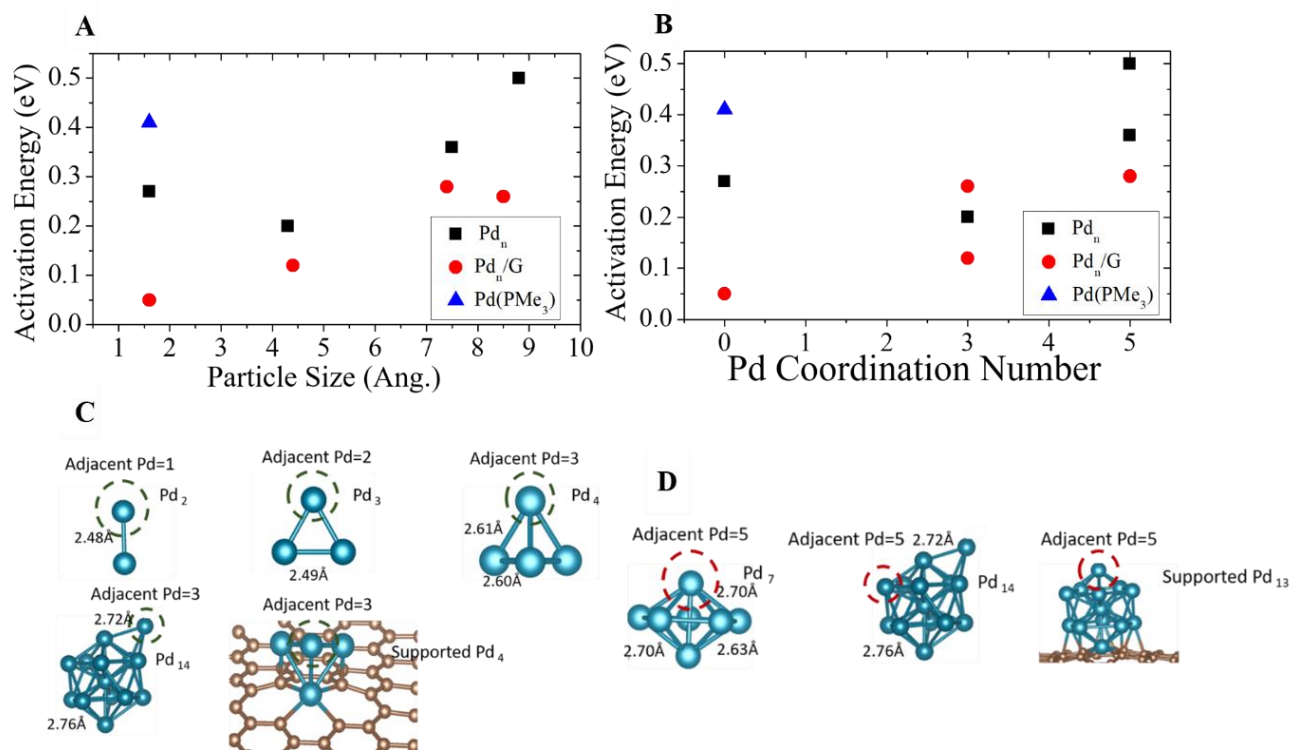


Figure 3-3 Pd_n cluster size (A) and coordination (B) effect on activation energy in reductive elimination step. Pd cluster with lower coordination number and the smaller size is relatively more active in this step. (C) Lower coordination of Pd_n clusters (adjacent Pd less than 4) is more active in oxidative addition and reductive elimination step. (D) Higher coordination of Pd_n clusters (adjacent Pd more than 3) is less active in oxidative addition and reductive elimination step.

To further elucidate the structure effects on the activation energies in the full reaction cycle, we then studied the detailed structure transformation of the Pd-bromobenzoic acid complex during the pathway to fragmentation in oxidative addition step. Electronic structure analysis reveals that the lowest unoccupied molecular orbital (LUMO) of 4-Bromo-benzoic acid is dominated by the aromatic ring. Consequently, the acid initially binds by bonding the two carbon atoms from the phenyl group to the apex Pd site as shown in Fig. 3.4. The bond cleavage starts with a rotation of the adsorbed molecule to form the Br-Pd bond. In this rotation process, the Br and Pd distance decrease quickly. In contrast, the Br-C bond length hardly changed. The rotation is more

energetically unfavorable if multiple Pd-C formed between the adjacent Pd atoms and other carbon atoms in the aryl molecular. As a result, for the Pd₄ cluster with low coordination, the adjacent Pd atoms of the cluster offers no hindrance to the rotation allowing a smooth formation of the Br-Pd bond. In contrast, the two adjacent Pd atoms at the triangular surfaces of Pd₁₃ cluster strongly trapping the benzoic acid molecular obstructs the rotation process and increases the reaction barrier. For the free Pd₁₄ cluster, although there is a protrude site with low coordination,

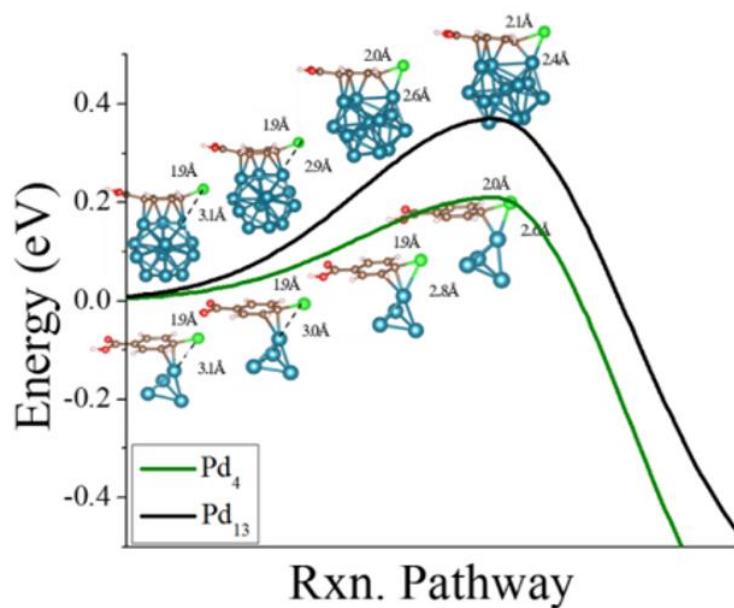


Figure 3-4 The microscopic mechanism of breaking the Br-C bond from the initial state to transition state on the Pd₄ and Pd₁₃ clusters.

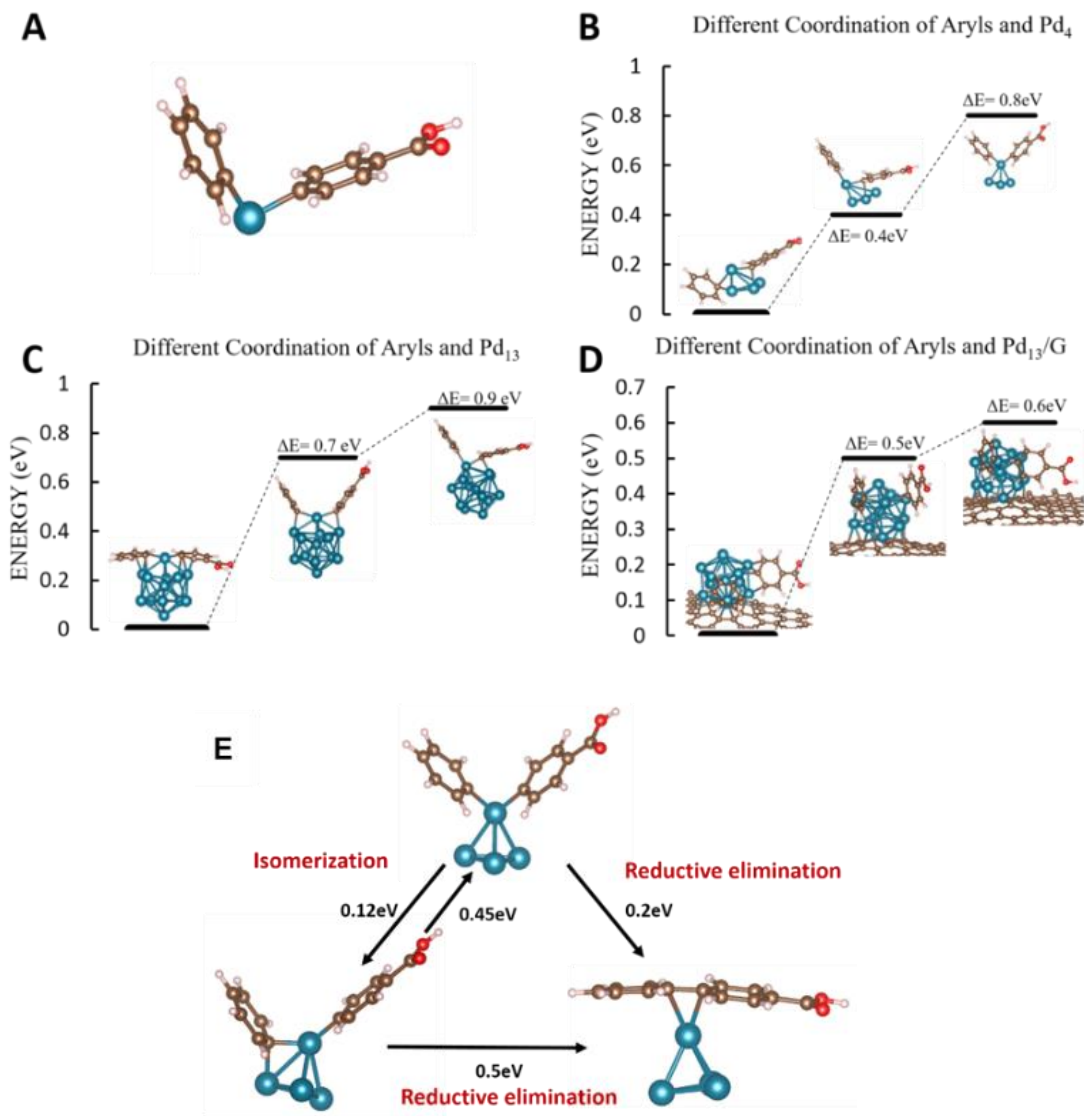


Figure 3-5 Different coordination of Pd_n cluster with biaryl complexes of Pd₁ (A), Pd₄ (B), Pd₁₃ (C), and supported Pd₁₃ (D). Fig (E) shows the activation energies for different biaryl-Pd₄ conformer. And isomerization energy requires transform to another conformer.

In the reductive elimination step, different from the case of single Pd atom as shown in fig 3.5 A, Pd_n clusters form the more stable multi carbon-palladium bonds structure as shown in fig 3.5 B, C, and D for Pd₄, Pd₁₃, and supported Pd₁₃ respectively. Bonds formed between the adjacent Pd_n cluster and the two aryl molecular increases the binding between the catalyst and reagent and

also further separate the two aryls molecular and increase the initial C-C distance. As shown in Fig. 3.5 E, the variation of different activation energies of different Pd₄-biphenyl conformers suggests that it is more difficult to form the C-C bond when the biaryl-Pd_n complex form more stable structure.

Fig. 3.6 shows how the initial biaryl-Pd binding energies and the carbon-carbon distance, in two aryls molecular, in initial state affect the activation energies in reductive elimination step. These results indicate strong binding of biaryl-Pd_n complexes and long initial C-C distance reduce the mobility of aryl reagent on the surface of Pd cluster and eventually obstruct the formation of the new C-C bond. For high coordination Pd site as in Pd₁₃, since the increase in the initial binding energies and carbon-carbon distance is more significant due to more adjacent Pd atoms, the activation energy increase is also more dramatic. However, the case of ligated Pd/PMe₃ is different. The binding energy and carbon-carbon distance are apparently lower than the Pd_n clusters. The activation energy is significantly higher than the supported Pd cluster which suggests the charge state of Pd also play a key role in the formation of the new bond since the ligated Pd is positively charged. In contrast, the supported Pd cluster is negatively charged and the free Pd is almost neutral. Furthermore, no decisive connection between the structure of the Pd active site and the activation energy in transmetallation step is observed.

The graphene also helps to stabilize low coordination Pd sites that are ideal active sites, resulting in an additional reason that clusters supported on defected graphene may enhance the activity. Immobilizing the free cluster on defected graphene assists in maintaining those active sites because of a higher average Pd atom binding energy and the fact that the support leaves less freedom for the deformation of the cluster.

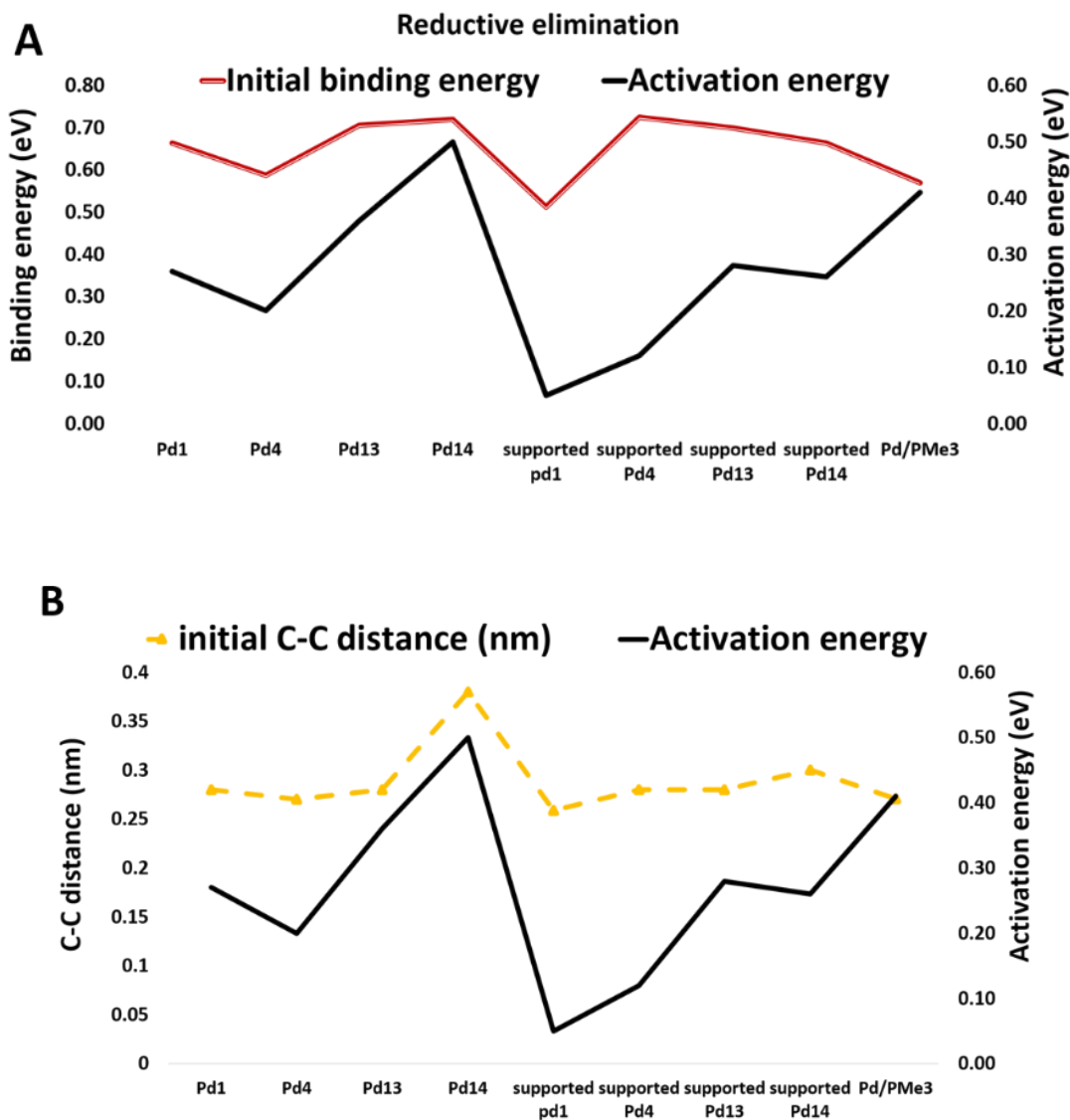


Figure 3-6 (A) Correlation between initial biaryl-Pd_n binding energy and the activation energy. (B) Correlation between the initial C-C distance of biaryl and activation energy.

3.3.3 Charge effects on the activation energy

Structural effects can only explain part of the variations in the activation energies. When directly comparing the corresponding free and supported clusters, the significant decreases of activation energies in both the electron donating and withdrawing steps after deposition are difficult to be explained by the slight structure deformation after immobilizing the metal cluster

on the graphene. As a result, charges on reagents and products were analyzed at each step for each cluster (Fig. 3.7) to identify the physical origin of the reduced activation energies. We first consider the transmetallation step which involves both charge donation and back donation. The Pd catalyst first donated the aryl-B(OH)₃⁺ complex to activate the C-B bond. Then charge flow back to Pd to form the Pd and sp² C bond. As seen in Fig. 3.7 and Tab. 3.2, the electron-rich ligand of the Pd/P(Me)₃ catalyst enhances the charge donation of the catalyst, which is shown as the largest amount of charge transferred to the aryl-B(OH)₃⁺ complete initial state, but the backflow of the charge is hindered which leads to a high activation energy. In contrast, graphene supported Pd clusters, especially Pd₄/G which has donated the lowest amount of charge to the product, have lower activation energies for transmetallation due to the conductive nature of graphene allowing it to accept a charge. There is a clear inverse relationship between the net charge flow and the activation energies demonstrating that catalysts which effectively accept charge are more active for transmetallation as shown in Fig 3.8 A.

Figure number?

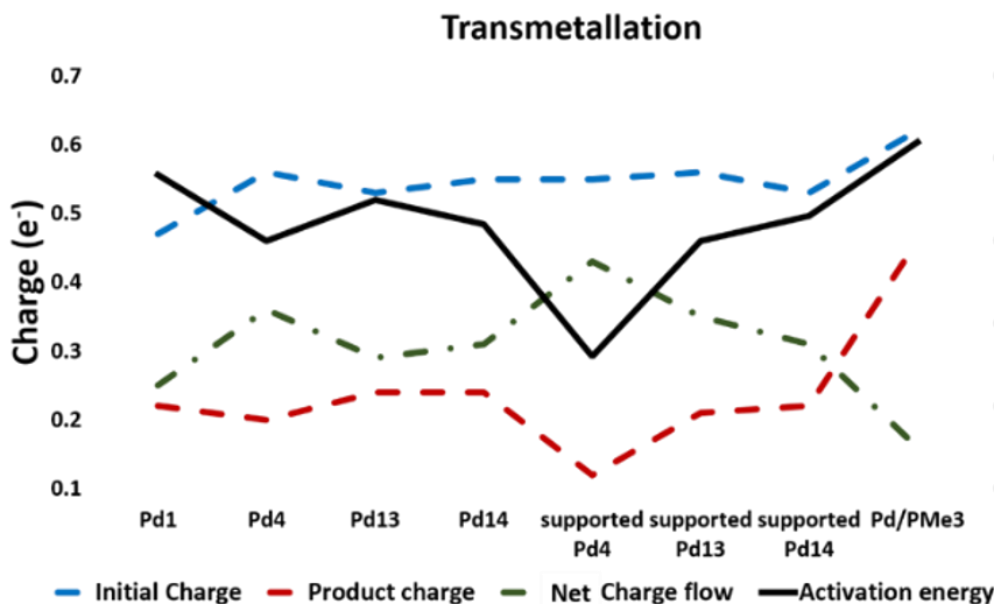


Figure 3-7 Charge transfer and activation energy for free and supported Pd_n , and $\text{Pd}(\text{PMe}_3)$ during transmetallation step.

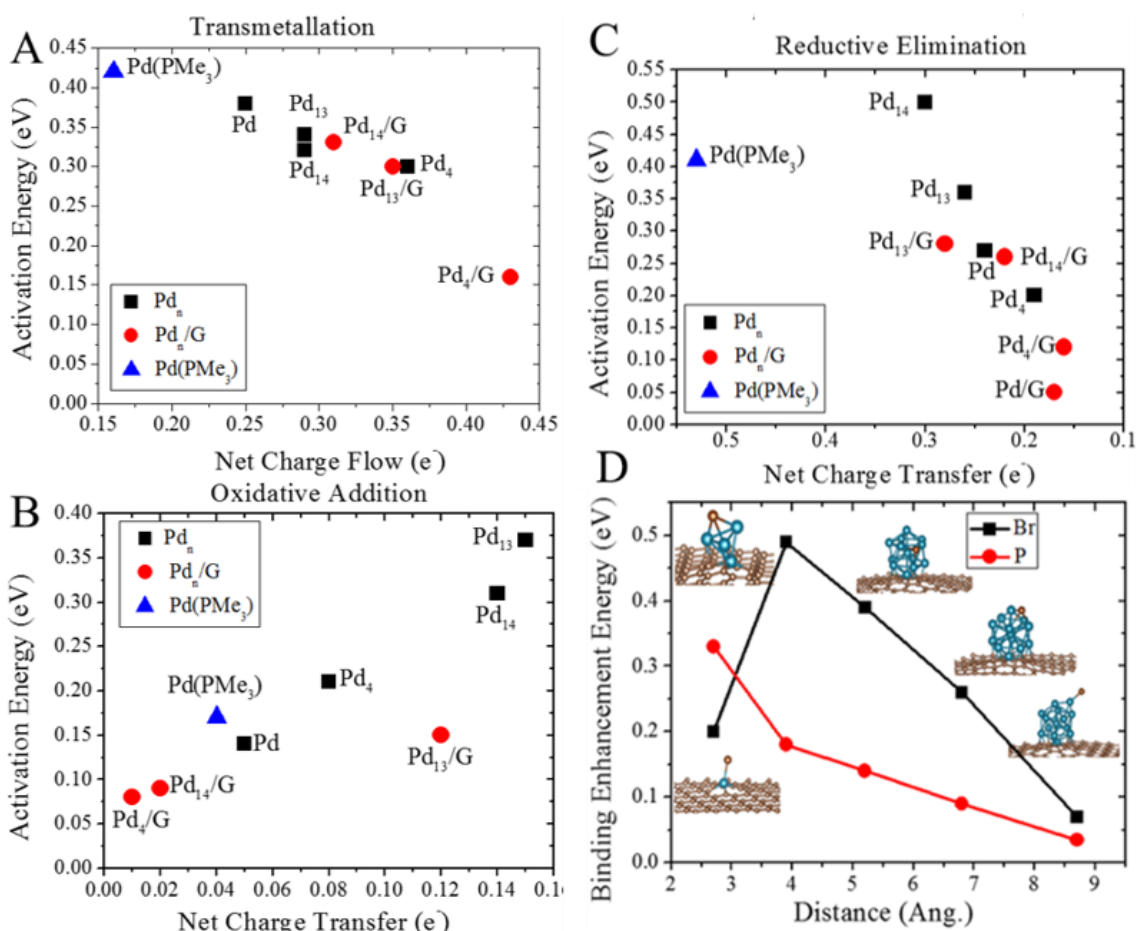


Figure 3-8 Charge transfer and activation energy for free and supported Pd_n , and $\text{Pd}(\text{PMe}_3)$ during (A) transmetallation, (B) oxidative addition and (C) reductive elimination. (D) Enhance Br and P binding energy correlated to the distance from the Pd active site to the lattice of graphene.

The relationship between charge flow and activation energy can also be observed in the oxidative addition and reductive elimination steps (Fig. 3.7 B and C). In oxidative addition, charge donation by graphene to Br lowers the activation energy. In Fig. 3.7 B, clusters that accept a charge from the reactant such as Pd_{13} , and Pd_{14} have high activation energies, while clusters that are better donors, such as Pd_4/G and Pd_{14}/G have lower activation energies. During the reductive elimination

step, the lowest activation energy is observed for catalysts that readily accept a charge. This is supported by the large activation energy for Pd/PMe₃ because the electron-rich ligand causes the catalyst to act as a charge donor, while the better acceptors such as Pd/G and Pd₄/G have lower activation energies. To confirm graphene assists both charge donation and withdrawal, the adsorption energies of Br (acceptor) and P (donor) were calculated as shown in Fig 3.7 D. The binding energy of both the Br and P are enhanced on the defected graphene as compared to the free clusters, confirming that the support enhances both charge donation and acceptance and that the graphene appears to be functioning as a solid-state ligand. Furthermore, the enhanced binding after deposit Pd on graphene is also associated with the distance from the Pd active site to the graphene lattice which also confirmed by experiments (135).

3.3.4 Bonding and antibonding state effects on the activation energy

To further examine the effect of the graphene support on the catalytic activity, we examined the position of the bonding and antibonding orbitals at the transition state that controls the breaking of the Br-C bond. The active site for a transition metal atom for covalent bond cleavage typically contains a d_z^2 orbital that forms a 3-center bonding orbital that stabilizes the stretched bond, and a d_{xz} antibonding orbital that breaks the bond. The orbitals are shown in Figure 3.9 lists the energy of the level. Both the bonding and antibonding orbitals reveal a substantial stabilization of about 0.5 eV upon absorption when supported on defected graphene. The stabilization of the active orbitals can be attributed to the positively charged state of the deposited cluster.

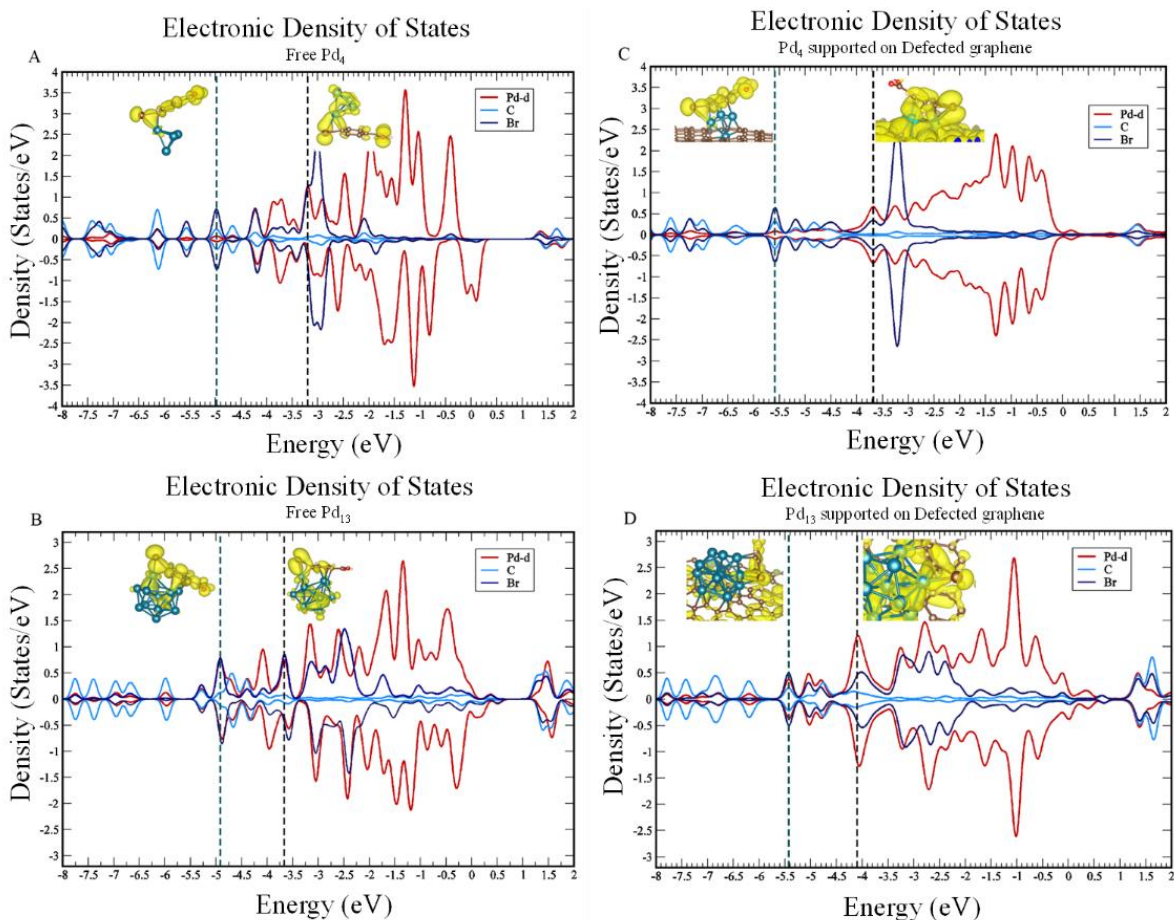


Figure 3-9 shows the 4d Pd atom at the active site, C, and Br orbital electron density of states of the Pd atom at the active site at the transition state of free Pd₄, Pd₁₃ and supported Pd₄ and Pd₁₃ respectively in an oxidative addition reaction. Both the bonding and antibonding state are shifted left by 0.5eV after deposit the Pd₄ and Pd₁₃ cluster on defected graphene.

A similar conclusion is also reached for the reductive elimination step. Figure 3.10 shows the density of states of Pd₄ and Pd₄/G at the transition state for reductive elimination. The bonding and antibonding orbitals that control the formation of the C-C bond are significantly stabilized by the presence of the defected graphene. The stabilization is due to the positively charged state of the supported cluster as the support makes the catalyst a superior charge acceptor.

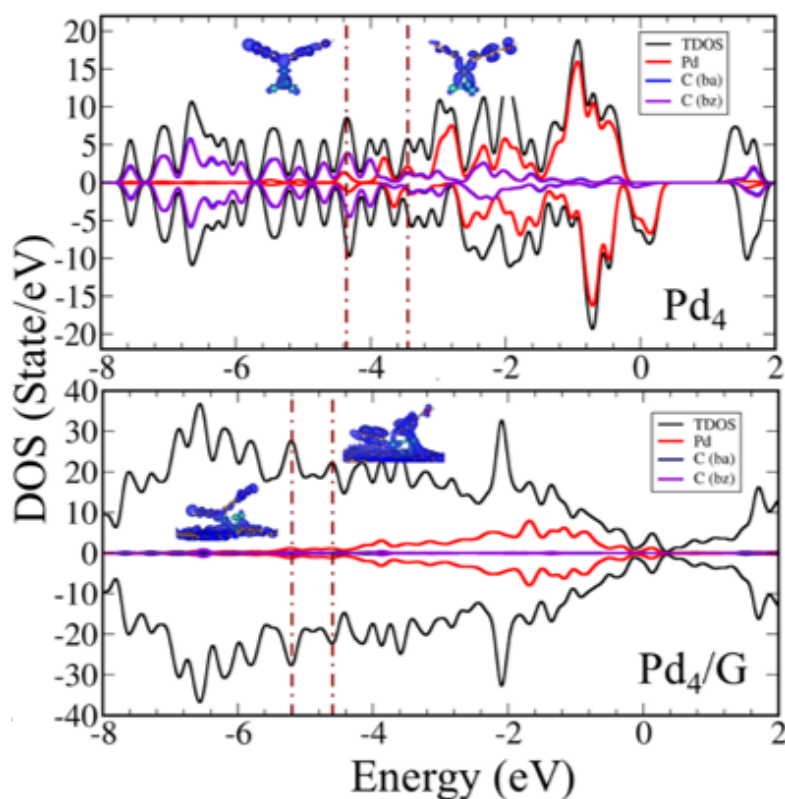


Figure 3-10 Density of States (DOS) and bonding/antibonding orbitals at the transition state for the reductive elimination of Pd₄ and Pd₄/G. (ba= benzoic acid, bz= benzene).

3.4 Conclusion

In this chapter, we performed theoretical calculations to understand the key factors affecting the activation energy in each step of the Suzuki reaction catalyzed by naked free Pd_n clusters as well as Pd clusters supported on a double defected graphene. The structure analyzing of the intermediates indicates the lower coordination Pd site within the Pd cluster is ideal to conduct the reaction in oxidative addition and reductive elimination steps resulting from the adjacent Pd atoms to the active Pd site trap the reagent which lead. This study also provides a framework for understanding the dramatic increase in catalytic activity that can be achieved by optimizing the electronic interactions between the metal cluster and the conducting support. Theoretical

investigations demonstrate that the resulting metal-ligand interaction promotes electron flow between the metal cluster and the defected graphene. This is clearly due to the conductive nature of the support that actively enhances charge transfer to and from the reactants. However, the benefit of the support substrate is diminished if the metal is weakly immobilized. We anticipate that the bifunctional nature of graphene defect supported catalysts might be applied to a wide range of multi-step reactions that incorporate both oxidative and reductive reaction steps.

Chapter IV DFT study of different transition metal clusters supported on defected graphene for cross-coupling reaction

4.1 Introduction

C-C and C-heteroatom cross-coupling reactions catalyzed by Palladium-based catalysts have made a tremendous impact in organic synthesis since their discovery. These reactions typically form C-C or C-heteroatom bond from an aryl-halide and an organometallic precursor mediated by ligated Pd salt. More recently, the implementation of Pd clusters and nanoparticles as catalyst open a new era due to their high reactivity, sustainability, recyclability and less metal contamination in the product (45, 133, 136). The possibility of substituting expensive Pd catalyst with earth abundant and less expensive first-row transition metal, such as Ni, Fe, and Cu, is apparently even more appealing (137-139). Take Ni as an example: Ni is a commodity metal with a cost of roughly \$1.20 per mol, whereas Pd and Pt are precious metals, which command a significantly higher price of \$1,500 and \$10,000 per mol, respectively (140). However, Ni is not only a less developed and low-cost substitution of Pd. Owing to their strong charge donating capability, the first-row transition metals are potential to activate strongly energetically hindered bonds such as C-Cl, C-F, C-OR, and C-NR (139-147). However, despite the immense advancement of nanoparticles and clusters catalysis in the past decade, when the first-row transition metals nanoparticles were applied, the reactions usually require excess ligand and coupling partner, harsh reaction condition and a stoichiometric amount of metal which have hindered the development and application of such catalysts (18, 148-151).

Graphene has been proven to actively assist the cross-coupling reaction when it is used as a support substrate to immobilize ultra-fine Pd nanoparticles or clusters in previous studies. In the

complex reaction cycle involving multiple redox steps such as cross-coupling reaction, the graphene support serves as a solid-state ligand facilitating the charge transfer in each step in the reaction owing to its conductive nature (134). To extend the Pd/graphene system to other earth-abundant metal, it is important to understand the interaction between the graphene and the first-row transition metal clusters and their reaction mechanisms in the cross-coupling reaction.

We carried out a meticulous study to investigate the properties of Ni, Fe and Cu clusters supported on defected graphene catalysts as well as how their reaction barriers compare to Pd in the full Suzuki reaction cycle using density functional theory. One significant drawback of the first-row metal catalysis is that the metal clusters are easy to be oxidized which leads to loss of reactivity (152-154). Our result of this study reveals that the electron properties of the metal cluster have been modified after supported the cluster on graphene: the metal cluster and the defected graphene form a charge donor and acceptor pair which stabilize the metal cluster. The study of the full reaction cycle of Suzuki reaction also suggested that the activation energies in the electron withdraw steps are significantly curtailed after support the metal clusters on defected graphene. And by tuning the ratio of the metal cluster size and defect size, Ni clusters have great potential to replace Pd.

4.2 Method

The theoretical studies used a gradient corrected functional proposed by Perdew et al. The VASP code was used, and the Kohn–Sham orbitals were expanded using a plane wave basis set and the cutoff was set to 400 eV. The projector-augmented wave method was used to treat electron-ion interactions. Van der Waals correction (DFT-D2) was applied. A dipole correction was incorporated along the z-axis of the slab, and that Gamma point is used for Brillouin zone integration. Since Fe_n , Cu_n , and Ni_n clusters carry magnetic moments, various spin states were

investigated to determine the ground state. Bader charges were used to determine the charge of the individual atoms. Nudge elastic band method was applied to optimize the reaction pathway.

4.3 Result and discussion

4.3.1 Stability of Ni, Cu, and Fe cluster supported on defected graphene

To screen metal-graphene combination possess similar electronic property to the Pd/graphene, we started this research with the stability study of different metal clusters supported on the double vacancy defect site as shown in Fig 4.1. For the case of Au₁₃ and Mo₁₃ clusters, the binding energies of the metal clusters to the graphene are 4.2 eV and 4.3 eV respectively which are much lower than the binding energy of Pd₁₃ cluster to the graphene. The lower binding energy not only suggests that the structure is less stable but also indicates the metal cluster has much lower charge donating capability since the graphene is a charge acceptor. In contrast, the binding energy of Ru₁₃ cluster to the graphene support is significantly higher than it of the Pd₁₃ cluster to the graphene which indicates the charge donating capability of the metal is strong and the charge reception capability of the metal cluster is poor. Since the reaction that interests us is a complex reaction cycle which contains both charge donation and charge withdrawn steps, Ni₁₃, Fe₁₃ and Cu₁₃ clusters with the similar binding energies of metal to the graphene support comparing with the binding energy of Pd₁₃ cluster to the graphene which predicts similar reaction barrier in the Suzuki reaction are our choice to proceed with in this research.

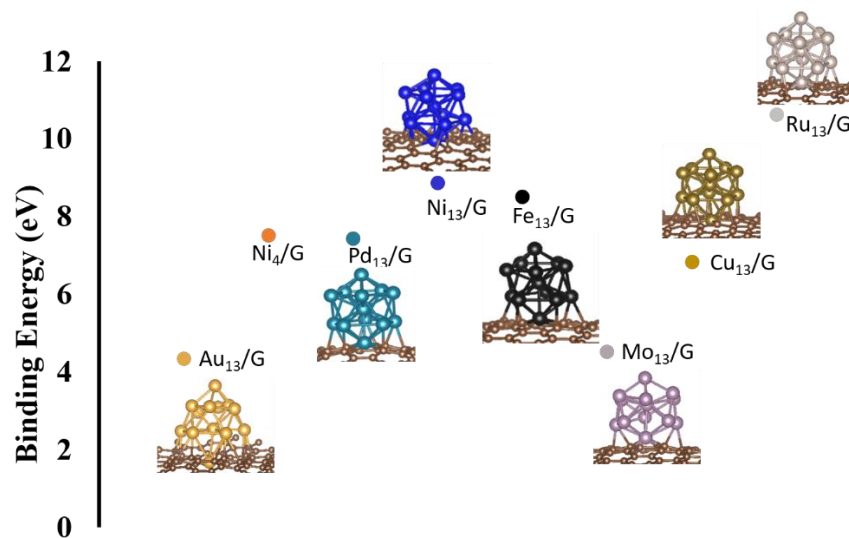


Figure 4-1 Binding energies of Au₁₃, Ni₁₃, Fe₁₃, Mo₁₃, Cu₁₃ and Ru₁₃ clusters supported on the double vacancy defect on graphene.

To further probe the interaction between the metal and the support substrate, we first examined the structure of Pd₁₃, Fe₁₃, Ni₁₃ and Cu₁₃ cluster binding to a double vacancy defect graphene sheet. The thirteen cluster is the first geometric closed structure. And the size of the cluster is approaching nanometer. Furthermore, based on the previous studies, the Pd₁₃ cluster on defected graphene is highly stable. As shown in Fig 4.2 and Table 4.1, strong interactions between the metal clusters and defect site are exhibited: for Ni₁₃ and Fe₁₃ clusters, the binding energies of the clusters and the graphene are more than 8.5 eV. It is important to note that the energy requirement for leaching one carbon atom from the graphene lattice is about 7.8 eV. Other than the binding energy of the whole cluster to the graphene, the internal binding energies of the metal atoms inside the cluster are also significantly enhanced after deposition. Usually, shorter bonds lead to stronger binding. However, the case of Cu₁₃ is different. Both the free Cu cluster and the supported cluster are even less stable than the corresponding free and supported Pd cluster which may lead to strong metal leaching during the reaction.

The other sign of the strong interaction between the metal cluster and the support is charge transfer. In the case of a Ni₁₃ cluster, 2.01 e⁻ charge flowed from Ni cluster to graphene. The electron flow changes the magnetic moment of the metal clusters which also can be observed through the change in the density of the state (DOS) after the deposition. Fig 4.1 E shows the charge density change after binding Pd₁₃ cluster to the defected graphene. The charge density change clearly presents how the Pd-C bonds are formed and where the charges are originally from. The charge density change on each individual Pd atom shows a strong correlation to the distance from the atom to the defect center. However, even top the Pd exhibit slight charge density deform under the presence of graphene. The modified electron property may significantly affect the reactivity of the metal cluster.

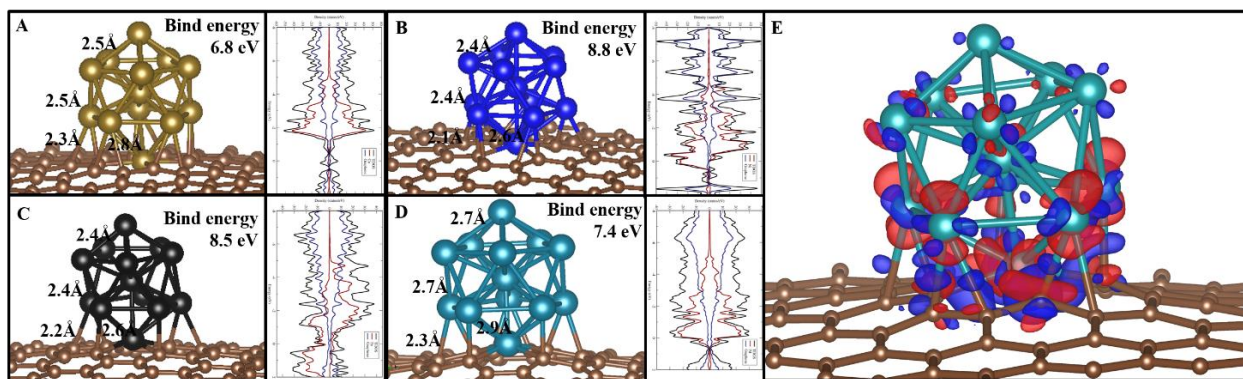


Figure 4-2 Structure, selected bond length, binding energies to graphene and density of state of supported Cu₁₃ (A), Ni₁₃ (B), Fe₁₃ (C), and Pd₁₃ (D). Figure (E) shows charge density deformation of the Pd₁₃ cluster before and after deposition on graphene. Blue shows new charge density after deposition and red indicates the origin of that charge.

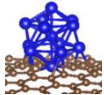
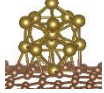
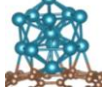
Metal cluster	Structure	Avg. Binding energy	Magnetic moment (μB)	Graphene binding energy (eV)	Charge transferred to graphene (e^-)
Ni_{13}		3.27	8	-	-
Ni_{13}/G		3.95	10	8.8	2.09
Fe_{13}		3.72	44	-	-
Fe_{13}/G		4.37	36	8.5	2.85
Cu_{13}		2.30	5	-	-
Cu_{13}/G		2.85	1	6.5	1.90
Pd_{13}		2.41	6	-	-
Pd_{13}/G		2.94	2	7.4	1.10

Table 4.1 Average internal binding energy, magnetic moment, binding energy and charge transferred to graphene of free and supported Fe_{13} , Cu_{13} , Ni_{13} and Pd_{13} clusters.

4.3.2 Electronic structure change after deposition

In order to examine the change of electronic property of the metal cluster after deposition, we then calculated the work function and the metal D band center for the free and supported clusters, as shown in Fig 4. 2 The work function is an indication of the minimum energy required to remove one electron from the metal cluster. And it usually can be tuned by engineering specific dipole of the metal cluster: deposit the metal cluster to a strong electronegative supporting surface like defected graphene is one way to modify the work function. As a result, the work function for all

the metal clusters increased after deposition, which indicates the charge donation capability of the supported clusters is diminished. It is surprising that the increase of the work function of the Pd₁₃ cluster is negligible (0.006eV). And the increase in the work functions is more significant for the more reactive free clusters. It is also important to note that after deposit, the work function of the Ni₁₃/graphene cluster is close to the free Pd₁₃ cluster and the work function of the Fe₁₃/graphene cluster is similar to the free Cu₁₃ cluster. Another suggestion from the change in work function is the metal clusters are more stable against oxidation after deposition which assists remaining their valence state during synthesis and reaction. The D band center model has also proven to be practical in analyzing bond formation and trends in reactivity in transition metals. D band center is an indication of the antibonding energy level when adsorbates form bonds with the surface metal. Higher metal D band center (relative to Fermi energy) corresponds to a higher metal-adsorbate antibonding energy level which leads to less destabilized metal-adsorbate bond. As shown in figure 4.2A, it is clear that the D band center for all the metals shifted deeper after deposition on graphene which would destabilize the adsorbate-metal bonding. Since the work function and changes are mainly caused by charge transfer between graphene and metal clusters, Fig 4.2 B shows that the net electron flows have a strong correlation with the amount of work function change.

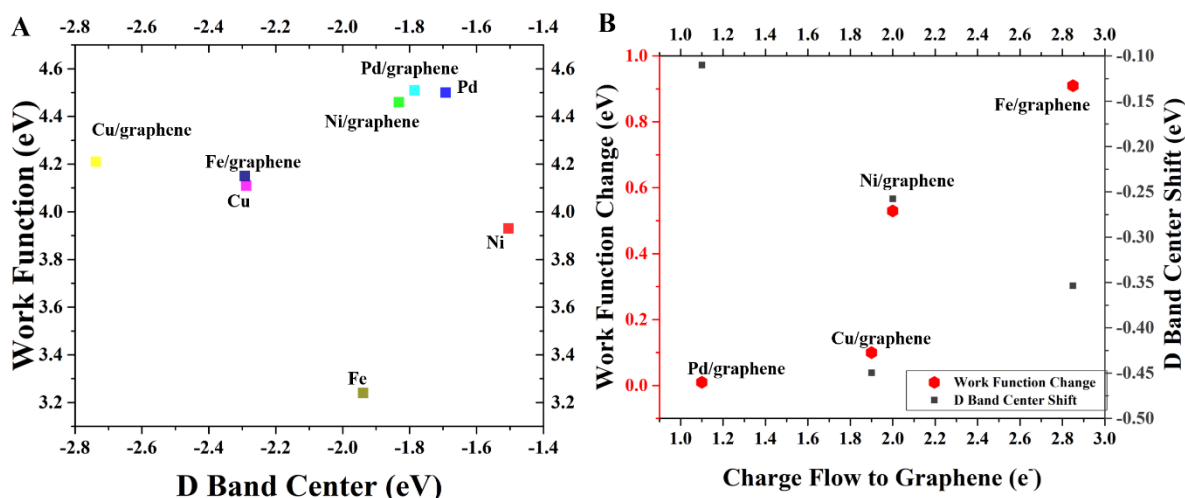


Figure 4-3 (A) D band center and the work function of free and supported Fe₁₃, Cu₁₃, Ni₁₃ and Pd₁₃ clusters. (B) D band center shift and work function change as a function of charge flow to graphene after deposit Fe₁₃, Cu₁₃, Ni₁₃ and Pd₁₃ clusters on defected graphene.

To further confirm the variation of the electronic property after deposition, we then test the adsorption energy of bromine, dehydrated benzoic acid and trimethyl phosphine on different free and supported metal clusters. Aryl-halide is a commonly used compound in cross-coupling reaction. The adsorption energy of the segment aryl and halide compounds provide a direct indication of the activation energy in the reaction. Both the bromine and benzoic acid are charge acceptors after binding to the metal cluster. Phosphine is an electron-rich molecule, and usually serves as a ligand in the cross-coupling reaction, which we used to test the electron withdrawing capability of the metal clusters. As shown in fig. 4.3 A, bromine binding energy is negatively corresponding to the charge donation capability of the cluster in the means of work function. It is reasonable to suggest the bromine binding energies would significantly decrease for the supported species since the work function dropped after deposition. However, except for Ni₁₃ cluster, the bromine binding energies for all other metal clusters considerably increased after depositing the cluster on graphene. One possible explanation for the increase in binding energy is the electrons

withdrawn by defected graphene serve as a reservoir facilitating the charge transfer. The other possible reason is the negatively charged defect graphene and positively charged metal cluster created a strong dipole structure which enhanced the attraction to other strongly negatively charged species of the metal clusters. In contrast, phosphine binding energy, as a sign of the capability of charge acceptance of the clusters, is positive corresponding to work function of the cluster. And deposition of the clusters increased phosphine binding energies. For the benzoic acid binding energy to the metal clusters, the carbon-metal sp-d orbital hybridization plays an important role as shown in Fig. 4.3 B. The deposition of the metal clusters on graphene depresses the metal D band center and hence reduces the benzoic binding energies.

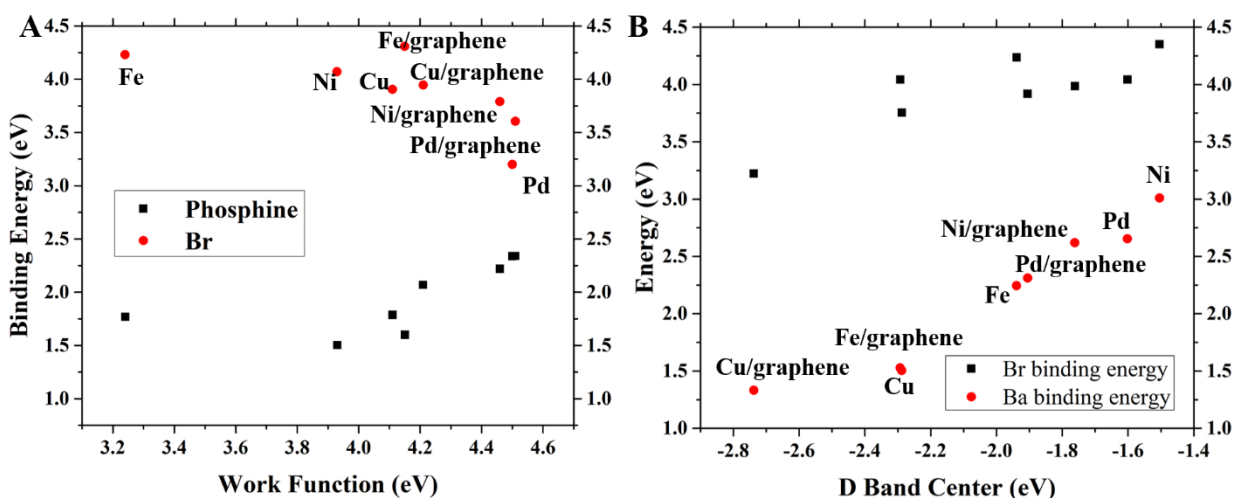


Figure 4-4 Bromine and trimethylphosphine binding energy of free and supported Fe₁₃, Cu₁₃, Ni₁₃ and Pd₁₃ clusters correspond to work function of the metal clusters. (B) Bromine and benzoic acid binding energy of free and supported Fe₁₃, Cu₁₃, Ni₁₃ and Pd₁₃ clusters as a function of metal D band center.

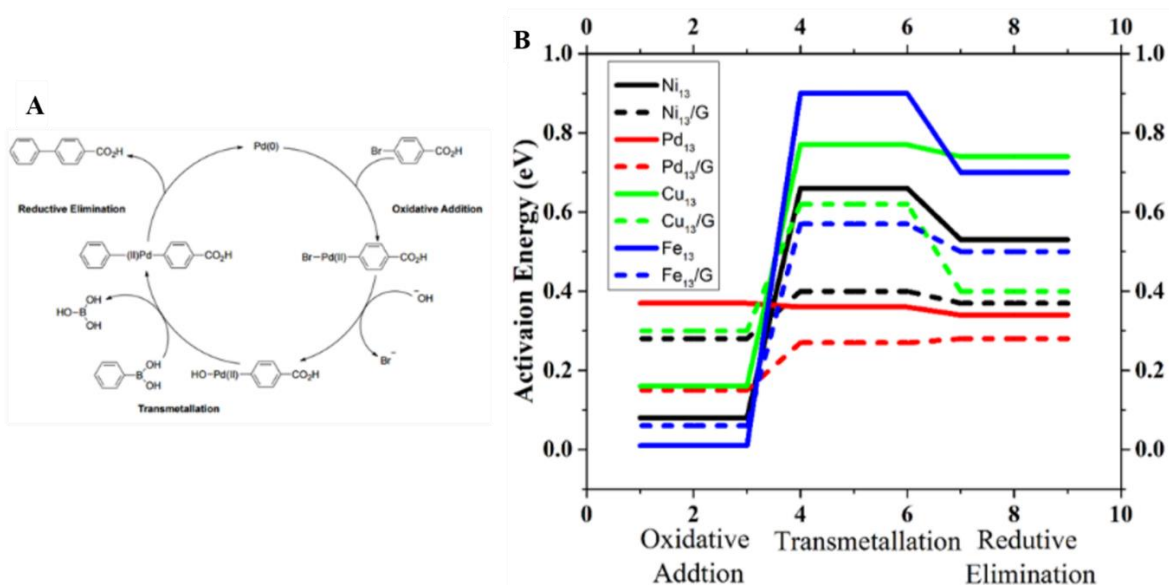
Metal cluster	Work Function (eV)	D band Center (eV)	Bromine Binding energy (eV)	Benzoic acid Binding energy (eV)	Phosphine Binding energy (eV)
Ni ₁₃	3.93	-1.50411	4.0705	4.3513	1.5041
Ni ₁₃ /G	4.46	-1.83174	3.79	3.9859	2.2195
Fe ₁₃	4.5	-1.69176	3.2007	4.0431	2.3396

Fe ₁₃ /G	4.51	-1.78533	3.6057	3.9191	2.341
Cu ₁₃	4.11	-2.28803	3.9059	3.7541	1.7866
Cu ₁₃ /G	4.21	-2.73769	3.9459	3.2221	2.0704
Pd ₁₃	3.24	-1.93896	4.2309	4.2374	1.8686
Pd ₁₃ /G	4.15	-2.29257	4.3098	4.0429	1.6006

Table 4-2 Work function, D band center, Br binding energy, benzoic acid binding energy and trimethylphosphine binding energy of Fe₁₃, Cu₁₃, Ni₁₃ and Pd₁₃ clusters before and after deposit on the graphene.

4.3.3 Full reaction cycle of Fe_n, Cu_n, Ni_n clusters catalyzed Suzuki reaction

Finally, we tested the free and supported clusters in full reaction cycle of Suzuki reaction, one of the most impacted cross-coupling reaction, using the nudged elastic band method. The Suzuki reaction usually proceeds in three steps: oxidative addition, transmetallation, and reductive elimination. The catalyst acts as a charge donor in oxidative addition step and the first part of the transmetallation step. Then in the second part of transmetallation and reductive elimination steps, the catalyst serves as a charge acceptor which finally form the carbon-carbon bond and release the product. The reaction mechanism is shown in fig. 4.4 A. The activation energies and intermediate structures are presented in fig. 4.4 B and Table 4.3.



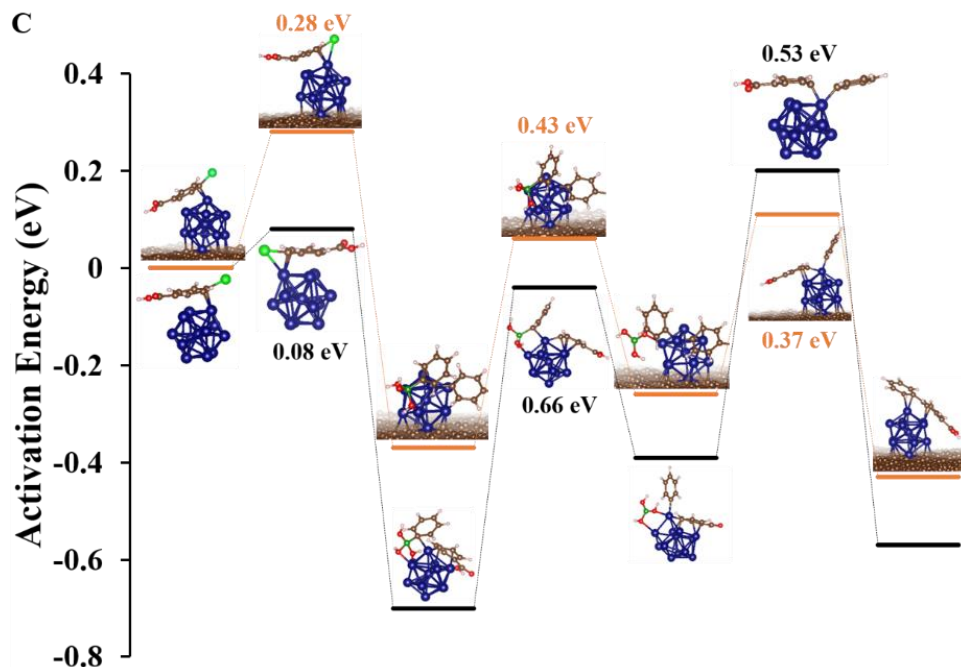


Figure 4-5 (A) Reaction mechanism of Suzuki reaction. (B) Activation energies of free and supported Fe, Cu, Ni and Pd clusters in full reaction cycle. (C) Structure of intermedia of free and supported Ni₁₃ cluster.

Metal cluster	Activation energy (eV)		
	Oxidative addition	Transmetalation	Reductive elimination
Ni ₁₃	0.08	0.66	0.53
Ni ₁₃ /G	0.28	0.43	0.37
Pd ₁₃	0.37	0.36	0.34
Pd ₁₃ /G	0.15	0.27	0.28
Cu ₁₃	0.16	0.77	0.74
Cu ₁₃ /G	0.3	0.62	0.4
Fe ₁₃	0.01	0.9	0.7
Fe ₁₃ /G	0.06	0.57	0.5

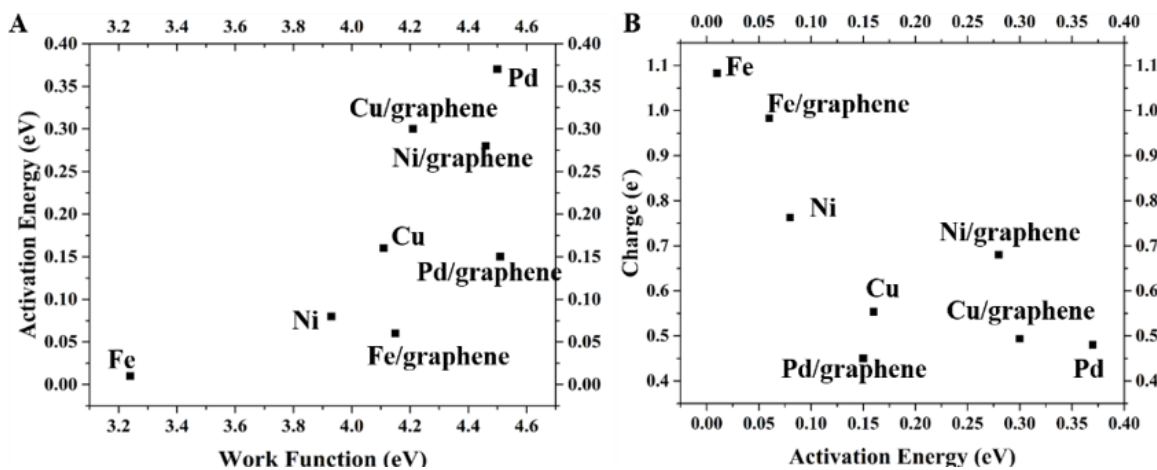
Table 4-3 Activation energies of Ni₁₃, Pd₁₃, Fe₁₃, and Cu₁₃ in a full reaction cycle of Suzuki reaction.

In the charge donating oxidative addition step, for the free clusters, the activation energy of the first-row transition metal clusters are significantly lower than that of the Pd₁₃ cluster. And the trend of the activation energy is strongly correlated to work function and bromine adsorption energy.

Fe₁₃ cluster exhibits extremely low activation energy suggesting a strong charge endowment capability of this species. After deposit, the metal clusters on the defected graphene, the activation energy for Fe₁₃, Cu₁₃ and Ni₁₃ clusters increased. In contrast, Pd₁₃ on graphene shows lower activation energy than a free Pd₁₃ cluster. Since the breaking of the Br-C controlled by both the charge donation capability of the metal cluster which is mainly corresponding to the Br adsorption energy as well as the metal-benzoic acid stability which is strongly related to the metal D band center, we found the change of the activation energies is able to be well defined by the Br adsorption energy change and metal D band center change. For Ni₁₃/graphene cluster, after deposition, both the Br binding energy and the D band center of Ni cluster have been decreased drastically. As a result, the reactive barrier for the Ni cluster increased significantly. For Fe and Cu clusters, although the Br binding energies raised slightly, the D band center shifts to deeper energy level are more compelling. The activation energies for those species are considerably increased. For Pd cluster, after supported on graphene, the metal D band center shift slightly deeper and the Br binding energy hikes 0.4 eV which is contributed to the activation energy drop. It is interesting to note that the energy gain difference before and after deposition in this step is also following the same pattern.

As an opposite charge flow process of oxidative addition, the reductive elimination step requires the catalyst to serve as an electron acceptor. As shown in fig. 4.5 D and E, metal cluster with higher work function and higher D band center forms less destabilized biphenyl composite and possess lower activation energy. All activation energies dropped after deposit the metal clusters on defected graphene. More significant change in the metal D band center and metal-Br binding energy lead to a higher decrease in the activation energies. For the case of free Cu₁₃, since the internal binding energy of free Cu cluster is low, the Cu₁₃ cluster experiences significant structural deformation

which leads to severely trapping of the biphenyl starting materials by changing the Cu-C sp² bond angle and forming multiple copper carbon bonds. In contrast, after deposition, Cu₁₃ cluster becomes more stable and the activation energy drop is drastic. For the transmetallation step, although the metal clusters experience both charge donation and acceptance process, the activation energies are dominated by the charge withdrawal capability of the metal cluster which is also reflected by net charge gain of the metal during this step. As a result, in this step, the different metal clusters behave similarly to those in the reductive elimination step. The activation energy change is controlled by the work function change after supported by graphene. In summary, after deposition, the activation energies increased slightly for the first-row transition metal in oxidative addition step. However, in the rate determining transmetallation and reductive elimination steps, support the metal clusters dramatically decreased the activation energies: as an example, the activation energy dropped 0.23 eV (40%) in the rate determining step and the overall activation energy declined for 0.22 eV. The activation energy for supported Ni cluster is close to free Pd clusters.



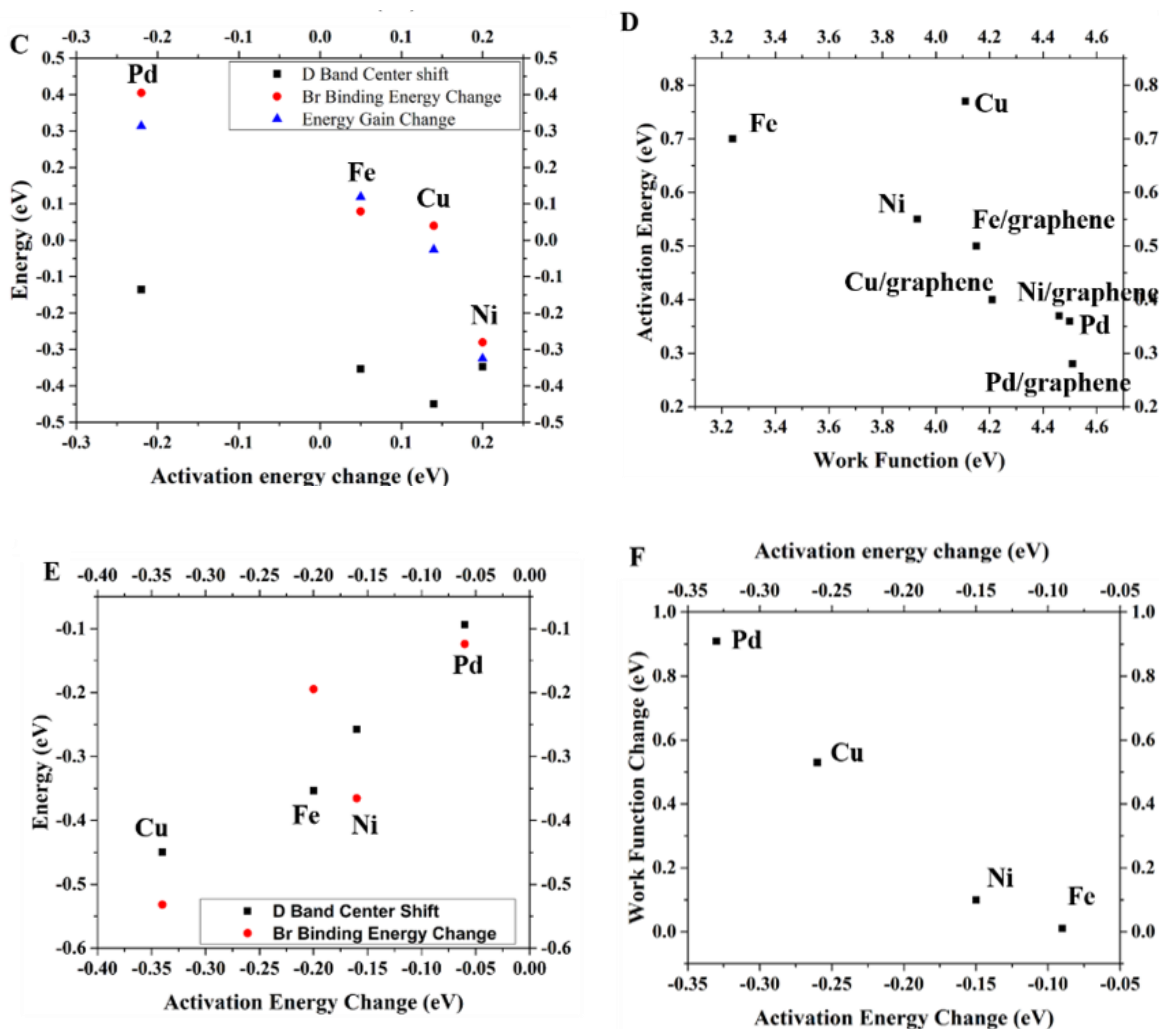


Figure 4-6 Activation energies of free and supported Fe, Cu, Ni and Pd clusters correspond to work function of the cluster (A) and charge transfer to the 4-bromobenzoic acid reagent in the transition state (B) in oxidative addition step. (C) Metal cluster D band center shifts, bromine binding energy changes and net energy gain changes affect the activation energy of the metal cluster after deposition in oxidative addition step. (D) Activation energies of free and supported Fe, Cu, Ni and Pd clusters correspond to work function of the cluster in reductive elimination step. The activation energy changes are controlled by metal D band center shift and metal-Br binding energy change after deposition in reductive elimination (E) and transmetalation (F) step.

The case of Ni₁₃ cluster supported on catalyzed Suzuki reaction is particularly interesting since the activation energy of the rate determine transmetalation step is only 0.42 eV which is close to

the free Pd₁₃ cluster. In fact, homogenous Ni-catalyzed cross-coupling has been extensively studied (155-159). Next, we decided to further our understanding of the Ni cluster supported on graphene and try to decrease the overall activation energy of Ni/graphene in the full reaction cycle. For this purpose, two approaches interest us: the first approach is tuning the size of the Ni cluster, the second approach is mixing a certain amount of Pd atom into the Ni cluster. For the first approach, we started with switching the Ni₁₃ cluster to a Ni₄ cluster.

Ni₄, a small tetrahedron cluster, was immobilized to a double vacancy defect site on graphene. By switching the large thirteen cluster to a smaller Ni₄ cluster, two effects are enhanced. The first one is the charge transfer between the graphene surface and the metal active site is enhanced since the distance from the active site to the graphene is much shorter. The second effect is the switching generated a more positively charged metal cluster which would facilitate the charge withdrawing reaction steps. The binding energies of bromine and phosphine to the free and supported Ni₄ cluster was tested subsequently. It is surprising that both the Br and phosphine binding energies are increased by 0.23 eV and 0.28 eV respectively after the Ni₄ cluster was deposited on graphene. In contrast, the Br bind energy is dropped by 0.3 eV in the case of the Ni₁₃ cluster. The reason for the difference of binding energy changed after deposition between the Ni₄ cluster and the Ni₁₃ cluster is mainly due to the first effect that the charge transfer enchantment from the graphene is enhanced. Comparing with a neutral cluster, the charge donating capability of a positively charged cluster is usually diminished which indicate the Br binding energy should be reduced instead of increased after the deposition.

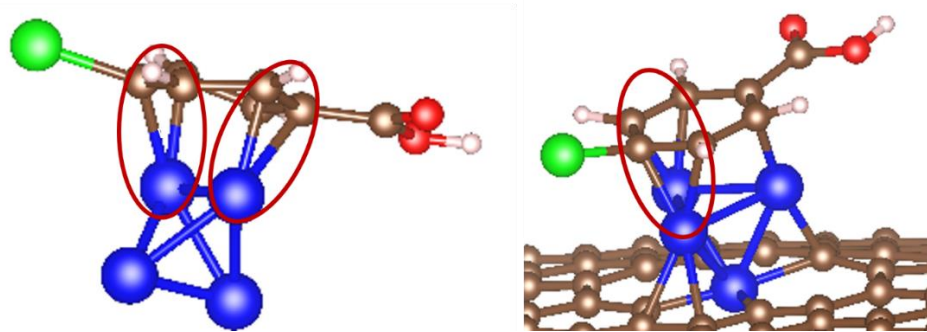


Figure 4-7 The sterically hindered C₂-Ni-Ni-C₂ structure obstructs the breaking of Br-C bond in the free and supported Ni₄ cluster.

We then calculated the activation of a full reaction cycle of free and supported Ni₄ cluster. The result is shown in Fig. 4.7. Both the activation energy in charge withdraw step and charge donating step are reduced after deposition which is consistent with our previous conclusion that the defected graphene serves as an electron reservoir actively assisting charge transfer. It is important to note that using Br and phosphine binding energy as an indication of charge transfer capability of the metal catalyst to predict activation energy is relatively accurate. However, the impact of the geometric structure of the active site on the activation energy cannot be reflected by the Br or phosphine binding energies. The activation energy of free Ni₄ cluster hiked to more than three times compared with a free Ni₁₃ cluster in oxidative addition step. Structure of the active site is the origin of this increase. In the case of the Ni₄ cluster, when the Ni₄ cluster binds to the aryl reagent, two of neighboring Ni atoms in the cluster form multiple Ni-C bonds with the carbon atoms in the two parallel apexes of the sp² C-C bond in the benzoic acid which obstruct the rotation of the bromobenzoic acid molecular to form a Ni-Br bond as shown in fig 4.6. This situation is not pertinent to the free Pd₄ cluster since Pd-Pd bond is not short enough to form the C₂-Pd-Pd-C₂ structure. The energetically hindered C₂-Ni-Ni-C₂ structure is also observed in the supported Ni₄ cluster in the oxidative addition step. However, the charge donating process is enhanced by

graphene support. As a result, the activation energy of supported Ni₄ cluster decreases by 0.04 eV. In the charge withdrawing transmetallation and reductive elimination step, the activation energies drop by 0.18 eV (35%) and 0.32 eV (90%) respectively after deposition. It is surprising that the activation energy in the final reductive elimination step is curtailed by 90 percent. One reason besides the two effects mentioned before which also reduces the activation energy in the final reductive elimination step in the Ni₄ catalyzed reaction is the carbon-carbon distance in the initial stage before forming the bond is much shorter than the case of Pd₄ and Ni₁₃ cluster.

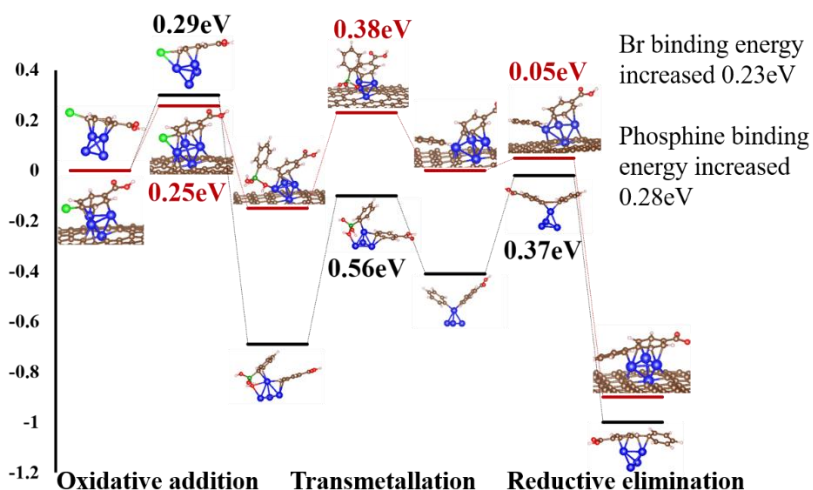


Figure 4-8 The normalized total energies and the atomic structures of the free and supported Ni₄ clusters in the Suzuki reaction.

For the second approach to reducing the activation energy of the supported Ni₁₃ cluster is mixing a certain amount of Pd atoms to the Ni cluster to generate a bimetallic cluster. We started with the research of the Ni/Pd bimetallic cluster with the Ni₁₂Pd₁ and Pd₁₂Ni₁ clusters as shown in fig 4.8. When different metal atoms are contained in the same cluster, one assumption is the different steps in the reaction could be carried out on different active site. Since the Ni active site has low activation energy for the charge donating step and the Pd site has low activation energy for the charge withdrawing steps. One challenge for this co-catalysis system is the energy barrier

to allow reaction intermediate transferred between the different active site. This co-catalysis assumption is not adopted by this study since we found the electronic property of Pd and Ni individual active site changed significantly in the bimetallic cluster. Fig 4.8 shows the activation energies of the free and supported $\text{Ni}_{12}\text{Pd}_1$ and $\text{Pd}_{12}\text{Ni}_1$ clusters. One important finding is that in the free Pd/Ni cluster, the Pd site would donate charges to the neighboring Ni sites and become positively charged. The Ni site accepts charges from Pd and becomes negatively charged. The activation energy of the bimetallic cluster in the full reaction cycle, as well as the binding energies of Br and phosphine, suggests that the tendency of the reactivity of the different active site is: for the charge withdrawing steps, activation energy $\text{Pd} < \text{Ni}^+ < \text{Pd}^- \ll \text{Ni}$, and for the charge donating steps, the activation energy follows the trend as $\text{Ni} \ll \text{Ni}^+ < \text{Pd}^- < \text{Pd}$. For both of the charge donating and accepting steps, Ni^+ active site possesses relatively low activation energy.

After evaluating the previous two approaches, we decided to merge those methods to work with a small bimetallic cluster, the Ni_2Pd_2 cluster. The Ni_2Pd_2 cluster is a symmetric cluster. And as the same as the situation of $\text{Ni}_{12}\text{Pd}_1$ and $\text{Pd}_{12}\text{Ni}_1$ clusters, in the Ni_2Pd_2 cluster, Ni site accepts charges from Pd becoming negatively charged and the Pd site donates charges and becomes positively charged. Table 4.8 shows the structure and charge state of the free and supported Ni_2Pd_2 clusters. Two possible structures are available when the Ni_2Pd_2 cluster is binding to the double vacancy defected graphene: Binding one Pd atom as the anchor site or binding one Ni atom as the anchor site. Using Ni as anchor site generates more stable clusters ($\text{Ni}_2\text{Pd}_2/\text{graphene}$). However, both of the two formations are tested in a full reaction cycle of the model Suzuki reaction.

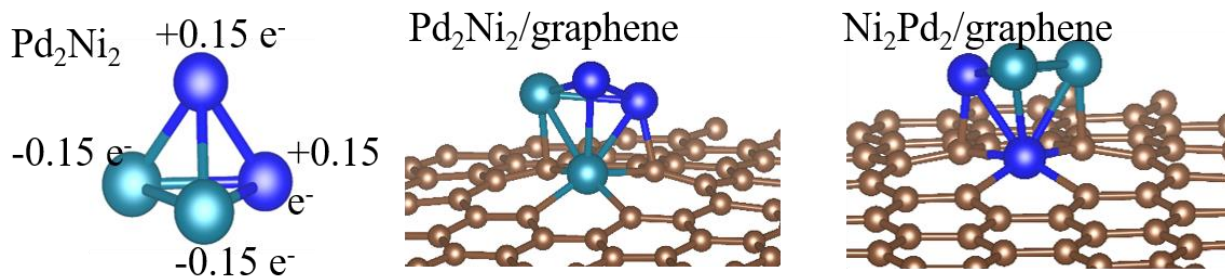


Figure 4-9 Structure of Pd₂Ni₂ cluster and the two corresponding supported Pd₂Ni₂ clusters.

The resulted in reaction barriers for the three steps Suzuki reaction using the free and supported Ni₂Pd₂ clusters are listed in table 4.4. The reaction barriers of the free and supported Pd₄ and Ni₄ clusters are also listed for comparison. For the first step in the Suzuki reaction, for both free and supported the Ni₂Pd₂ clusters the reaction barrier is higher than the corresponding free and supported Pd₄ clusters. The increased reaction barriers for the Ni₂Pd₂ clusters result from the stereo hindered structure of the carbon-Ni-Ni-carbon bonds formed by the metal cluster and the reagent where a similar situation also occurred for the Ni₄ cluster. For the charge withdrawing transmetallation and reductive elimination step, the reaction barrier for the Pd₂Ni₂/G cluster, which is using the Pd atom as the anchor site and the Ni site as the active site, is surprisingly low. This calculation is confirmed that the positive charge Ni site is a better charge acceptor than the negatively charge Pd site.

Metal cluster	Oxidative addition (eV)	Transmetallation (eV)	Reductive elimination (eV)
Ni ₂ Pd ₂	0.37	0.34	0.22
Pd ₂ Ni ₂ /G	0.11	0.12	0.017
Pd ₂ Ni ₂	0.16	0.42	0.21
Ni ₂ Pd ₂ /G	0.22	0.21	0.11
Pd ₄	0.21	0.3	0.2
Ni ₄	0.35	0.66	0.26
Pd ₄ /G	0.08	0.16	0.12
Ni ₄ /G	0.3	0.39	0.1

Tab 4.4 The reaction barrier of the model Suzuki reaction using the free and supported Ni₂Pd₂ clusters and free and supported Pd₄ and Ni₄ clusters.

4.4 Conclusion

The theoretical calculations probed the interactions between defected graphene and different metal clusters in the graphene supported Ni, Fe and Cu clusters catalyst. Electronic properties of the metal clusters have been modified after supporting the metal clusters on the defected graphene which also lead to change in the activation energy of the catalyst in Suzuki reactions. Ni clusters supported on graphene defects have the lowest activation energy in the rate-determining step. By tuning the size of the Ni cluster or mixing a certain amount of Pd into the Ni cluster, the activation energy of graphene supported Ni or Pd/Ni is further reduced. Some of this bimetallic lowering of the activation energy is due to the charge transfer from the Pd to the Ni resulting in the Pd being enhanced in charge donating steps of the reaction, while the Ni sites are enhanced in the charge accepting steps.

Chapter V Pd nanoparticles/clusters supported on graphene as an efficient and sustainable catalyst for Suzuki reaction

5.1 Introduction

The finding in the theoretical calculation suggests the presence of the vacancy defect site is critical to immobilize the metal nanoparticles. The graphene support is functionalized as solid-state ligand actively assisting the charge transfer in the multiple charges donating and withdrawing steps in a complex reaction cycle. It is important to experimentally verify the theoretical results. Furthermore, under the guidance of the theoretical work, the next work started with the optimization of the Pd/graphene catalyst by engineering the defect site on graphene as well as tuning the interaction between the metal nanoparticles and the support substrate.

In homogeneous catalysis, the reactivity and selectivity of the catalyst can be tuned by using ligands, such as phosphines, amines, and carbenes (*160-164*). Recently developed electron rich and bulky structure phosphines ligands have proven to significantly facilitate the reaction (*37, 163, 165, 166*). Ligand design has been the critical driving force to improve catalytic reactions under mild and environmentally benign conditions. Although the discussion on the exact coordination of Pd and ligands, which is associated with ligands attachment, detachment, and isomerization, in each step (oxidative addition, transmetallation, and reductive elimination) of the reaction is not completely understood, a fundamental consensus of catalytic mechanism has been established (*118, 127, 167*). In contrast, in ligand-free heterogeneous catalysis, controversial catalytic mechanisms have been proposed in different works. A true “heterogeneous” mechanism, in which the reaction is carried out on the surface of the supported Pd_n nanoparticles, was proposed by Ellis, Jason, Wang and Li (*93, 168-171*). Alternative studies suggested a “homogenous” mechanism in which

a soluble Pd atom or small cluster leaching from the metal particle acts as the true catalytic active Pd species (44, 167, 172, 173). Some other works have suggested that the metal leaching is promoted by the oxidative insertion step. And, the leached Pd species is the Aryl-Pd-halide intermediate. As a result, under this mechanism, the reaction is partially homogenous and heterogeneous (43, 44, 127, 174-177). Since all three reaction mechanisms are possible and could occur simultaneously in one reaction, to design a heterogeneous catalyst with superior reactivity and stability, it is important to identify the energy efficiency for different catalytic paths.

5.2 Method

An exemplary procedure for Suzuki reaction

4-bromobenzoic acid (64 mg, 0.32 mmol, 1 eq.) was dissolved in a mixture of 4 mL H₂O–EtOH (1: 1) and placed in a 10 mL vial. Phenylboronic acid (47 mg, 0.382 mmol, 1.2 eq.), potassium carbonate (133 mg, 0.96 mmol, 3 eq.) was then added to the solution. 0.5 % Pd/G was then added, the tube was sealed, stirred and heated at 80 °C for 10 min. After the reaction, the mixture was diluted with 10 mL of EtOH and test in GCMS/HPLC versus internal standard.

Co-reduction (CO) method for catalyst synthesis.

For the preparation of Pd on graphene catalyst, 200 mL of deionized water (18.2 MΩ·cm), 90 mg of graphene oxide, and 200 μL of palladium nitrate were mixed by ultrasonication at 300 W for 20 min. Then the mixture was stirred for 3 hours to allow Pd cation exchange with the acidic functional groups on the GO. Finally, 400 μL of hydrazine was slowly added under stirring and subsequently, the solution was irradiated for 2 min in a microwave oven (Emerson MW8119SB) at full power (1000 W), 2.45 GHz. Once the mixture was irradiated, the product was washed and dried overnight in a vacuum oven at 80 °C.

Strong electrostatic adsorption (SEA) method and hydrogen reduction (Pd/G SEA-H).

For the synthesis of palladium on graphene, a 225 ppm H_2PdCl_4 solution was first made by dissolving 125 mg of PdCl_2 in 0.333 L H_2O and 328.6 μL of 12 M HCl (5.6 molar excess). The solution pH was adjusted to $\text{pH}=3.25$ with NH_4OH and a 5 mL initial aliquot was taken for inductively coupled plasma optical emission spectroscopy (ICP-OES) analysis of Pd content. Next, 1 g of graphene oxide was added to the solution and shaken at 100 rpm on an orbital shaker for 1 hour to allow for electrostatic adsorption of PdCl_4^{2-} . After shaking for 1 hour, a second 5 mL aliquot was taken and 0.2 μm syringe filtered for ICP-OES. The solution was next vacuum filtered, dried in a tube furnace at 180 $^\circ\text{C}$ in the presence of H_2 flow.

Solventless microwave treatment of Pd/G SEA catalyst (Pd/G SEA-MW).

200 mg Pd/SEA catalyst placed in a 10 ml tube. The tube was then heated in a CEM microwave reactor at 135 $^\circ\text{C}$ for 10 minutes with magnetic stirring to produce the final Pd/G SEAM catalyst. The difference of Pd concentration between before and after microwave heated, measured by ICP-OES, was used to calculate the Pd wt% of the resulting Pd/G SEAM catalyst.

Kinetic evaluation of Suzuki reaction.

Bromobenzoic acid (50 mg, 0.25 mmol, 1 eq.) was dissolved in a mixture of 4 mL H_2O : EtOH (1: 1) and placed in a 10 mL vial. Phenylboronic acid (33 mg, 0.3 mmol, 1.2 eq.), potassium carbonate (103 mg, 0.75 mmol, 3 eq.) was then added to the solution. 0.5 % Pd catalyst, homogeneous or heterogeneous, was then added, the tube was sealed, stirred and heated in a water bath (at 25 $^\circ\text{C}$, 35 $^\circ\text{C}$, 55 $^\circ\text{C}$, 65 $^\circ\text{C}$ and 80 $^\circ\text{C}$ respectively). A small aliquot of the reaction mix tested by HPLC at reaction time 1, 3, 5, 10, 30 and 60 mins.

Transmission electron microscopy (TEM).

The particle size and particle size distribution of the Pd-based nanoparticles were investigated by transmission electron microscopy (TEM) with a Zeiss Libra 120 Plus at 120 kV. For the TEM grid preparation, a drop of the catalyst was diluted in 2 mL of acetone and sonicated for ~10 min. Then, a 300 mesh Cu /lacey-carbon grid was immersed twice in the diluted suspension and allowed to dry at room temperature. Image J 4.18v software was used to measure the particle size of the obtained pictures.

Calculation of activation energy.

The calculation is based on the conversion results at a different temperature from Kinetic evaluation as shown in Fig 5.1 which shows the conversion at different temperature in Suzuki reaction using 4-Bromo benzoic acid and phenylboronic acid catalyzed by solid supported Pd catalyst. The conversion was evaluated at 1, 3, 5, 10, 15, 30 and 60 mins.

The Activation energies were then calculated assuming the second order of reaction. The rate constant of a reaction can be expressed as

$$k = Ae^{-E_a/RT}$$

Transformed by taking log on both sides of the equation:

$$k = -E_a/R(1/T) + \ln A$$

$$E_a = \text{Slope (Arrhenius Plot)} * R$$

Where R is the constant equal to 8.314 J/mol-K.

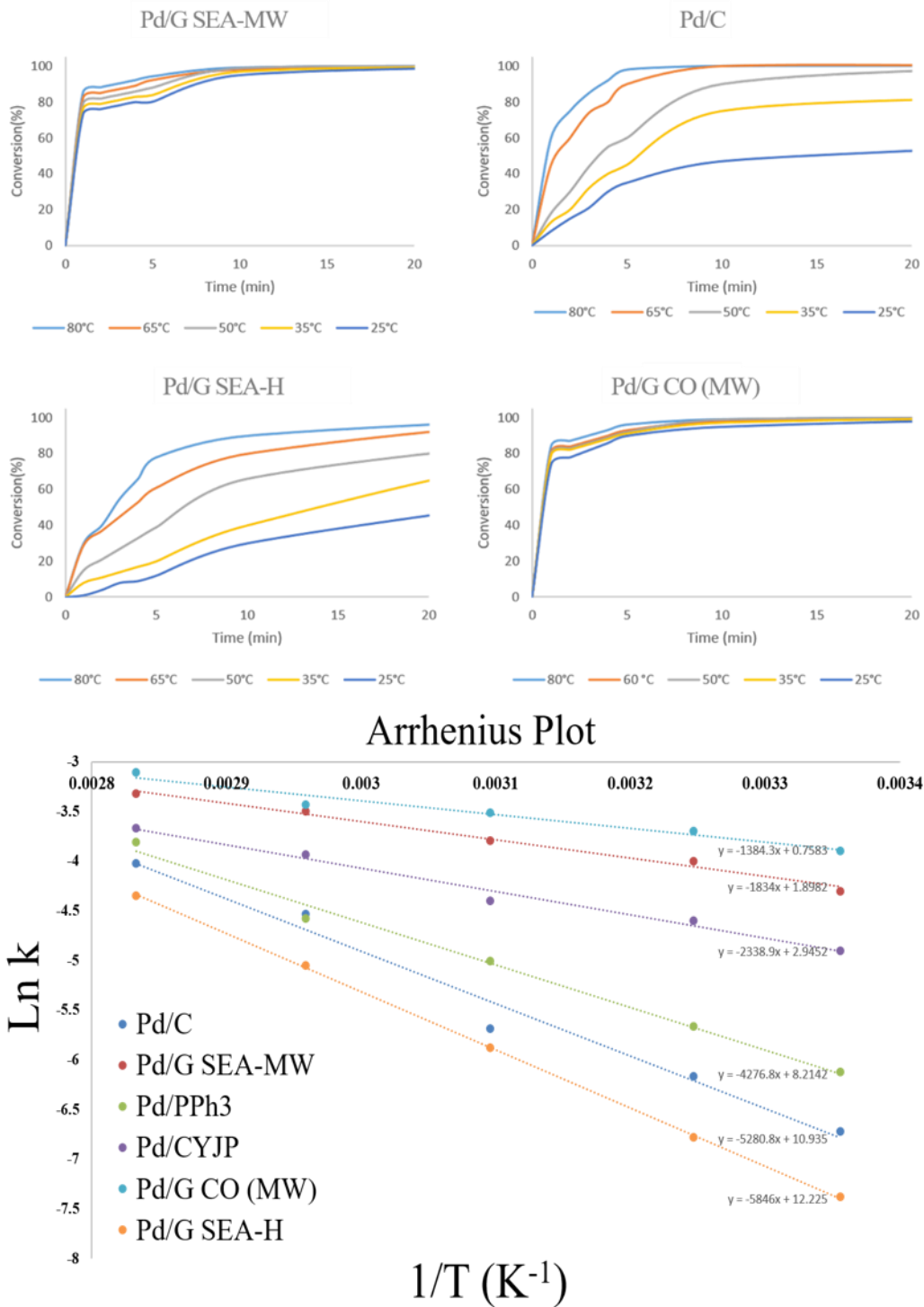


Figure 5-1 Pd based solid support catalyst conversion at different temperature in Suzuki reaction using 4-bromobenzoic acid and phenylboronic acid. Second order Arrhenius Plot based on the conversion at different temperatures

Resin preparation for three-phase tests

Rink amide resin (1.0 g) was added to a 30-ml cartridge with a 70 μm frit. Then 20 ml of dimethylformamide (DMF) were added to swell the resin for 30 min. Next, 4-Iodo-benzoic acid (1.04 g, 4.2 mmol), hydroxybenzotriazole (0.642 g, 4.2 mmol) and diisopropylcarbodiimide (0.529 g, 4.2 mmol) were premixed in dichloromethane (DCM) (20 ml) and then added to the resin. The cartridge was capped and stirred for 6 hours. Subsequently, the solvent was removed and the resin was washed three times with DMF (15 ml), DCM (15 ml) and methanol (15 ml) for 2 min each. Finally, the resin was dried in vacuum for 24 hours at 0 $^{\circ}\text{C}$.

Three phase tests

100 mg 4-Iodo-benzamide bound rink amide resin (0.07 mmol 4-Iodo-benzamide) were added to 5 ml DMF to swell for 30 min in a 10 ml cartridge with a 70 μm frit. Then the pre-swelled resin, Phenylboronic acid (24.5 mg, 0.22 mmol), potassium carbonate (55.2 mg, 0.4 mmol) and Pd/G catalyst 30% were added to 2 ml ethanol and water (1:1) solution. The cartridge was capped and stirred for 20 hours at 25 $^{\circ}\text{C}$. The resin was then washed with ethanol. Afterward, trifluoroacetic acid (0.95 ml) and deionized water (0.05 ml) were added to the resin and the cartridge was capped and stirred for 4 hours. Finally, the solution was collected and washed again. The three-phase test was also performed at 80 $^{\circ}\text{C}$ using microwave irradiation.

Hot filtration test and ICP-MS analyze.

Bromobenzene (50 mg, 0.32 mmol, 1 eq.) was dissolved in a mixture of 4 mL water-ethanol (1:1) and placed in a 10 mL microwave tube. Phenylboronic acid (47 mg, 0.382 mmol, 1.2 eq.), potassium carbonate (133 mg, 0.96 mmol, 3 eq.) was then added to the solution. Next 0.5 wt.% of Pd/G catalyst was added to the tube then sealed, stirred and heated at 80 $^{\circ}\text{C}$ for 10 min under

microwave irradiation (250 W, 2.45 GHz). After, the reaction mixture was hotly filtrated through celite. A portion of the filtrated solution was then analyzed by ICP-MS for Pd content. To fully digest the metal nanoparticles, the filtrated solution was diluted in 10 wt % nitric acid aqueous solution. Then the solution was tested by ICP-MS (Varian 820 ICP MS) with Pd standards to determine the Pd content. In addition, fresh bromobenzene (50 mg, 0.32 mmol, 1 eq.) and phenylboronic acid (47 mg, 0.382 mmol, 1.2 eq.) was added to the filtrated solution. This latter solution was also subjected to 80 °C for 10 min under microwave irradiation (250 W, 2.45 GHz) to indirectly check for any leached active Pd species.

5.3 Result and discussion

5.3.1 Synthesis Pd on graphene via different methods

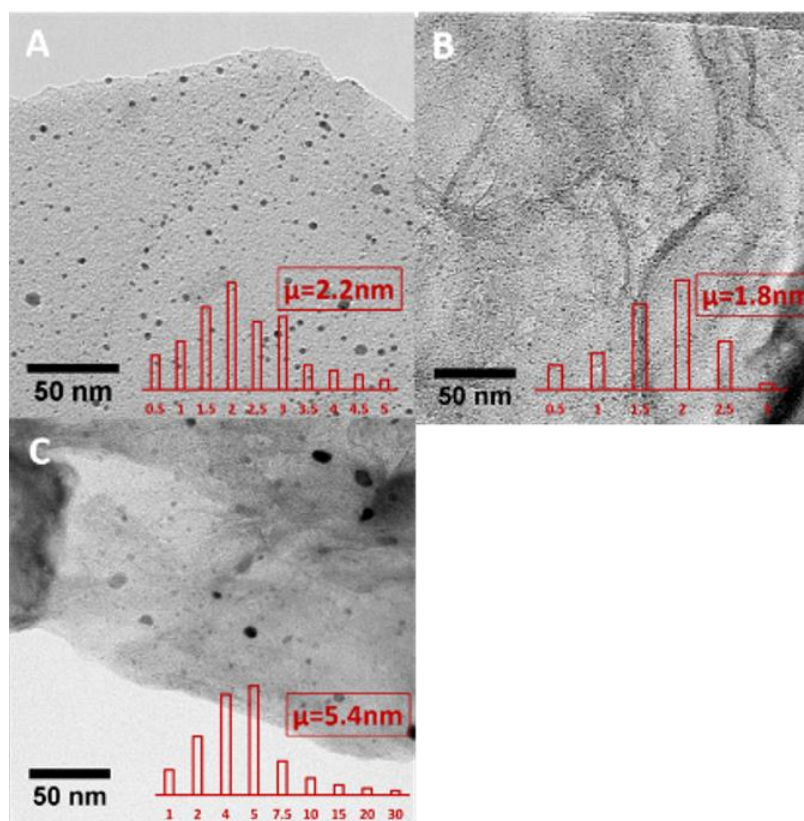


Figure 5-2 TEM image and particle size distribution of Pd/graphene catalyst fabricated by (A) co-reduction method, (B) SEA method and (C) Post solventless microwave heating method (SEA-MW).

To understand the impact of particle size and the nature of support substrate on the catalytic reactivity, Pd/graphene catalysts were fabricated in three different methods including co-reduction (CO), strong electrostatic adsorption (SEA)(178-180) and post dry phase microwave method (SEA-MW). The co-reduction method aims to reduce the Pd precursor and the graphene support at the same time using a strong reducing agent and microwave irradiation. The hypothesis behind the SEA approach to catalyst synthesis is that monolayer adsorption of metal complexes via strong electrostatic adsorption can lead to small metal particles when the complexes are reduced by reducing agent. The maximum uptake of the metal salt highly depends on the PH of the solution. For the SEA-MW approach, the reducing agent in the regular SEA reduction process is replaced by microwave irradiation. And recent studies show the microwave heating is an efficient method to reduce GO back to pristine graphene (116, 181).

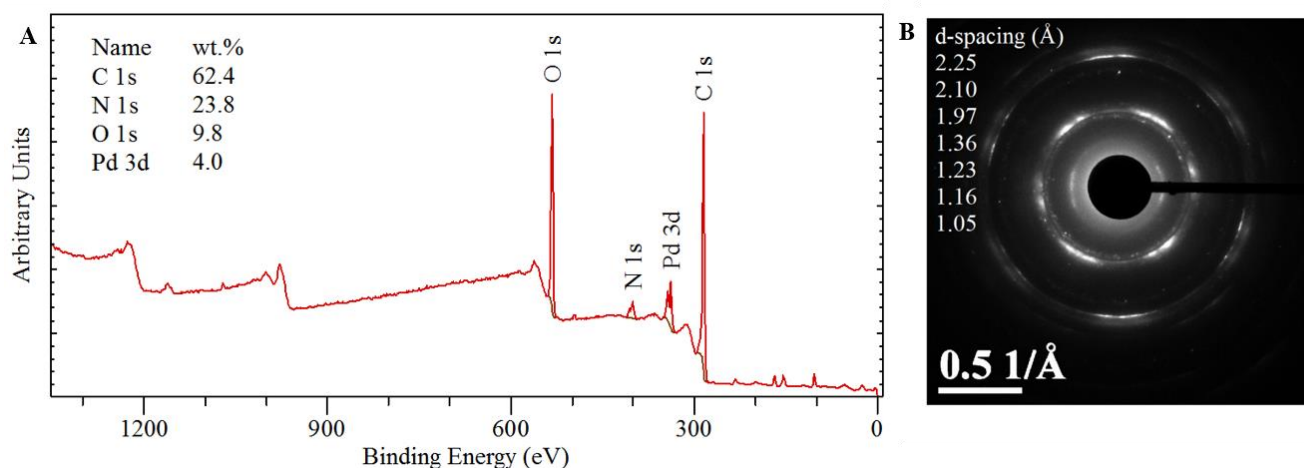


Figure 5-3 (A) atomic survey on the surface of Pd/G catalyst measured by x-ray photoelectron spectroscopy. (B) SAED shows the crystalline structure of Pd. SAED was performed in an area of about 100 nm². The right side of Fig. 4a shows the SAED pattern and the measured d-spacing

values. From the diffraction pattern, three of the rings at a d-spacing of 2.10 Å, 1.23 Å, and 1.05 Å are associated with the graphene substrate exhibiting the characteristic sixfold rotational symmetry. The other diffraction rings are identified and their d-spacing of 2.25 Å, 1.97 Å, 1.36 Å, and 1.16 Å correspond to the (111), (200), (220), and (311) planes of the face center cubic crystalline structure of Pd.

Fig 5.2 (A) shows the Pd graphene catalyst fabricated by CO method using hydrazine and microwave heating. Previous studies suggested that Pd clusters (up to 5nm) bind strongly to the vacancies/voids defect in the graphene lattice generated by the reduction of graphene oxide using the microwave heat. As a result, the embedded Pd nanoparticles hardly leached from the support substrate and the reaction proceeds on the surface of the deposited particles. Note that the size of the Pd/graphene prepared by the CO method is smaller than the previously reported (61). Strong electrostatic adsorption (SEA) method, using hydrogen and conventional heating as reducing agent, also enables deposition of Pd cluster (avg. 1.9nm) on the graphene substrate, showed in Fig 5.2 (B). Since the Pd nanoparticles are immobilized by strong electrostatic force between the metal and different functional groups (epoxy, hydroxyl, and carboxylic acid) on the surface of graphene, no significant vacancy defects on the graphene are formed by this method. A dry phase microwave heating reduction of the Pd nanoparticle after strong electrostatic adsorption (SEA-MW) is used to testify if the defect site on the graphene created by microwave heating is a key feature to inhibit metal leaching and boost catalyst reactivity as shown in Fig 5.2 (C). The atomic survey on the surface of Pd/G catalyst measured by x-ray photoelectron spectroscopy and SAED shows the crystalline structure of Pd are also shown in Fig 5.3. It is interesting to note that isolated vacancy defect site on the graphene sheet, vacancy site that accommodating Pd nanoparticles, as well as Pd nanoparticle embedded in the graphene was able to be observed by TEM due to the larger particle

size generated by solventless microwave heating as shown in Fig 5.4. SEM image of Pd on activated carbon is shown in Fig 5.5.

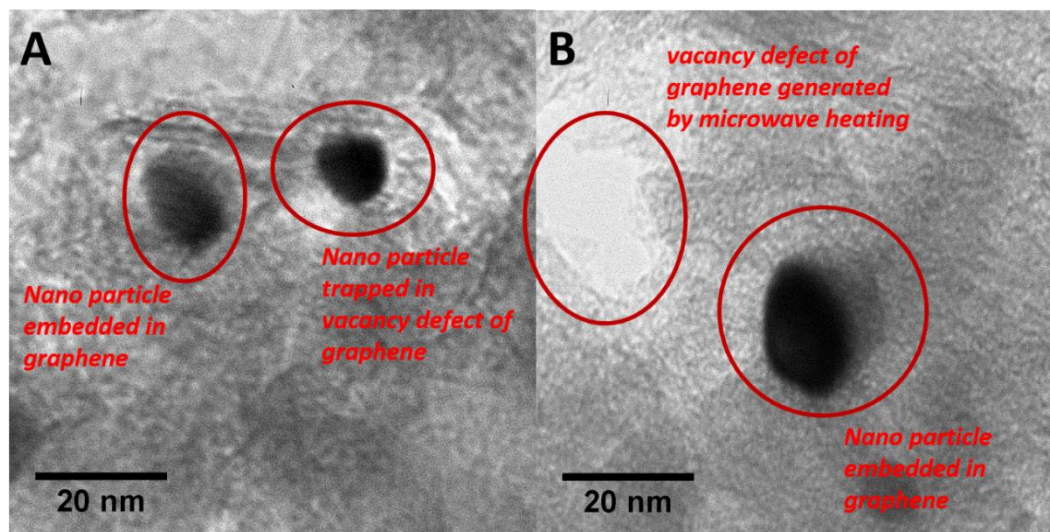


Figure 5-4 TEM images show isolated vacancy defect site on the graphene sheet, vacancy site that accommodating Pd nanoparticles, as well as Pd nanoparticle embedded in the graphene. Catalyst generated via solventless microwave method.

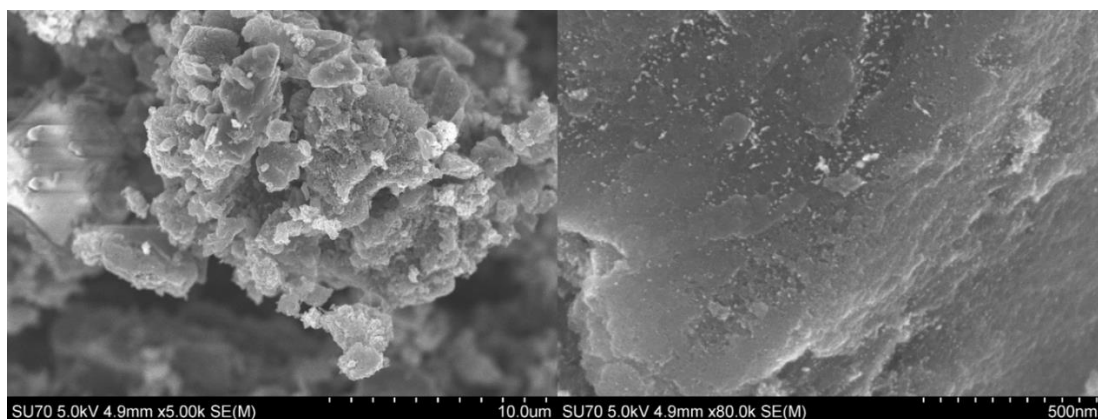


Figure 5-5 SEM images of commercially available Pd on activated carbon.

5.3.2 Kinetic evaluation and turn over frequency test

The resulting catalysts were then evaluated with respect to commercially available heterogeneous and homogenous Pd-based catalysts for activation energy and TOF in a model

Suzuki reaction using 4-bromobenzoic acid and phenylboronic acid as a reagent. The reaction conversions at each sampling time point are shown in Fig 5.1. The Pd/G catalyst fabricated by CO method represents remarkably high TOF and low activation energy compared with all another catalyst. In order to make the comparison more meaningful, the Pd/G CO and Pd/G SEA were designed to possess similar size distribution (avg. 2 nm) of Pd nanoparticles. However, the activation energy (0.12 eV) of the Pd/G CO is about one-fourth of activation energy (0.5 eV) of the catalyst fabricated via SEA method. The significant variation of the activation energy of those two catalysts with similar particle size and support substrate suggests that the catalytic reactivity is sensitive to how the metal clusters interact with support. In the case of Pd/G SEA method, the Pd nanoparticles are attached to the graphene via the oxygen-based functional group. And the binding energy of Pd cluster to the oxygen decorated graphene is significantly lower than the binding energy of Pd clusters bound to the vacancy defect site on the graphene. The suspected reason why the Pd/G SEA has lower catalytic activity is the supported Pd clusters are leached out from the graphene or the functional groups on the graphene obstructs charge flow between the substrate and Pd cluster. As a result no significant benefit from graphene support was observed by using SEA method. In fact, the activation energy of the Pd/G SEA catalyst is close to the activation energy of commercially available Pd/C catalyst which, based on several previous studies, is believed to catalyze the reaction under a “homogenous” mechanism. However, instead of using hydrogen and tube furnace heating as in traditional SEA method, catalyst (Pd/G SEA-MW) reduced by solventless microwave heating (no reducing agent) after strong electrostatic adsorption result in much robust catalyst even when the heating generated larger nanoparticles (up to 20 nm) and extended size distribution. It is generally considered that the large nanoparticles are less catalytic reactive than smaller nanoparticle since the specific surface area of large nanoparticle is lower.

However, the activation energy of Pd/G SEA-MW containing significantly larger Pd nanoparticles is only one third of the activation energy of Pd/G SEA. This indicates the microwave irradiation generates interaction between the Pd nanoparticle and the support substrate which boosts the Pd nanoparticle activity. The reason that activation energy of Pd/G SEA-MW is slightly lower than the Pd/G CO catalyst is mainly due to the dry phase microwave heating that destroyed some lower coordination Pd protrude sites, (adjacent Pd less than 4) as describe in the theoretical portion. The catalytic reactivity of commercially available Pd/C is measured as a benchmark for heterogeneous catalyst. The activation energy and turnover frequency is 0.45 eV and 12,000 h⁻¹, respectively. After comparing the Pd/graphene catalysts fabricated by three different methods, the microwave heating which generate the vacancy/void defect sites to accommodating the Pd nanoparticle is the most critical feature that decrease the activation energy.

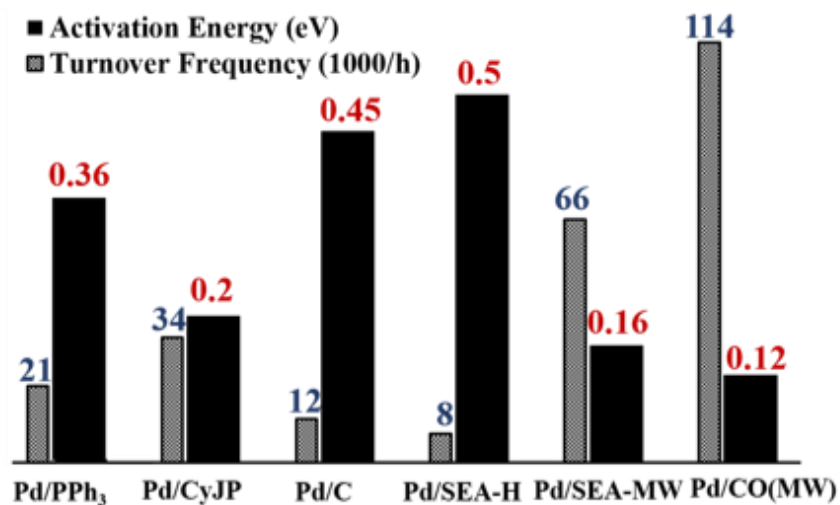


Figure 5-6 Activation energy and TOF of the catalysts in Suzuki reaction.

Suzuki Reaction						
Catalyst	Pd(OAc) ₂ PPh ₃	Pd(OAc) ₂ CyJohnPhos	Pd/C	Pd/G SEA-H	Pd/G CO	Pd/G SEA-MW
Activation energy (KJ/mol)	35.5	19.6	43.9	48.6	11.6	16.0
Activation energy (eV)	0.36	0.21	0.45	0.5	0.12	0.17
TOF mol of catalyst (h ⁻¹)	21,000	34,000	12,000	8,000	114,000	66,000

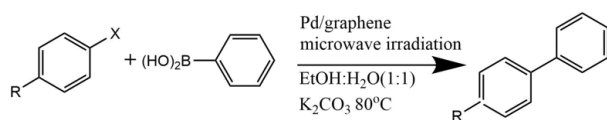
Table 5.1 Activation energy and TOF of the catalysts in Suzuki reaction.

The measured activation energy of the two homogenous catalysts, Pd/triphenylphosphine (Pd/PPh₃) and Pd/(2-Biphenyl)dicyclohexylphosphine (CyJohnPhos) (Pd/CYJP), are 0.36 eV and 0.21 eV, respectively. The bulky and electron rich CyJohnPhos Ligand enhances the Pd catalytic activity especially at low temperatures which is consistent with previous studies. The remarkable improvement of CyJohnPhos ligand compared with PPh₃ is thought to be due to the bulky structure that sterically pushes the two aryl groups closer, which facilitates the reductive elimination step. Although the CyJohnPhos ligand has excellent performance in assisting the Suzuki reaction, the activation energy of Pd/G CO catalyst is about half of the activation energy of Pd(OAc)₂/CyJohnPhos homogenous catalysis and the TOF is one order of magnitude higher. Furthermore, the lower activation energy is not only indicating fast reaction rates but also potential to activate more energetically and structural hindered substrates like aryl chloride.

5.3.3 Heterogeneity test

The previous combined computational and experimental studies demonstrate that the reduced graphene strongly binds the palladium clusters, and enhances the reactivity suggesting that the supported clusters are the favored species in the cross-coupling reaction. This catalyst was then

tested in a series of experiments to evaluate if the catalyst is functionalized by leach soluble Pd atoms or small clusters or as a true heterogeneous method. The hypothesis of the three-phase test is by immobilizing one of the reagents onto an insoluble surface (usually a polymer) to generate a second solid phase reaction (182). Since reaction merely occurred in a solution between two substrates both in the insoluble phase, the reaction would not proceed if the metal nanoparticle catalyst is strongly bound to the graphene. In opposite, if the metal nanoparticle in the solid supported catalyst is leached out the graphene support and catalyze the reaction in solution phase, with the polymer-supported reagent, the reaction can still proceed (44, 63, 183, 184). The control experiments using the unbounded corresponding aryl-halide as reagent provides evidence that the graphene supported Pd nanoparticle is extremely active in catalyzing the crossing coupling reaction.

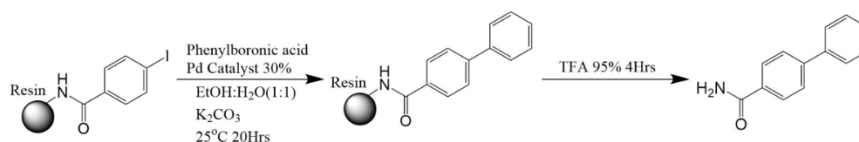


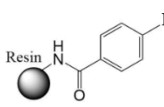
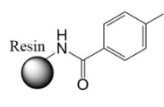
Entry	Aryl Halide	Conversion ^a
1		100%
2		100%
3 ^{b,c}		100%
4		100%
5		100%
6 ^{b,c}		100%

a, Conversion confirmed by GCMS and HPLC. *b*, Similar conversion could be achieved by using Pd(OAc)₂/PPh₃ Catalyst. *c*, Similar conversion could be achieved by running reaction in 25 °C in 1 hour.

Table 5.2 Control experiments Suzuki reaction

In the three-phase experiment, 4-iodobenzoic acid and 4-bromo-benzoic acid were covalently immobilized on an insoluble resin substrate as the aryl halide partner of Suzuki reaction, so the cross-coupling will only occur if the palladium catalyst is released into the solution. To ensure the solid support catalyst Pd/G is active in the reaction condition of the three-phase test, control experiments were conducted, as shown in table 5.2. Rink amide resin substrate bound to 4-iodobenzoic acid/4-bromobenzoic acid and phenylboronic acid (in solution) were then used in a Suzuki reaction as shown in Table 5.3. In the presence of homogeneous catalyst Pd(OAc)₂ and ligand, 60% of conversion is observed after cleavage from the substrate resin. However, Pd/graphene (Pd/G) catalyst, in the same reaction condition, resulted in less than 1% conversion. This insignificant amount of conversion confirms that unbounded palladium plays a negligible role in the overall catalytic process and is not the major source of catalytic activity. Furthermore, by adding a fresh homogeneous catalyst to the inactive Pd/G batch, after 20 hours, the same conversion is achieved as compared with only using a homogeneous catalyst. This test offers strong evidence that Pd nanoparticles are not leaching into the free solution and the reaction is primarily occurring on the surface of small Pd nanoparticles supported on reduced graphene. However, this test does not preclude Pd leaching promoted after the binding of the aryl-halides and Pd clusters while immobilizing the aryl-halides to an insoluble substrate.



Resin bounded aryl halide	Pd Catalyst	Reaction temperature	Running time (Hour)	Conversion
	Pd/graphene	80°C ^a	2	<1%
	Pd(OAc) ₂ /PPh ₃	80°C ^a	2	29% ^b
	Pd/graphene	25°C	20	<1%
	Pd(OAc) ₂ /PPh ₃	25°C	20	45%
	Pd/graphene	80°C ^a	2	<1%
	Pd(OAc) ₂ /PPh ₃	80°C ^a	2	33%
	Pd/graphene	25°C	20	<1%
	Pd(OAc) ₂ /PPh ₃	25°C	20	60%

a, Reaction was heated using microwave irradiation. *b*, Conversion achieved 26% after 30mins.

Table 5.3 Different reaction condition for the three-phase test.

To further demonstrate the catalytic mechanism, a hot filtration test followed by ICP-MS analysis was implemented. Hot filtration test is another standard protocol to test if the leached metal plays an important role in the catalysis process. In this test, the reaction is terminated near the middle point of the total conversion. The solution of the half-completed reaction is then filtrated to remove any insoluble materials. The filtrate then continues to react to determine if there is any new product formed after the removal of the solid supported catalyst. Any product generated after the filtration only accounts for the leached metal in the solution.

A Suzuki reaction of 4-bromobenzene and phenylboronic acid was performed in the presence of Pd/G catalyst as showed in Fig. 5.7. To evaluate any sign of leached palladium, hot filtration using celite was implemented after the coupling reaction was completed. The filtrate solution was analyzed using ICP-MS and it was shown to contain approximately 225 ppb of palladium. Fresh reagents were then added to the filtrate solution and no catalytic activity was observed. While the

presence of Pd in solution suggests that the catalyst is not completely heterogeneous, the lack of activity after removal of the solid supported Pd catalysts indicates that the reactivity is not derived from the dissolved species.

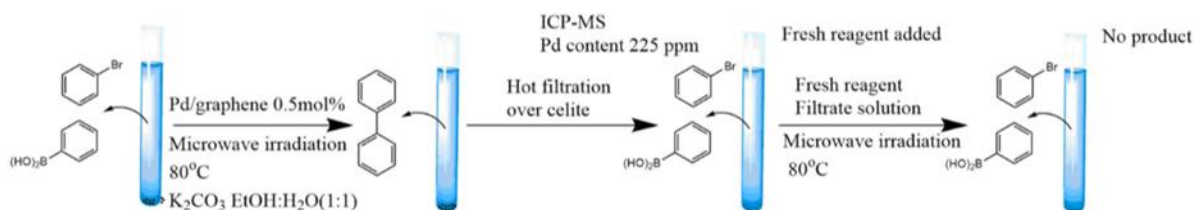


Figure 5-7 Hot filtration test of Pd on graphene catalyst

Although we cannot definitively preclude the possibility of a rapid leaching and re-deposition mechanism, the consistency between the results from these two orthogonal experiments along with our computational analysis of the Pd binding energy within graphene defect sites strongly suggests that most of the catalytic activity arises from the supported Pd species during the Suzuki reaction. Furthermore, we have found no evidence that would support a homogeneous catalytic pathway with Pd/G for Suzuki reactions within this body of work. However, we also recognize the importance of the fabrication method for preparation of the Pd/G catalysts. Sufficiently small Pd clusters must be produced to properly accommodate defect sites that promote cluster immobilization and minimize metal leaching during the carbon-carbon cross-coupling reaction. One may also expect that large Pd clusters produced during the deposition process may increase the likelihood of leaching. However, it is clear that these larger clusters are not the source of remarkable catalytic activity reported herein.

5.3.4 Recyclability test

One of the major advantages of the heterogeneous catalyst is the recyclability of the catalyst. The catalyst can be removed and retained from the reaction mixture by a simple filtration or

centrifugation step. The recyclability tests were carried out to determine how many time the catalyst can be collected from the reaction mixture and reused before losing any catalytic reactivity.

A recyclability test was performed on a Suzuki reaction between 4-bromotoluene (0.5 mmol) and phenylboronic acid (0.6 mmol) with 0.5 mol% of Pd/G catalysts, potassium carbonate (1.5 mmol), and at 80°C with stirring. Following each reaction, the 25 mL of EtOH was added and the entire mixture was centrifuged and the supernatant was decanted. This centrifuge wash procedure was repeated three times. After the final wash, new reaction reagents were added and the subsequent reactions were performed until conversion by GCMS dropped.

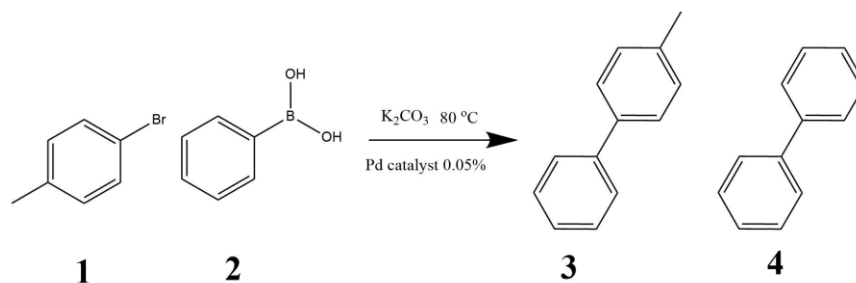


Figure 5-8 The model Suzuki reaction tested in the recyclability test

Cycle of reaction	Pd/SEA-H		Pd/SEA-MW		Pd/CO(MW)	
	Conversion* of 1	Conversion to 3**	Conversion of 1	Conversion to 3	Conversion of 1	Conversion to 3
1	100	92	100	89	100	92
2	100	92	100	93	100	95
3	96	96	100	93	100	92
4	89	89	100	98	100	98
5	44	44	100	98	100	98
6	29	29	93	89	100	99

7	-	-	90	88	100	99
8	-	-	53	52	100	99
9	-	-	-	-	100	99
10	-	-	-	-	58	58

* All conversions were determined by GC/MS

** The competing reaction is the homo-coupling of the phenylboronic reagent resulting in byproduct 4 and reduction of the Pd⁺² to Pd⁰.

Tab. 5.4 The GC/MS conversion of the recyclability tests

The results from the recyclability test show the Pd/G catalyst manufactured by the CO(MW) method has the highest number of reaction cycles. Meanwhile, the catalyst generated without the microwave heating exhibits the lowest recyclability which the conversion started to drop after the third cycle and the conversion was cut in half after the fourth run. The result is consistent with the theoretical calculation. Since the reduction method by hydrogen in conventional heating tube furnace is not able to generate any vacancy defects, the metal nanoparticles bind to the graphene surface only through the oxygen-based functional group on the graphene. As shown in the theoretical result from chapter two, the binding energy of Pd cluster binding to graphene through the vacancy defect is much higher than the binding through the oxygen functional groups which result in stabilized Pd nanoparticles and better recyclability.

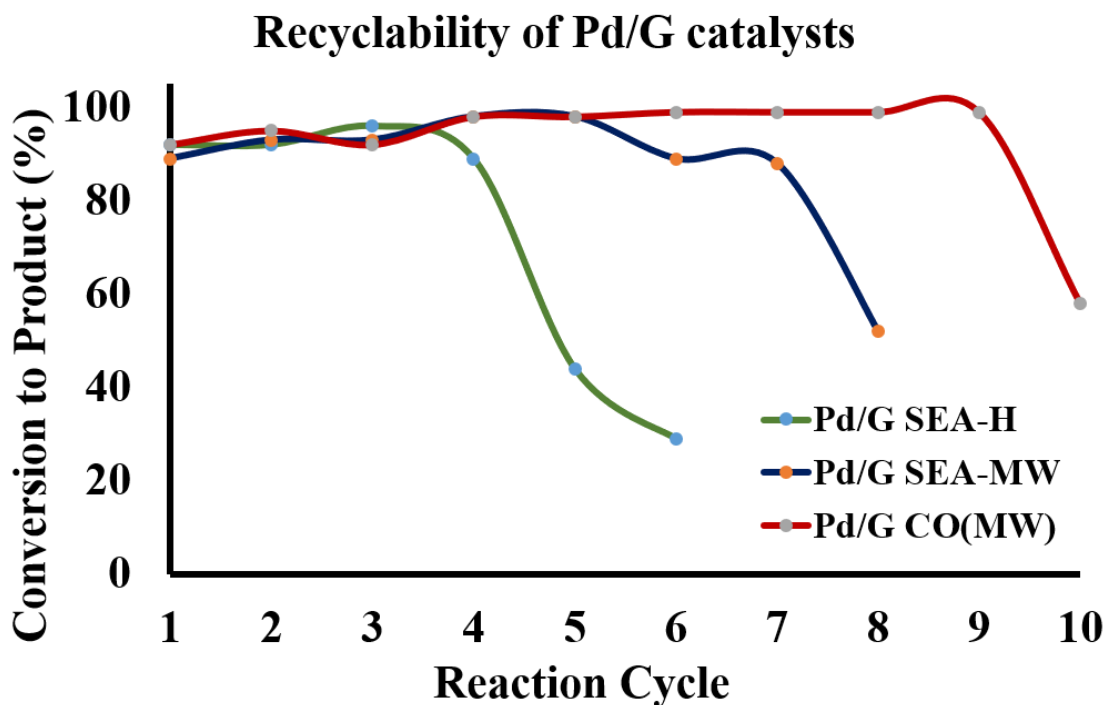


Figure 5-9 Recyclability of three Pd on graphene catalyst prepared by the different method.

5.4 Conclusion

Ultra-fine Pd nanoparticle supported on graphene catalyst was successfully prepared using a different method. The average size of the Pd nanoparticle ranged from 1 to 2 nm was achieved. However, catalyst only reduced by microwave irradiation exhibits extraordinary reactivity. The kinetic studies of the activation energy of a variety of homogeneous and heterogeneous Pd catalyst provide insights that defect-inducing microwave irradiation drastically lowers the activation energy. The heterogeneity test provides fundamental evidence that the catalysts prepared by microwave irradiation catalyze the reaction via the true heterogeneous manner.

Chapter VI Ni-Pd @ Graphene-nanotube hybrids as robust catalysts in cross-coupling reactions

6.1 Introduction

The increasing demand for both efficient and environmentally benign process stimulates the development of heterogeneous catalysis in the fine chemical, energy and pharmaceutical industry. Many disadvantages of homogeneous catalysts can be overcome via homogenization the catalyst such as the separation, recovery, and reuse of the catalyst. A catalyst support is usually required for the heterogeneous catalyst fabrication since the support substrate play an important role in the stabilizing the metal particle as well as the dilution of the expensive catalyst component. Graphene as a two-dimensional atomic thin carbon allotrope has been extensively exploited as supporting substrate for heterogeneous catalyst in organic synthesis due to its high specific area, high conductivity and excellent thermal and chemical stability. Recent researchers suggested the graphene support actively assisting the charge transfer between the supported metal particles and the adsorbed molecules in many arylations, hydrogenation and oxidation reactions due to the conducting nature of the sp^2 carbon hybridization. However, major drawbacks such as the agglomeration of the graphene sheet due its restacking nature are still limiting the application of graphene as support substrate which leads to loss of surface area, poor reusability of the catalyst and reproducibility of the reaction.

Several approaches have been made to address the restacking issue of graphene. One intriguing approach is to integrate the one-dimensional carbon nanotube and the two-dimensional graphene into a three-dimensional (3D) composite (GCNT) to combine the advantages of the high surface area provided by the atomic thin sheet of graphene and the high aspect ratio of the carbon nanotube.

Additionally, experimental results also suggest the hybrids GCNT possess enhanced electrical property, reduced sheet resistance, modified mechanic and thermal property, and superior electrochemical stability if the carbon nanotubes were seamlessly attached to the graphene lattice. Previously, the production of carbon nanotube and graphene usually relies on chemical vapor deposition (CVD) method. Some of this process is economical-inefficient, time-consuming, the reactions are always in separated phases which require especially equipment. A facile, low-cost, rapid and easy to scale up a method to incorporate the graphene and carbon nanotube is still desired.

A ball milling technique is mainly used to mechanically exfoliate graphite and functionalize graphene by adding impurities to the edge of the lattice. The reported BET surface area of exfoliated graphene prepared by the ball milling method is 150-350 m²/g. To the functionalize the graphene, with the kinetic energy provided by the moving ball, the strong interaction between graphene lattices were broken and the new surface generated is chemically active. The previous experimental result indicates many N, O, S based impurities and even metal nanoparticles can be immobilized to graphene through the ball milling method.

We developed a facile, solvent-less, scalable and rapid method to prepare a magnetic Pd nanoparticle-decorated graphene nanoplates-carbon nanotube-Ni composite (Pd@GCNTNi) as a highly active solid support catalyst for Suzuki reaction and C-H activation reaction. An urchin like the structure of the graphene nanoplates-carbon nanotube-Ni (GCNTNi) support was obtained through the ball milling the graphene nanoplates and Ni precursor follows by a solvent-less microwave irradiation treatment. Pd nanoparticles then were immobilized on the 3-D GCNTNi support through multiple methods including further ball milling treatment and microwave assisted chemical reduction.

6.2 Experimental method

5-20 wt% Ni(acac)₂ as the precursors of Ni nanoparticle is mix with graphene nanoplates, which is mechanically exfoliated from graphite. The market price of graphene nanoplates is at least an order of magnitude less expensive than the graphene oxide, reduced graphene oxide, and pristine graphene. The mixture of Ni(acac)₂ and graphene nanoplates is then transferred to a vessel in the ball mill to continue milling for 50 minutes. The mixture after ball milling is directly transferred to the CEM microwave reactor at different temperature for 10 to 50 minutes. Comparison experiments using domestic microwave was also conducted. The resulting materials were then tested by SEM to measure the size of the carbon nanotube that grown on the graphene lattice.

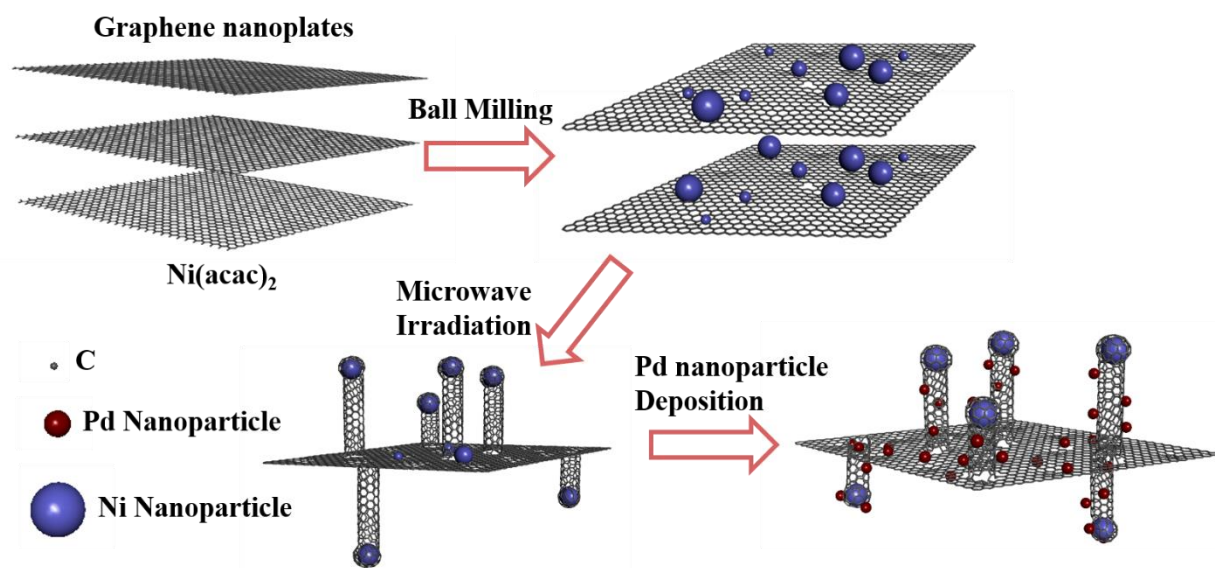


Figure 6-1 The strategy of the synthesis of the CNT/GNP hybrid and immobilizing the Pd nanoparticles on the 3-D CNT/GNP substrate.

6.3 Result and discussion

6.3.1 Synthesis the CNT/GNP support substrate

Ni with delicately designed ligands is known to catalyze a variety of cross-coupling reactions. Ni is also one of the important metal that used to produce graphene and carbon nanotube in several

chemical vapor deposition (CVD) processes. By combining the ball-milling and solventless microwave technology, we discovered a facile method to synthesize a three-dimensional nanostructure containing the hybrid of graphene-carbon nanotube-nickel nanoparticle (G-CNT-Ni) via a tip growth mechanism of the nanotube on graphene lattice without an additional carbon source as shown in Fig 6.1. Due to the re-stacking nature of the 2-D graphene lattice, experimental results on graphene used as battery material show poor reversible capacity and poor cycle life because of structural limits (185-188). The 3-D graphene-carbon nanotube hybrid could be a solution for the structural limitation of graphene which has great potential in the energy storage applications.

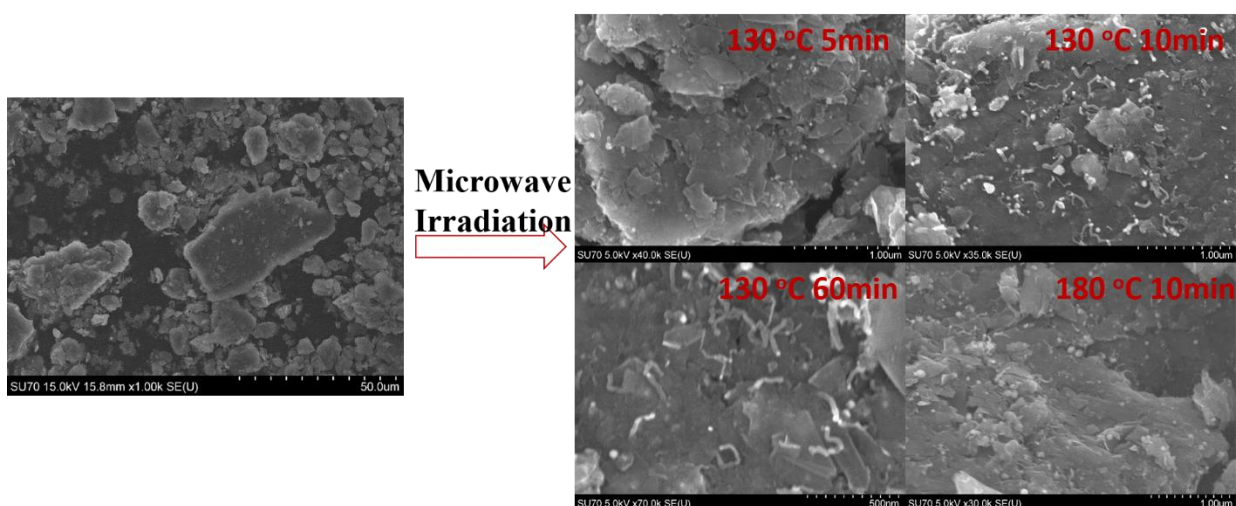


Figure 6-2 Left figure shows the Ni-graphene mixture after ball milling. Right figures show the growth of carbon nanotube on the graphene under microwave irradiation.

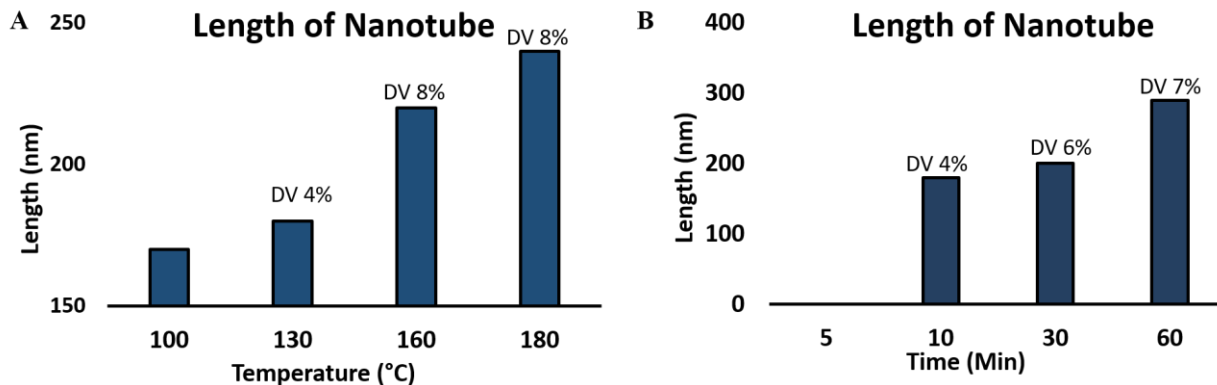


Figure 6-3 Fig (A) shows the length of the carbon nanotube as a function of and temperature after 10 mins of the microwave irradiation. Fig (B) shows the length of the carbon nanotube as a function of time after the microwave irradiation at 130 °C.

Previous studies on the effect of ball milling to form the metal nanoparticle on the graphene suggest small Ni nanoparticle can be formed through the ball milling process. XRD result of the Ni@GNP after ball milling also suggested small Ni nanocrystal around 3-4 nm was formed. During the microwave heating, the unreduced Ni precursors and small reduced Ni nanoparticles started to be reduced by the microwave heating and agglomerate. Defect sites on the graphene are the anchor points to immobilize the Ni nanoparticles. The suspected mechanism of the growth of the carbon nanotube started with the tremendous heat generated by the microwave through a “tip-growth” mechanism. Results from fig 6.2 clearly suggest that the length of the carbon nanotube is controlled by the heating temperature and time during the microwave irradiation. Null formation of carbon nanotube was observed when the heating temperature is below 100 °C. We then use a domestic microwave as a comparison to drastically illustrate the effect of microwave irradiation since the domestic microwave (Emerson MW8119SB at full power 1000 W, 2.45 GHz) has a much higher fixed power comparing to the CEM reactor. The resulting G-CNT-Ni hybrids are shown in fig. 6.3. Both the size and population of the carbon nanotube increased significantly in contrast to

previous CEM heating. 3D structure from hundreds of nanometers to several micrometers observed from the SEM images.

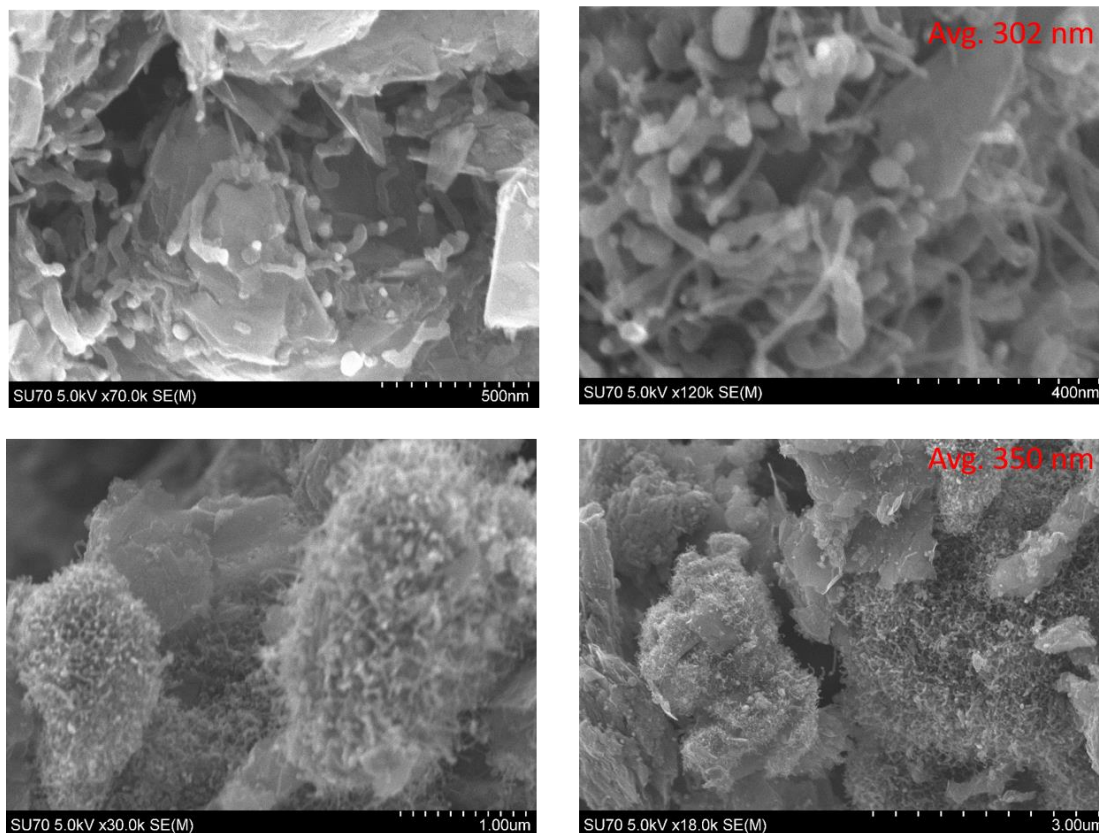


Figure 6-4 Graphene-carbon nanotube-Ni nanostructure generated using ball milling and domestic microwave.

It is important to note that no carbon nanotube is generated when the Ni is supported on activated carbon for the small process which is indicated that graphene is the only source of carbon to grow nanotube. A critical temperature is also required to induce the carbon nanotube. One control experiment is conducted using a water bath to control the reaction temperature during the domestic microwave heating. As a result, the temperature of the vial is not able to exceed 100°C and no carbon nanotube is formed in the control experiment. And since, the Ni nanoparticles are

coated with carbon, the G-CNT-Ni nanostructure, without further treatment, shows no catalytic reactivity for Suzuki cross-coupling reaction.

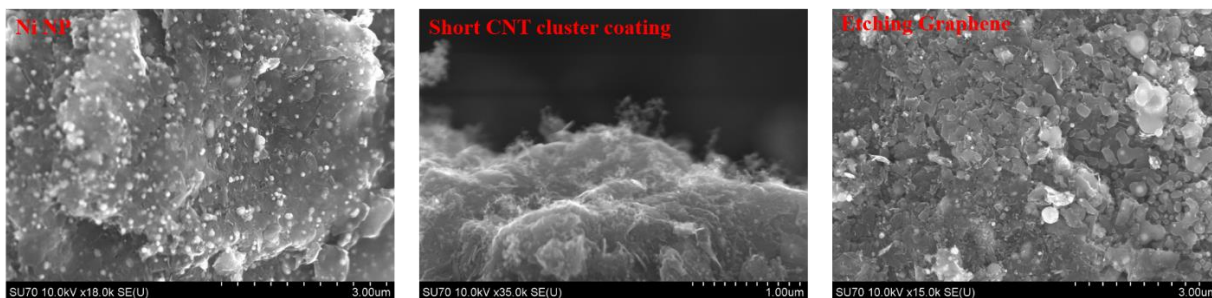


Figure 6-5 Ni@GNP generated using ball milling and domestic microwave.

Other interesting effects were also observed by SEM after the Ni@GNP sample was treated by microwave irradiation. At parts of the microwave treated Ni@GNP sample, large naked Ni nanoparticle without any coated carbon nanotubes was observed as shown in Fig 6.4(left). The existing of uncoated Ni nanoparticle was thought to result from the uneven heating generated by the domestic microwave oven. Parts of the sample did not gain enough energy to grow the nanotube. However, Ni nanoparticle stuck in uneven carbon holders was observed which is important evidence of the commencement of the growth of the carbon nanotube and provides information on how the growth proceeds. As shown in fig 6.4 (middle), in the same Ni@GNP sample, parts of the GNP were covered with small carbon nanotube clusters. However, no metal tip was observed in those small carbon nanotubes. The exact reason for the formation of such coating is still unknown. On the right side of fig 6.4 shows small graphene flake with etched edges. Since the carbon source of the carbon nanotube was thought to directly come from the graphene nanoplates, the reason of the formation of the small graphene flake is suspected to result from the consumption of the graphene and the detachment of the carbon nanotube.

The BET surface area study is an important technique to determine the overall modification to the Ni@GNP due to the microwave irradiation. As shown in table 6.1, the surface area of the Ni@GNP after ball milling (Ni@GNP BM) was 144 m²/g. After one minute of microwave irradiation, the surfaces increased to more than two times to 319 m²/g. The continuing microwave heating has no significant impact on the BET surface area of the sample. However, the micropore area of the sample was increased after the second minute of microwave heating. To determine the surface increasing was due to the growth of the carbon nanotube or the thermal exfoliation of the graphene nanoplates, we carried out a control experiment which GNP was ball milled without the presence of the Ni salt. The BET surface of the sample (GNP BM) was determined to be 258 m²/g. Then the ball milled GNP sample was microwaved in the same condition as the Ni@GNP batch. The surface area of the new sample (GNP BM-KMW2MIN) was 266 m²/g. The surface area increase of the sample without Ni was negligible and within the standard error of the physisorption equipment. The control experiments confirmed the surface area increase of the Ni@GNP sample was due to the growth of the carbon nanotube.

Sample	BET surface (m²/g)	Micropore (m²/g)
Ni@GNP BM	144	50
Ni@GNP BM-KMW1MIN	319	92
Ni@GNP BM-KMW2MIN	325	125
Ni@GNP BM-KMW3MIN	303	106
GNP BM	258	185
GNPBM-KMW2MIN	266	199
Pd@CNT-GNP BM	259	172

Tab 6.1 The BET surface area and micropore size of the Ni@GNP sample prepared by the different method.

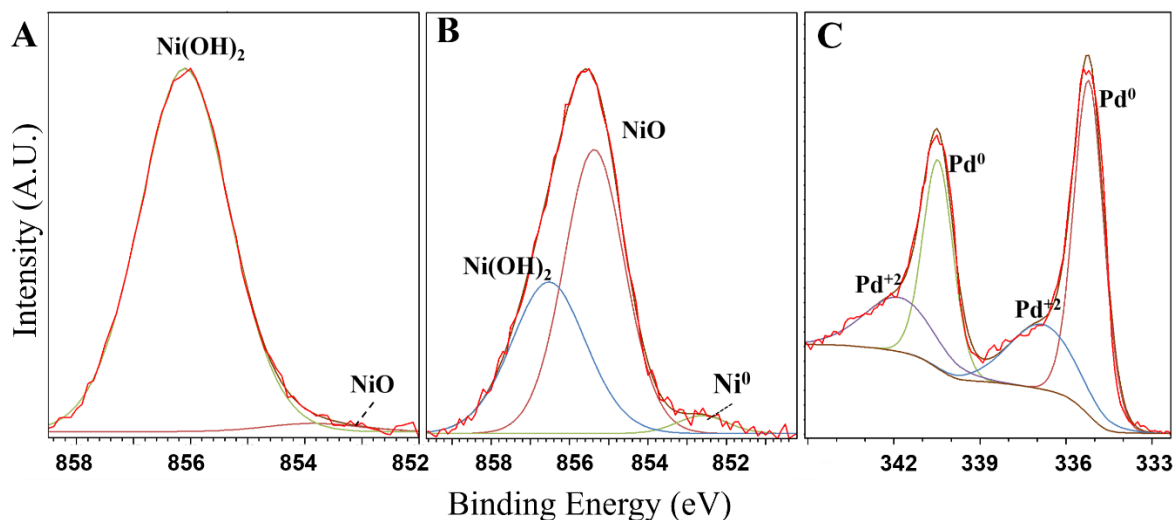


Figure 6-6 XPS result shows the different Ni and Pd peaks in the sample (A) Ni@GNP BM, (B) Ni@GNP BM-KMW2MIN and (C) Pd@CNT-GNP Hydrazine and Microwave reduction

Sample	Ni Crystal size (nm)	Pd Crystal size (nm)
Ni@GNP BM	3	-
Ni@GNP BM-KMW2MIN	33	-
Pd@Ni-CNT-GNP BM	37	4.7
Pd@Ni-CNT-GNP Hydrazine and Microwave reduction	34	4.9

Tab 6.2 XRD result shows crystal size of Ni and Pd in different samples.

6.3.2 Immobilize the Pd nanoparticle on the Ni-CNT-GNP hybrid

Two different methods were selected to immobilize the Pd nanoparticle to the graphene. One method is through ball milling the Pd(OAc)₂ with the Ni-CNT-GNP support. The benefit of the method is that this method is a facile and solventless approach. The previous study suggests that carbon nanotube would reduce the Pd(OAc)₂ and generate Pd nanoparticle. However, one hypothesis is the additional ball milling may destroy the 3-D structure of CNT-GNP or at least remove the shell of the carbon nanotube. The second method to immobilize the Pd nanoparticle is through wet impregnation of the Pd salt and the support then reduce the Pd salt with hydrazine and

microwave heating. Both two Pd catalyst was successfully prepared and characteristic by SEM, STEM, XRD, physisorption, and XPS.

The XPS study of the microwave treated Ni@GNP shows critical evidence that Ni was coated by the carbon nanotube and graphene which eliminated the contact of the Ni nanoparticle with the ambient atmosphere resulting in a large amount of unoxidized metallic Ni nanoparticle. Some of the Ni nanoparticles in the Ni@GNP sample was not covered by carbon nanotube and oxidized to Ni^{+2} which is consistent with the SEM observation. Fig 6.5 shows the charge state of Pd nanoparticle after supported on graphene. The major portion of the Pd nanoparticle is metallic Pd. In contrast, a small portion of Pd was oxidized to Pd^{+2} . Table 6.2 shows the crystal size of Ni nanoparticle and Pd nanoparticle. The size of Ni nanoparticle is small after ball milling with graphene nanoplates. However, the intense microwave treatment causes quickly agglomeration of the nanoparticle. The average crystal size of the Ni nanoparticle reaches 33 nm after 2 mins of microwave irradiation. To immobilize the Pd nanoparticle on the hybrid materials, the different method results in the similar size of Pd nanoparticles. The BET surface area study (tab 6.1) of the Pd decorated Ni-CNT-GNP indicates the addition of the Pd nanoparticle slightly decrease the overall surface area, however, created much more microporous.

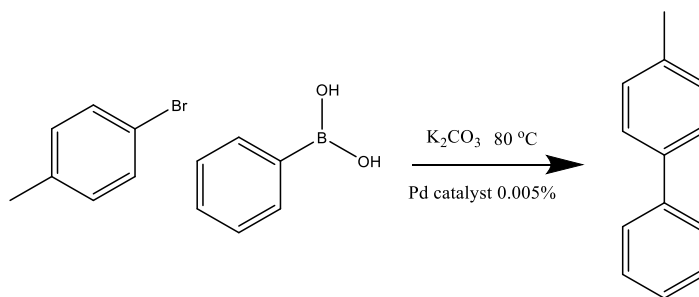


Figure 6-7 Model Suzuki reaction catalyzed by the Pd@GNP-CNT catalyst

Catalyst	TOF(h ⁻¹)
Pd@GNP-CNT BM	105,000
Pd@GNP-CNT CO	120,000
Pd@ Activated carbon	11,000
Ni@GNP500 CO-MW/hydrazine(PPh ₃)/Ar ₂	20
Ni@GNP500 BM-KMW/hydrazine/Ar ₂	0

Table 6.3 TOF of Pd and Ni-based catalysts generated by different method tested for a model Suzuki reaction.

**See me about this data.

Pd catalyst 0.5 mol%
2 equiv PhI(OAc)₂
MeOH 80 °C
15 MIN

Catalyst	TOF(h ⁻¹)
Pd@GCNT BM	1,200
Pd@GCNT CO	350
Pd@activated carbon	Trace
Ni@GNP CO	0
Ni@GNP BM-KMW	0

Table 6.4 TOF of Pd and Ni-based catalysts generated by different method tested for model a model C-H activation reaction.

A Model Suzuki reaction was selected to test the catalytic reactivity of the Pd@GNP-CNT catalysts. Tab 6.3 lists the turnover frequency of different catalyst for the same reaction. Without the presence of the Pd nanoparticles, the hybrid Ni-GNP-CNT support substrate has no catalytic activity even after pre-reduce the Ni nanoparticle by hydrazine or triphenylphosphine. In contrast, Ni nanoparticle immobilized on GNP by the co-reduction method is able to catalyze the reaction

with relatively low reaction rate. The catalysts were also tested with a model C-H activation reaction shown in Table 6.4. The Pd/NiGCNT BM catalyst was significantly more active than other catalysts tested. Since the catalytic cycle of the C-H activation is from Pd⁺² to Pd⁺⁴, the higher reactivity of Pd/NiGCNT BM catalyst is believed originate from the higher Pd⁺² content.

6.4 Conclusion

The graphitic one-dimensional (1D) carbon nanotube and two-dimensional (2D) graphene are important materials in catalysis design. The integration of the 1D carbon nanotube and 2D graphene into a three-dimensional (3D) composite (GCNT) to combine the advantages of the high surface area provided by the atomic thin sheet of graphene and the high aspect ratio of the carbon nanotube is of significant interest. In this study, we reported a facile and solventless method to prepare the 3D GCNT. The carbon nanotubes were generated on graphene using the “tip growth” mechanism via a Ni-catalyzed and microwave irradiation assisted reaction. Then 3D Ni@GCNT was functionalized and Pd nanoparticles were deposited using microwave irradiation. The Ni-Pd@GCNT materials act as a multifunctional catalyst for cross-coupling reaction having not only high activity for both types of reactions but also being synthesized in highly scalable routes. It is interesting to extend the scope of the reaction to include certain electrochemistry which would be benefited by the modified electronic property of the hybrid support.

Chapter VII Conclusion and direction of future work

This combined theoretical and experimental study focused on fundamentally analyzing the role of graphene as a support substrate provides answers to several important questions in the realm of the heterogeneous catalysis in cross-coupling reactions. The stability study and heterogeneity tests have predicted and proven the importance of the presence of the defected sites on the graphene to stabilize the metal nanoparticles. The strong interaction and large charge flow between the metal cluster and the graphene support are not only stabilizing the supported metal but also enhancing the charge transfer of the supported metal. The activation calculations by DFT and experiments demonstrate the enhanced charge transfer by the graphene support would reduce the activation energy of both the charge donating steps and the charge withdrawn steps in the reaction cycle of a cross-coupling reaction. The theoretical study on the full reaction cycle of the Suzuki reaction also revealed the effect of the size and the coordination of the metal cluster on the activation energy. The study on the first-row transition metal nanoparticle catalyzed cross-coupling reactions demonstrate the graphene support system could activate different metal clusters and tune their electronic properties. By adjusting the size and the structure Ni cluster, the graphene supported Ni on graphene catalyst has the comparable capability to catalyze cross-coupling reactions. Furthermore, Ni nanoparticles also possess the key to further modify the structure and function of the graphene support.

The current work provides a fundamental understanding and future direction for the cross-coupling reaction catalyzed by graphene supported nanocatalyst. However, limited by the computational method and the computation capability as well as the experimental methods, a lot of future work in this area is still waiting for the challenger. For the stability study of the graphene supported system, diffusion and entropy of the system were not considered by the current

calculation method due to the accuracy and feasibility of the calculation. For the theoretical calculation of the reaction cycle, one important improvement to increase the accuracy of the calculation in the future is to consider more factors that affect the activation energy which are already been proven to be vital for the reaction, such as the solvent, the base effect, and the oxidation of the metal nanoparticles. Furthermore, increasing the size of the metal cluster in the theoretical calculation to several nanometers as the experiments describe also enable better correlation between the experimental data and theoretical result. Calculating the activation energy in separated steps in the experimental measurement, which may require to using more sophisticated AFM method, would provide much critical information to understand the reaction mechanism which cannot be reflected by the theoretical work.

As described by the theoretical calculation, the size of the defect site on the graphene and the size metal nanoparticle significantly affect the reactivity as well as the stability of the catalyst. The capability to specifically generate certain size and structure of defect sites on graphene and the suitable metal or bimetallic nanoparticles enable the tuning of the electronic properties of the catalyst which could also be broadly used in electrochemistry, hydrogen storage as well as other organic reactions.

Appendix

Appendix A The binding energy of Pd₁₋₄ bound to various sizes and structures of vacancy defected graphene are listed, along with the spin multiplicity.

Pd-Defected graphene	Size of Vacancy (Num. of C)	Pd binding energy (eV)	Spin multiplicity
Pd-DV(7-55-5)	0	1.8	1
Pd-DV(555-3)	1	5.4	1
Pd-DV(5555-7777)	2	1.7	1
Pd-DV(777-555)	2	2.1	1
Pd-DV(5-8-5)	2	4.3	1
Pd-DV(5-7-5-13)	3	7.1	1
Pd-DV(18)	6	7.2	1
Pd ₂ -DV(18)	6	12.6	1
Pd ₂ -DV(17-5)	7	13.0	1
Pd ₂ -DV(22)	10	13.8	1
Pd ₃ -DV(17-5)	7	14.2	1
Pd ₃ -DV(22)	10	14.5	1
Pd ₃ -DV(24)	13	15.8	1
Pd ₄ -DV(18)	6	13.5	1
Pd ₄ -DV(22)	10	15.6	1
Pd ₄ -DV(24)	13	17.9	1

**Appendix B Individual Pd atom charge states in double vacancy defected graphene
supported Pd_n clusters (n=1-14)**

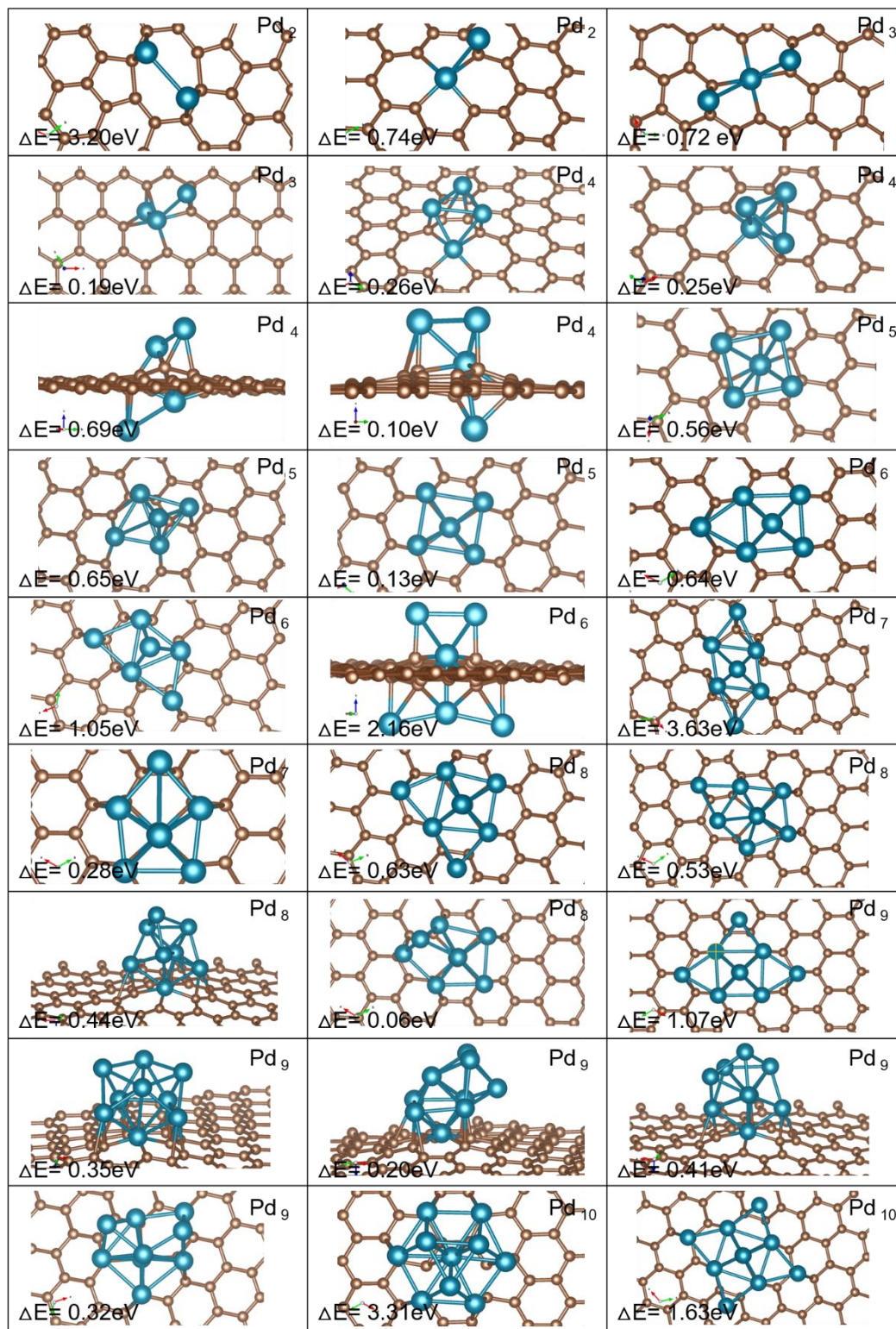
Pd ₁₋₁₄		Pd ₁	Pd ₂	Pd ₃	Pd ₄	Pd ₅	Pd ₆	Pd ₇	Pd ₈	Pd ₉	Pd ₁₀	Pd ₁₁	Pd ₁₂	Pd ₁₃	Pd ₁₄
Anchor (e ⁻)	Pd-1	9.46	9.51	9.42	9.42	9.51	9.39	9.41	9.39	9.41	9.41	9.41	9.41	9.42	9.43
Bottom layer (e ⁻)	Pd-2		9.67	9.91	9.86	9.83	9.89	9.89	9.82	9.87	9.82	9.82	9.82	9.86	9.92
	Pd-3			9.88	9.87	9.89	9.88	9.91	9.86	9.82	9.93	9.83	9.85	9.95	9.90
	Pd-4				10.07	9.82	9.88	9.84	9.90	9.84	9.85	9.86	9.85	9.88	9.83
	Pd-5					10.14	9.90	9.87	9.85	9.83	9.87	9.88	9.83	9.87	9.87
	Pd-6						10.10	9.85	10.01	9.91	9.97	9.89	9.97	9.90	9.84
	Pd-7							10.10	10.04	10.08	10.05	9.97	9.97	10.00	9.96
Top layer (e ⁻)	Pd-8							10.07	10.03	10.01	10.01	10.05	10.05	10.08	
	Pd-9								10.07	10.07	10.07	10.04	10.04	10.05	
	Pd-10									10.01	10.05	10.04	10.03	10.01	
	Pd-11										10.01	10.04	10.06	10.00	
	Pd-12											10.04	10.05	10.03	
	Pd-13												10.05	10.07	
	Pd-14														

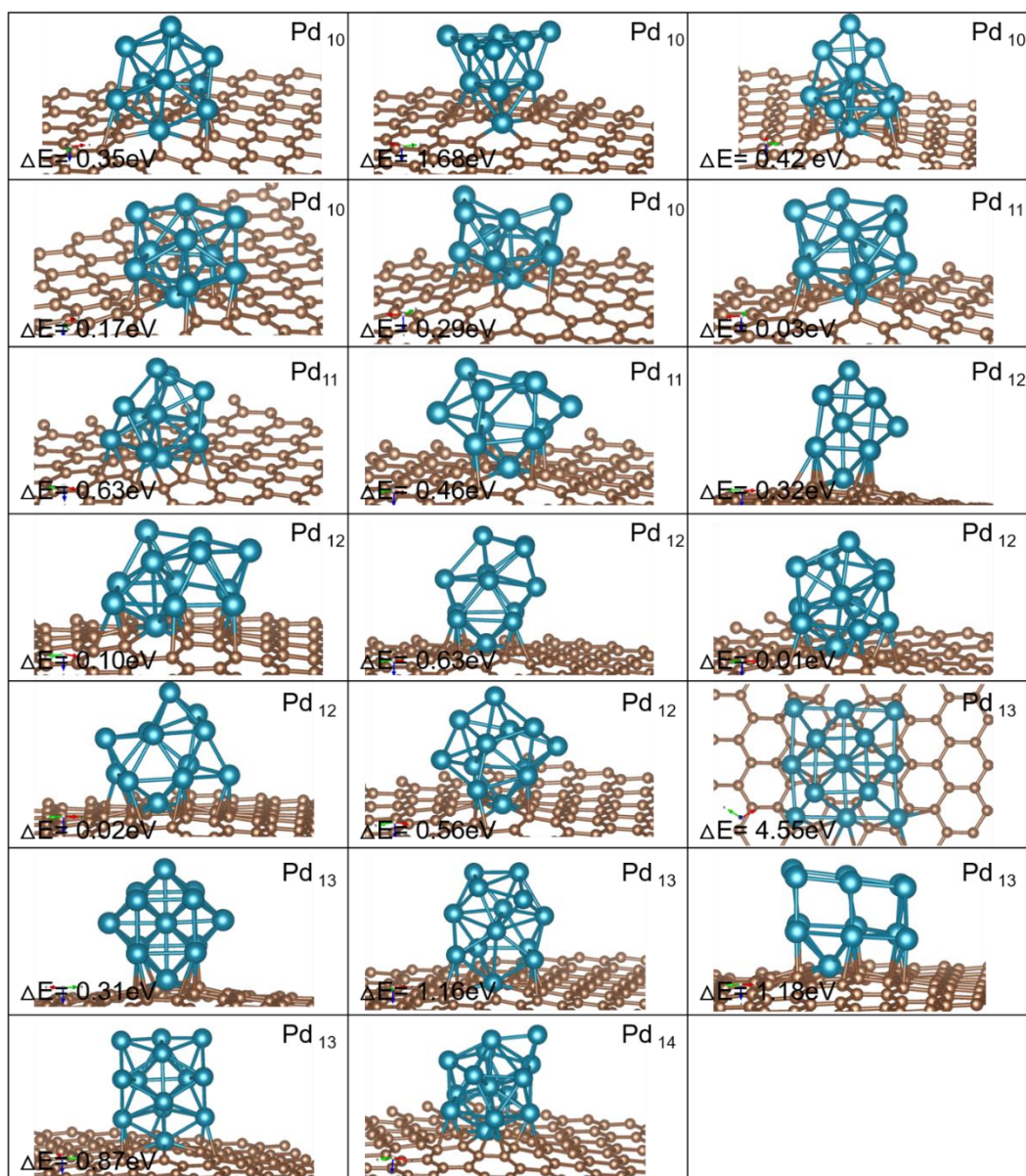
Appendix C Charge state of free and supported Pd_n cluster and phenylboronic acid in transmetallation step.

The charge state of transmetallation step					Net charge flow Phenyl-B(OH) ₃	Activation energy
Pd Cluster		Initial	transition	product		
Pd ₁	Phenyl	-0.90	-0.36	-0.21	0.25e	0.38ev
	B(OH) ₃	+0.43	0	-0.01		
	Phenyl-B(OH) ₃	-0.47	-0.36	-0.22		
	Pd	+0.65	0.67	0.42		
Pd ₄	Phenyl	-0.87	-0.34	-0.19	0.36e	0.3ev
	B(OH) ₃	+0.31	-0.03	-0.01		
	Phenyl-B(OH) ₃	-0.56	-0.37	-0.2		
	Pd	+0.85	+0.46	+0.41		
Pd ₁₃	Phenyl	-0.95	-0.32	-0.20	0.29e	0.34ev
	B(OH) ₃	+0.42	+0.03	-0.04		
	Phenyl-B(OH) ₃	-0.53	-0.3	-0.24		
	Pd	+0.91	+0.7	+0.6		
Pd ₁₃ supported	Phenyl	-0.89	-0.3	-0.21	0.35e	0.3ev
	B(OH) ₃	+0.33	-0.01	0		
	Phenyl-B(OH) ₃	-0.56	-0.31	-0.21		
	Pd	+2.0	+1.91	+1.72		
Pd ₄ supported	Phenyl	-0.76	-0.49	-0.15	0.43e	0.16ev
	B(OH) ₃	0.21	0.07	0.03		
	Phenyl-B(OH) ₃	-0.55	-0.42	-0.12		
	Pd	+1.87	+1.81	+1.71		

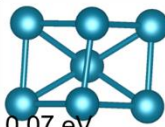
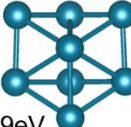
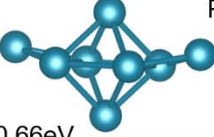
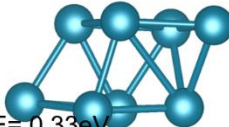
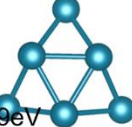
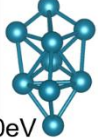
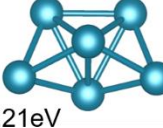
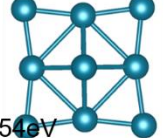
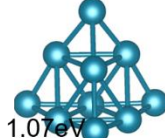
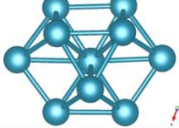
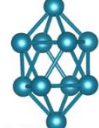
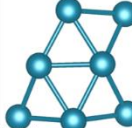
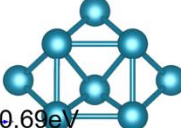
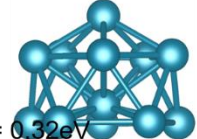
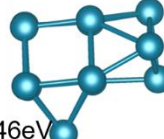
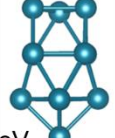
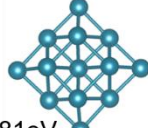
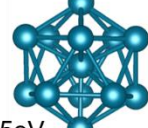
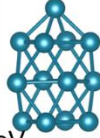
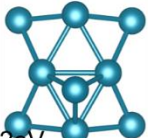
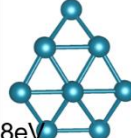
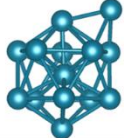
Pd ₁₄ supported	Phenyl	-0.90	-0.39	-0.25	0.31e	0.33ev
	B(OH) ₃	0.37	0.06	0.03		
	Phenyl-B(OH) ₃	-0.53	-0.33	-0.22		
	Pd	+2.0	+1.81	+1.56		
Pd/P(Me) ₃	Phenyl	-0.86	-0.58	-0.43	0.16e	0.42ev
	B(OH) ₃	0.24	0.04	-0.03		
	Phenyl-B(OH) ₃	-0.62	-0.54	-0.46		
	Pd	0.45	0.30	0.21		

Appendix D Different structure of Pd_n Cluster n=2-14 supported on double vacancy defected graphene. ΔE is the energy difference from the ground state.





Appendix E Different structure of Pd_n Cluster n=4-14. ΔE is the energy difference from the ground state.

 Pd ₄ ΔE= 0.51eV	 Pd ₅ ΔE= 0.03eV	 Pd ₇ ΔE= 0.07 eV
 Pd ₈ ΔE= 0.39eV	 Pd ₈ ΔE= 0.66eV	 Pd ₈ ΔE= 0.33eV
 Pd ₉ ΔE= 0.70eV	 Pd ₉ ΔE= 0.29eV	 Pd ₉ ΔE= 0.60eV
 Pd ₉ ΔE= 0.21eV	 Pd ₁₀ ΔE= 0.54eV	 Pd ₁₀ ΔE= 1.07eV
 Pd ₁₀ ΔE= 0.76eV	 Pd ₁₀ ΔE= 0.35eV	 Pd ₁₁ ΔE= 0.08eV
 Pd ₁₂ ΔE= 0.69eV	 Pd ₁₂ ΔE= 0.32eV	 Pd ₁₂ ΔE= 0.46eV
 Pd ₁₂ ΔE= 0.43eV	 Pd ₁₃ ΔE= 0.81eV	 Pd ₁₃ ΔE= 0.35eV
 Pd ₁₃ ΔE= 0.54eV	 Pd ₁₃ ΔE= 0.41eV	 Pd ₁₃ ΔE= 0.32eV
 Pd ₁₃ ΔE= 0.28eV	 Pd ₁₄	

Appendix F Charge state in oxidative addition step.

The table lists the net Bader charge state of the Pd_n cluster, bromine atom and benzoic acid fragment when the 4-bromo-benzoic acid is in the initial state on the Pd_n cluster, at the transition state, and at the final product. Note that in isolated 4-bromobenzoic acid, the charge on Br is -0.58 e⁻ and benzoic acid is 0.58 e⁻. The table lists the net Bader charge state of the Pd_n cluster, bromine atom and benzoic acid fragment when the 4-bromo-benzoic acid is in the initial state on the Pd_n cluster, at the transition state, and at the final product. Note that in isolated 4-bromobenzoic acid, the charge on Br is -0.58 e⁻ and benzoic acid is 0.58 e⁻.

	Initial state(e ⁻)	Transition state(e ⁻)	Final state(e ⁻)
Pd	0.22	0.24	0.40
Benzoic acid	-0.13	-0.10	-0.05
Bromine	-0.08	-0.13	-0.35
Pd ₄	0.17	0.20	0.65
Benzoic acid	-0.14	-0.10	-0.20
Bromine	-0.024	-0.10	-0.45
Pd ₁₃	0.34	0.48	0.74
Benzoic acid	-0.27	-0.24	-0.38
Bromine	-0.064	-0.24	-0.36
Pd ₁₄	0.16	0.31	0.59
Benzoic acid	-0.10	-0.10	-0.24

Bromine	-0.06	-0.20	-0.35
---------	-------	-------	-------

The table lists the net Bader charge state of the Pd_n cluster not including the anchor atom, the Pd anchor atom, the bromine atom, the benzoic acid fragment, and the defected graphene sheet when the 4-bromo-benzoic acid is in the initial state on the Pd_n cluster, at the transition state, and at the final product.

	Isolated catalyst(e ⁻)	Initial state(e ⁻)	Transition state(e ⁻)	Final state(e ⁻)
Pd ₄	0.76	1.53	1.53	1.59
Anchor Pd	0.57	0.57	0.57	0.58
Benzoic acid	-	-0.29	-0.31	-0.23
Bromine	-	-0.06	-0.06	-0.44
Defected graphene	-0.76	-1.18	-1.15	-0.92
Pd ₁₃	1.10	1.54	1.59	1.82
Anchor Pd	0.57	0.58	0.58	0.57
Benzoic acid	-	-0.30	-0.23	-0.33
Bromine	-	-0.07	-0.22	-0.37
Defected graphene	-1.10	-1.16	-1.15	-1.12
Pd ₁₄	1.07	1.24	1.21	1.75
Anchor Pd	0.57	0.57	0.57	0.57
Benzoic acid	-	-0.09	-0.05	-0.29
Bromine	-	-0.07	-0.09	-0.40
Defected graphene	-1.07	-1.08	-1.07	-1.07

Reference:

1. P. T. Anastas, M. M. Kirchhoff, T. C. Williamson, Catalysis as a foundational pillar of green chemistry. *Applied Catalysis A: General* **221**, 3-13 (2001); published online Epub11/30/ ([http://dx.doi.org/10.1016/S0926-860X\(01\)00793-1](http://dx.doi.org/10.1016/S0926-860X(01)00793-1)).
2. C. R. Catlow, M. Davidson, C. Hardacre, G. J. Hutchings, Catalysis making the world a better place. *Philosophical transactions. Series A, Mathematical, physical, and engineering sciences* **374**, 20150089 (2016); published online Epub06/09/accepted (10.1098/rsta.2015.0089).
3. C. A. Busacca, D. R. Fandrick, J. J. Song, C. H. Senanayake, The Growing Impact of Catalysis in the Pharmaceutical Industry. *Advanced Synthesis & Catalysis* **353**, 1825-1864 (2011)10.1002/adsc.201100488).
4. J. Magano, J. R. Dunetz, Large-Scale Applications of Transition Metal-Catalyzed Couplings for the Synthesis of Pharmaceuticals. *Chemical Reviews* **111**, 2177-2250 (2011); published online Epub2011/03/09 (10.1021/cr100346g).
5. I. Shinkai, A. O. King, R. D. Larsen, in *Pure and Applied Chemistry*. (1994), vol. 66, pp. 1551.
6. I. P. Beletskaya, A. V. Cheprakov, in *The Mizoroki–Heck Reaction*. (John Wiley & Sons, Ltd, 2009), pp. 51-132.
7. A. Jutand, in *The Mizoroki–Heck Reaction*. (John Wiley & Sons, Ltd, 2009), pp. 1-50.
8. M. Rouhi, SHINING LIGHT ON CHIRALITY. *Chemical & Engineering News Archive* **82**, 6 (2004); published online Epub2004/04/12 (10.1021/cen-v082n015.p006).
9. A. Suzuki, Recent advances in the cross-coupling reactions of organoboron derivatives with organic electrophiles, 1995–1998. *Journal of Organometallic Chemistry* **576**, 147-

- 168 (1999); published online Epub1999/03/15/ ([http://dx.doi.org/10.1016/S0022-328X\(98\)01055-9](http://dx.doi.org/10.1016/S0022-328X(98)01055-9)).
10. N. Miyaura, in *Cross-Coupling Reactions: A Practical Guide*, N. Miyaura, Ed. (Springer Berlin Heidelberg, Berlin, Heidelberg, 2002), pp. 11-59.
 11. C. Sambiasi, S. P. Marsden, A. J. Blacker, P. C. McGowan, Copper catalyzed Ullmann type chemistry: from mechanistic aspects to modern development. *Chemical Society Reviews* **43**, 3525-3550 (2014)10.1039/C3CS60289C).
 12. F. Ullmann, Ueber eine neue Bildungsweise von Diphenylaminderivaten. *Berichte der deutschen chemischen Gesellschaft* **36**, 2382-2384 (1903)10.1002/cber.190303602174).
 13. F. Ullmann, P. Sponagel, Ueber die Phenylirung von Phenolen. *Berichte der deutschen chemischen Gesellschaft* **38**, 2211-2212 (1905)10.1002/cber.190503802176).
 14. I. Goldberg, Ueber Phenylirungen bei Gegenwart von Kupfer als Katalysator. *Berichte der deutschen chemischen Gesellschaft* **39**, 1691-1692 (1906)10.1002/cber.19060390298).
 15. W. R. H. Hurtley, CCXLIV.-Replacement of halogen in orthobromo-benzoic acid. *Journal of the Chemical Society (Resumed)*, 1870-1873 (1929)10.1039/JR9290001870).
 16. R. F. Heck, Mechanism of arylation and carbomethoxylation of olefins with organopalladium compounds. *Journal of the American Chemical Society* **91**, 6707-6714 (1969); published online Epub1969/11/01 (10.1021/ja01052a029).
 17. W. Dai, J. Xiao, G. Jin, J. Wu, S. Cao, Palladium- and Nickel-Catalyzed Kumada Cross-Coupling Reactions of gem-Difluoroalkenes and Monofluoroalkenes with Grignard Reagents. *The Journal of Organic Chemistry* **79**, 10537-10546 (2014); published online Epub2014/11/07 (10.1021/jo5022234).

18. S. Z. Tasker, E. A. Standley, T. F. Jamison, Recent advances in homogeneous nickel catalysis. *Nature* **509**, 299-309 (2014); published online Epub05/15/print (10.1038/nature13274).
19. F.-S. Han, Transition-metal-catalyzed Suzuki-Miyaura cross-coupling reactions: a remarkable advance from palladium to nickel catalysts. *Chemical Society Reviews* **42**, 5270-5298 (2013)10.1039/C3CS35521G).
20. K. Sonogashira, Y. Tohda, N. Hagihara, A convenient synthesis of acetylenes: catalytic substitutions of acetylenic hydrogen with bromoalkenes, iodoarenes and bromopyridines. *Tetrahedron Letters* **16**, 4467-4470 (1975); published online Epub1975/01/01/ ([http://dx.doi.org/10.1016/S0040-4039\(00\)91094-3](http://dx.doi.org/10.1016/S0040-4039(00)91094-3)).
21. L. Cassar, Synthesis of aryl- and vinyl-substituted acetylene derivatives by the use of nickel and palladium complexes. *Journal of Organometallic Chemistry* **93**, 253-257 (1975); published online Epub1975/07/08/ ([http://dx.doi.org/10.1016/S0022-328X\(00\)94048-8](http://dx.doi.org/10.1016/S0022-328X(00)94048-8)).
22. D. Haas, J. M. Hammann, R. Greiner, P. Knochel, Recent Developments in Negishi Cross-Coupling Reactions. *ACS Catalysis* **6**, 1540-1552 (2016); published online Epub2016/03/04 (10.1021/acscatal.5b02718).
23. A. O. King, N. Okukado, E.-i. Negishi, Highly general stereo-, regio-, and chemo-selective synthesis of terminal and internal conjugated enynes by the Pd-catalysed reaction of alkynylzinc reagents with alkenyl halides. *Journal of the Chemical Society, Chemical Communications*, 683-684 (1977)10.1039/C39770000683).
24. C. Cordovilla, C. Bartolomé, J. M. Martínez-Ilarduya, P. Espinet, The Stille Reaction, 38 Years Later. *ACS Catalysis* **5**, 3040-3053 (2015); published online Epub2015/05/01 (10.1021/acscatal.5b00448).

25. J. K. Stille, The Palladium-Catalyzed Cross-Coupling Reactions of Organotin Reagents with Organic Electrophiles [New Synthetic Methods (58)]. *Angewandte Chemie International Edition in English* **25**, 508-524 (1986)10.1002/anie.198605081).
26. Y. Nakao, T. Hiyama, Silicon-based cross-coupling reaction: an environmentally benign version. *Chemical Society Reviews* **40**, 4893-4901 (2011)10.1039/C1CS15122C).
27. C. C. C. Johansson Seechurn, M. O. Kitching, T. J. Colacot, V. Snieckus, Palladium-Catalyzed Cross-Coupling: A Historical Contextual Perspective to the 2010 Nobel Prize. *Angewandte Chemie International Edition* **51**, 5062-5085 (2012)10.1002/anie.201107017).
28. T. Colacot, *New Trends in Cross-Coupling : Theory and Applications*. (2015).
29. F. Zhu, M. J. Rourke, T. Yang, J. Rodriguez, M. A. Walczak, Highly Stereospecific Cross-Coupling Reactions of Anomeric Stannanes for the Synthesis of C-Aryl Glycosides. *Journal of the American Chemical Society* **138**, 12049-12052 (2016); published online Epub2016/09/21 (10.1021/jacs.6b07891).
30. A. Chatterjee, T. R. Ward, Recent Advances in the Palladium Catalyzed Suzuki–Miyaura Cross-Coupling Reaction in Water. *Catalysis Letters* **146**, 820-840 (2016)10.1007/s10562-016-1707-8).
31. P. Ruiz-Castillo, S. L. Buchwald, Applications of Palladium-Catalyzed C–N Cross-Coupling Reactions. *Chemical Reviews* **116**, 12564-12649 (2016); published online Epub2016/10/12 (10.1021/acs.chemrev.6b00512).
32. H. M. L. Davies, D. Morton, Recent Advances in C–H Functionalization. *The Journal of Organic Chemistry* **81**, 343-350 (2016); published online Epub2016/01/15 (10.1021/acs.joc.5b02818).

33. J. Choi, G. C. Fu, Transition metal–catalyzed alkyl-alkyl bond formation: Another dimension in cross-coupling chemistry. *Science* **356**, (2017)10.1126/science.aaf7230).
34. R. Jana, T. P. Pathak, M. S. Sigman, Advances in Transition Metal (Pd,Ni,Fe)-Catalyzed Cross-Coupling Reactions Using Alkyl-organometallics as Reaction Partners. *Chemical Reviews* **111**, 1417-1492 (2011); published online Epub2011/03/09 (10.1021/cr100327p).
35. M. Tobisu, N. Chatani, Cross-Couplings Using Aryl Ethers via C–O Bond Activation Enabled by Nickel Catalysts. *Accounts of Chemical Research* **48**, 1717-1726 (2015); published online Epub2015/06/16 (10.1021/acs.accounts.5b00051).
36. D. R. Pye, N. P. Mankad, Bimetallic catalysis for C-C and C-X coupling reactions. *Chemical Science* **8**, 1705-1718 (2017)10.1039/C6SC05556G).
37. N. Hazari, P. R. Melvin, M. M. Beromi, Well-defined nickel and palladium precatalysts for cross-coupling. **1**, 0025 (2017); published online Epub03/01/online (10.1038/s41570-017-0025).
38. X. Hu, Nickel-catalyzed cross coupling of non-activated alkyl halides: a mechanistic perspective. *Chemical Science* **2**, 1867-1886 (2011)10.1039/C1SC00368B).
39. Ö. Metin, S. F. Ho, C. Alp, H. Can, M. N. Mankin, M. S. Gültekin, M. Chi, S. Sun, Ni/Pd core/shell nanoparticles supported on graphene as a highly active and reusable catalyst for Suzuki-Miyaura cross-coupling reaction. *Nano Research* **6**, 10-18 (2013); published online EpubJanuary 01 (10.1007/s12274-012-0276-4).
40. A. J. J. Lennox, G. C. Lloyd-Jones, Transmetalation in the Suzuki–Miyaura Coupling: The Fork in the Trail. *Angewandte Chemie International Edition* **52**, 7362-7370 (2013)10.1002/anie.201301737).

41. K. C. Nicolaou, P. G. Bulger, D. Sarlah, Palladium-Catalyzed Cross-Coupling Reactions in Total Synthesis. *Angewandte Chemie International Edition* **44**, 4442-4489 (2005).
42. R. A. Altman, S. L. Buchwald, Pd-catalyzed Suzuki-Miyaura reactions of aryl halides using bulky biarylmonophosphine ligands. *Nat. Protocols* **2**, 3115-3121 (2007); published online Epub12//print (
43. I. W. Davies, L. Matty, D. L. Hughes, P. J. Reider, Are Heterogeneous Catalysts Precursors to Homogeneous Catalysts? *Journal of the American Chemical Society* **123**, 10139-10140 (2001).
44. S. P. Andrews, A. F. Stepan, H. Tanaka, S. V. Ley, M. D. Smith, Heterogeneous or Homogeneous? A Case Study Involving Palladium-Containing Perovskites in the Suzuki Reaction. *Advanced Synthesis & Catalysis* **347**, 647-654 (2005)10.1002/adsc.200404331).
45. D. Astruc, F. Lu, J. R. Aranzaes, Nanoparticles as Recyclable Catalysts: The Frontier between Homogeneous and Heterogeneous Catalysis. *Angewandte Chemie International Edition* **44**, 7852-7872 (2005)10.1002/anie.200500766).
46. J. R. H. Ross, *Heterogeneous Catalysis Fundamentals and Applications*. (2012).
47. F. Bozso, G. Ertl, M. Grunze, M. Weiss, Interaction of nitrogen with iron surfaces. *Journal of Catalysis* **49**, 18-41 (1977); published online Epub1977/07/01/ ([http://dx.doi.org/10.1016/0021-9517\(77\)90237-8](http://dx.doi.org/10.1016/0021-9517(77)90237-8)).
48. H. Jahangiri, J. Bennett, P. Mahjoubi, K. Wilson, S. Gu, A review of advanced catalyst development for Fischer-Tropsch synthesis of hydrocarbons from biomass derived syn-gas. *Catalysis Science & Technology* **4**, 2210-2229 (2014)10.1039/C4CY00327F).

49. Y. Wang, H. Arandiyani, J. Scott, A. Bagheri, H. Dai, R. Amal, Recent advances in ordered meso/macroporous metal oxides for heterogeneous catalysis: a review. *Journal of Materials Chemistry A* **5**, 8825-8846 (2017)10.1039/C6TA10896B).
50. F. Zaera, Nanostructured materials for applications in heterogeneous catalysis. *Chemical Society Reviews* **42**, 2746-2762 (2013)10.1039/C2CS35261C).
51. H. M. Torres Galvis, J. H. Bitter, C. B. Khare, M. Ruitenbeek, A. I. Dugulan, K. P. de Jong, Supported Iron Nanoparticles as Catalysts for Sustainable Production of Lower Olefins. *Science* **335**, 835-838 (2012); published online Epub2012-02-17 00:00:00 (10.1126/science.1215614).
52. D. Cantillo, C. O. Kappe, Immobilized Transition Metals as Catalysts for Cross-Couplings in Continuous Flow—A Critical Assessment of the Reaction Mechanism and Metal Leaching. *ChemCatChem* **6**, 3286-3305 (2014)10.1002/cctc.201402483).
53. Yin, J. Liebscher, Carbon–Carbon Coupling Reactions Catalyzed by Heterogeneous Palladium Catalysts. *Chemical Reviews* **107**, 133-173 (2007); published online Epub2007/01/01 (10.1021/cr0505674).
54. T. Baran, T. Inanan, A. Menteş, Synthesis, characterization, and catalytic activity in Suzuki coupling and catalase-like reactions of new chitosan supported Pd catalyst. *Carbohydrate Polymers* **145**, 20-29 (2016); published online Epub7/10/ (<http://dx.doi.org/10.1016/j.carbpol.2016.03.019>).
55. K. Köhler, R. G. Heidenreich, S. S. Soomro, S. S. Pröckl, Supported Palladium Catalysts for Suzuki Reactions: Structure-Property Relationships, Optimized Reaction Protocol and Control of Palladium Leaching. *Advanced Synthesis & Catalysis* **350**, 2930-2936 (2008).

56. A. Gniewek, J. J. Ziółkowski, A. M. Trzeciak, M. Zawadzki, H. Grabowska, J. Wrzyszc, Palladium nanoparticles supported on alumina-based oxides as heterogeneous catalysts of the Suzuki–Miyaura reaction. *Journal of Catalysis* **254**, 121-130 (2008); published online Epub2/15/ (<http://dx.doi.org/10.1016/j.jcat.2007.12.004>).
57. C. M. Crudden, M. Sateesh, R. Lewis, Mercaptopropyl-Modified Mesoporous Silica: A Remarkable Support for the Preparation of a Reusable, Heterogeneous Palladium Catalyst for Coupling Reactions. *Journal of the American Chemical Society* **127**, 10045-10050 (2005); published online Epub2005/07/01 (10.1021/ja0430954).
58. B. Karimi, D. Enders, New N-Heterocyclic Carbene Palladium Complex/Ionic Liquid Matrix Immobilized on Silica: Application as Recoverable Catalyst for the Heck Reaction. *Organic Letters* **8**, 1237-1240 (2006); published online Epub2006/03/01 (10.1021/ol060129z).
59. H. Gruber-Woelfler, P. F. Radaschitz, P. W. Feenstra, W. Haas, J. G. Khinast, Synthesis, catalytic activity, and leaching studies of a heterogeneous Pd-catalyst including an immobilized bis(oxazoline) ligand. *Journal of Catalysis* **286**, 30-40 (2012); published online Epub2// (<http://dx.doi.org/10.1016/j.jcat.2011.10.013>).
60. G. M. Scheuermann, L. Rumi, P. Steurer, W. Bannwarth, R. Mülhaupt, Palladium Nanoparticles on Graphite Oxide and Its Functionalized Graphene Derivatives as Highly Active Catalysts for the Suzuki–Miyaura Coupling Reaction. *Journal of the American Chemical Society* **131**, 8262-8270 (2009); published online Epub2009/06/17 (10.1021/ja901105a).
61. A. R. Siamaki, A. E. R. S. Khder, V. Abdelsayed, M. S. El-Shall, B. F. Gupton, Microwave-assisted synthesis of palladium nanoparticles supported on graphene: A highly active and

- recyclable catalyst for carbon–carbon cross-coupling reactions. *Journal of Catalysis* **279**, 1-11 (2011); published online Epub4/1/ (<http://dx.doi.org/10.1016/j.jcat.2010.12.003>).
62. S. Moussa, A. R. Siamaki, B. F. Gupton, M. S. El-Shall, Pd-Partially Reduced Graphene Oxide Catalysts (Pd/PRGO): Laser Synthesis of Pd Nanoparticles Supported on PRGO Nanosheets for Carbon–Carbon Cross Coupling Reactions. *ACS Catalysis* **2**, 145-154 (2012); published online Epub2012/01/06 (10.1021/cs200497e).
63. G. Park, S. Lee, S. J. Son, S. Shin, Pd nanoparticle-silica nanotubes (Pd@SNTs) as an efficient catalyst for Suzuki-Miyaura coupling and sp² C-H arylation in water. *Green Chemistry* **15**, 3468-3473 (2013)10.1039/C3GC41672K).
64. J. K. Nørskov, F. Abild-Pedersen, F. Studt, T. Bligaard, Density functional theory in surface chemistry and catalysis. *Proceedings of the National Academy of Sciences* **108**, 937-943 (2011); published online EpubJanuary 18, 2011 (10.1073/pnas.1006652108).
65. J. K. Norskov, T. Bligaard, J. Rossmeisl, C. H. Christensen, Towards the computational design of solid catalysts. *Nature chemistry* **1**, 37-46 (2009); published online Epub04//print (
66. H. Eschrig, *The Fundamentals of Density Functional Theory*. (2003).
67. R. A. L. Alan Hinchliffe, Adrian Mulholland, *Chemical Modelling: Applications and Theory*, Volume 4. (2006).
68. P. A. Denis, F. Iribarne, Comparative Study of Defect Reactivity in Graphene. *The Journal of Physical Chemistry C* **117**, 19048-19055 (2013); published online Epub2013/09/19 (10.1021/jp4061945).

69. G. A. Somorjai, M. Yang, The Surface Science of Catalytic Selectivity. *Topics in Catalysis* **24**, 61-72 (2003); published online EpubOctober 01 (10.1023/B:TOCA.0000003077.98309.cf).
70. R. L. Brainard, R. J. Madix, Oxidation of tert-butyl alcohol to isobutylene oxide on a silver(110) surface: the role of unactivated carbon-hydrogen bonds in product selectivity. *Journal of the American Chemical Society* **111**, 3826-3835 (1989); published online Epub1989/05/01 (10.1021/ja00193a012).
71. S. Linic, M. A. Barteau, Formation of a Stable Surface Oxametallacycle that Produces Ethylene Oxide. *Journal of the American Chemical Society* **124**, 310-317 (2002); published online Epub2002/01/01 (10.1021/ja0118136).
72. S. Linic, M. A. Barteau, Construction of a reaction coordinate and a microkinetic model for ethylene epoxidation on silver from DFT calculations and surface science experiments. *Journal of Catalysis* **214**, 200-212 (2003); published online Epub2003/03/10/ ([http://dx.doi.org/10.1016/S0021-9517\(02\)00156-2](http://dx.doi.org/10.1016/S0021-9517(02)00156-2)).
73. B. Hammer, J. K. Nørskov, Theoretical surface science and catalysis—calculations and concepts. *Advances in Catalysis* **45**, 71-129 (2000); published online Epub2000/01/01/ ([http://dx.doi.org/10.1016/S0360-0564\(02\)45013-4](http://dx.doi.org/10.1016/S0360-0564(02)45013-4)).
74. S. Linic, J. Jankowiak, M. A. Barteau, Selectivity driven design of bimetallic ethylene epoxidation catalysts from first principles. *Journal of Catalysis* **224**, 489-493 (2004); published online Epub2004/06/10/ (<http://dx.doi.org/10.1016/j.jcat.2004.03.007>).
75. S. Alayoglu, A. U. Nilekar, M. Mavrikakis, B. Eichhorn, Ru-Pt core-shell nanoparticles for preferential oxidation of carbon monoxide in hydrogen. *Nat Mater* **7**, 333-338 (2008);

(http://www.nature.com/nmat/journal/v7/n4/supinfo/nmat2156_S1.html).

76. P. Liu, A. Logadottir, J. K. Nørskov, Modeling the electro-oxidation of CO and H₂/CO on Pt, Ru, PtRu and Pt₃Sn. *Electrochimica Acta* **48**, 3731-3742 (2003); published online Epub2003/11/15/ ([http://dx.doi.org/10.1016/S0013-4686\(03\)00538-3](http://dx.doi.org/10.1016/S0013-4686(03)00538-3)).
77. F. Studt, F. Abild-Pedersen, T. Bligaard, R. Z. Sørensen, C. H. Christensen, J. K. Nørskov, Identification of Non-Precious Metal Alloy Catalysts for Selective Hydrogenation of Acetylene. *Science* **320**, 1320-1322 (2008)10.1126/science.1156660).
78. E. Shustorovich, A. T. Bell, The thermochemistry of C₂ hydrocarbons on transition metal surfaces: The bond-order-conservation approach. *Surface Science* **205**, 492-512 (1988); published online Epub1988/11/01/ ([http://dx.doi.org/10.1016/0039-6028\(88\)90299-3](http://dx.doi.org/10.1016/0039-6028(88)90299-3)).
79. D.-H. Lim, A. S. Negreira, J. Wilcox, DFT Studies on the Interaction of Defective Graphene-Supported Fe and Al Nanoparticles. *The Journal of Physical Chemistry C* **115**, 8961-8970 (2011); published online Epub2011/05/12 (10.1021/jp2012914).
80. P. T. Araujo, M. Terrones, M. S. Dresselhaus, Defects and impurities in graphene-like materials. *Materials Today* **15**, 98-109 (2012); published online Epub2012/03/01/ ([http://dx.doi.org/10.1016/S1369-7021\(12\)70045-7](http://dx.doi.org/10.1016/S1369-7021(12)70045-7)).
81. R. J. W. E. Lahaye, H. K. Jeong, C. Y. Park, Y. H. Lee, Density functional theory study of graphite oxide for different oxidation levels. *Physical Review B* **79**, 125435 (2009); published online Epub03/27/ (
82. X. Wang, G. Sun, P. Routh, D.-H. Kim, W. Huang, P. Chen, Heteroatom-doped graphene materials: syntheses, properties and applications. *Chemical Society Reviews* **43**, 7067-7098 (2014)10.1039/C4CS00141A).

83. B. Sütay, M. Yurtsever, Adsorption of dihalogen molecules on pristine graphene surface: Monte Carlo and molecular dynamics simulation studies. *Journal of Molecular Modeling* **23**, 150 (2017); published online EpubApril 03 (10.1007/s00894-017-3311-2).
84. S. H. Noh, D. H. Kwak, M. H. Seo, T. Ohsaka, B. Han, First principles study of oxygen reduction reaction mechanisms on N-doped graphene with a transition metal support. *Electrochimica Acta* **140**, 225-231 (2014); published online Epub2014/09/10/ (<http://dx.doi.org/10.1016/j.electacta.2014.03.076>).
85. F. Karlický, M. Otyepka, Band Gaps and Optical Spectra of Chlorographene, Fluorographene and Graphane from G0W0, GW0 and GW Calculations on Top of PBE and HSE06 Orbitals. *Journal of Chemical Theory and Computation* **9**, 4155-4164 (2013); published online Epub2013/09/10 (10.1021/ct400476r).
86. C. R. C. Rêgo, P. Tereshchuk, L. N. Oliveira, J. L. F. Da Silva, Graphene-supported small transition-metal clusters: A density functional theory investigation within van der Waals corrections. *Physical Review B* **95**, 235422 (2017); published online Epub06/14/ (
87. I. López-Corral, E. Germán, A. Juan, M. A. Volpe, G. P. Brizuela, DFT Study of Hydrogen Adsorption on Palladium Decorated Graphene. *The Journal of Physical Chemistry C* **115**, 4315-4323 (2011); published online Epub2011/03/17 (10.1021/jp110067w).
88. B. Jiang, S. Song, J. Wang, Y. Xie, W. Chu, H. Li, H. Xu, C. Tian, H. Fu, Nitrogen-doped graphene supported Pd@PdO core-shell clusters for C-C coupling reactions. *Nano Research* **7**, 1280-1290 (2014); published online EpubSeptember 01 (10.1007/s12274-014-0492-1).
89. D. W. Yuan, C. Liu, Z. R. Liu, Structures and catalytic properties of Pd_mAun_n (m+n=7) bimetallic clusters supported on graphene by first-principles studies. *Physics Letters A* **378**,

408-415 (2014); published online Epub2014/01/17/
(<http://dx.doi.org/10.1016/j.physleta.2013.11.028>).

90. H. Zhou, X. Chen, L. Wang, X. Zhong, G. Zhuang, X. Li, D. Mei, J. Wang, Effect of graphene with nanopores on metal clusters. *Physical Chemistry Chemical Physics* **17**, 24420-24426 (2015)10.1039/C5CP04368A).
91. R. Arrigo, M. E. Schuster, S. Abate, G. Giorgianni, G. Centi, S. Perathoner, S. Wrabetz, V. Pfeifer, M. Antonietti, R. Schlögl, Pd Supported on Carbon Nitride Boosts the Direct Hydrogen Peroxide Synthesis. *ACS Catalysis* **6**, 6959-6966 (2016); published online Epub2016/10/07 (10.1021/acscatal.6b01889).
92. T. Maegawa, Y. Kitamura, S. Sako, T. Udzu, A. Sakurai, A. Tanaka, Y. Kobayashi, K. Endo, U. Bora, T. Kurita, A. Kozaki, Y. Monguchi, H. Sajiki, Heterogeneous Pd/C-Catalyzed Ligand-Free, Room-Temperature Suzuki–Miyaura Coupling Reactions in Aqueous Media. *Chemistry – A European Journal* **13**, 5937-5943 (2007)10.1002/chem.200601795).
93. P. Taladriz-Blanco, P. Hervés, J. Pérez-Juste, Supported Pd Nanoparticles for Carbon–Carbon Coupling Reactions. *Topics in Catalysis* **56**, 1154-1170 (2013)10.1007/s11244-013-0082-6).
94. F. Yang, C. Chi, S. Dong, C. Wang, X. Jia, L. Ren, Y. Zhang, L. Zhang, Y. Li, Pd/PdO nanoparticles supported on carbon nanotubes: A highly effective catalyst for promoting Suzuki reaction in water. *Catalysis Today* **256**, 186-192 (2015); published online Epub2015/11/01/ (<http://dx.doi.org/10.1016/j.cattod.2015.02.026>).
95. A. Corma, H. Garcia, A. Leyva, Catalytic activity of palladium supported on single wall carbon nanotubes compared to palladium supported on activated carbon. *Journal of*

- Molecular Catalysis A: Chemical* **230**, 97-105 (2005); published online Epub2005/04/06/
(<http://dx.doi.org/10.1016/j.molcata.2004.11.030>).
96. X. Chen, Y. Hou, H. Wang, Y. Cao, J. He, Facile Deposition of Pd Nanoparticles on Carbon Nanotube Microparticles and Their Catalytic Activity for Suzuki Coupling Reactions. *The Journal of Physical Chemistry C* **112**, 8172-8176 (2008); published online Epub2008/06/01 (10.1021/jp800610q).
97. M. Gómez-Martínez, E. Buxaderas, I. M. Pastor, D. A. Alonso, Palladium nanoparticles supported on graphene and reduced graphene oxide as efficient recyclable catalyst for the Suzuki–Miyaura reaction of potassium aryltrifluoroborates. *Journal of Molecular Catalysis A: Chemical* **404**, 1-7 (2015); published online Epub2015/08/01/
(<http://dx.doi.org/10.1016/j.molcata.2015.03.022>).
98. H. Wang, T. Maiyalagan, X. Wang, Review on Recent Progress in Nitrogen-Doped Graphene: Synthesis, Characterization, and Its Potential Applications. *ACS Catalysis* **2**, 781-794 (2012); published online Epub2012/05/04 (10.1021/cs200652y).
99. A. Ishii, M. Yamamoto, H. Asano, K. Fujiwara, DFT calculation for adatom adsorption on graphene sheet as a prototype of carbon nanotube functionalization. *Journal of Physics: Conference Series* **100**, 052087 (2008).
100. F. Banhart, J. Kotakoski, A. V. Krasheninnikov, Structural Defects in Graphene. *ACS Nano* **5**, 26-41 (2011); published online Epub2011/01/25 (10.1021/nn102598m).
101. E. P. Boon, L. T. Le, W. Y. Lee, Inversion of temperature–resistance relationship by enlarged structural defects in graphene oxide. *Carbon* **102**, 81-85 (2016); published online Epub2016/06/01/ (<http://dx.doi.org/10.1016/j.carbon.2016.02.010>).

102. J. P. Perdew, K. Burke, M. Ernzerhof, Generalized Gradient Approximation Made Simple. *Physical Review Letters* **77**, 3865-3868 (1996); published online Epub10/28/ (
103. G. Kresse, D. Joubert, From ultrasoft pseudopotentials to the projector augmented-wave method. *Physical Review B* **59**, 1758-1775 (1999); published online Epub01/15/ (
104. J. Harl, L. Schimka, G. Kresse, Assessing the quality of the random phase approximation for lattice constants and atomization energies of solids. *Physical Review B* **81**, 115126 (2010); published online Epub03/17/ (
105. F. Aguilera-Granja, A. Vega, J. Rogan, W. Orellana, G. García, Magnetic properties of Pd atomic clusters from different theoretical approaches. *The European Physical Journal D* **44**, 125-131 (2007); published online EpubJuly 01 (10.1140/epjd/e2007-00174-9).
106. B. Fan, G.-X. Ge, C.-H. Jiang, G.-H. Wang, J.-g. Wan, Structure and magnetic properties of icosahedral Pd_xAg_{13-x} (x = 0–13) clusters. *Scientific Reports* **7**, 9539 (2017); published online Epub2017/08/25 (10.1038/s41598-017-10184-6).
107. T. Vats, R. Gogoi, P. Gaur, A. Sharma, S. Ghosh, P. F. Siril, Pristine Graphene–Copper(II) Oxide Nanocatalyst: A Novel and Green Approach in CuAAC Reactions. *ACS Sustainable Chemistry & Engineering* **5**, 7632-7641 (2017); published online Epub2017/09/05 (10.1021/acssuschemeng.7b00960).
108. X. Wang, C. Zhu, Z. Huang, X. Hu, X. Zhu, In situ synthesis of pristine-graphene/Ag nanocomposites as highly sensitive SERS substrates. *RSC Advances* **6**, 91579-91583 (2016)10.1039/C6RA20085K).
109. X. Wang, G. Meng, C. Zhu, Z. Huang, Y. Qian, K. Sun, X. Zhu, A Generic Synthetic Approach to Large-Scale Pristine-Graphene/Metal-Nanoparticles Hybrids. *Advanced Functional Materials* **23**, 5771-5777 (2013)10.1002/adfm.201301409).

110. S. Agnoli, M. Favaro, Doping graphene with boron: a review of synthesis methods, physicochemical characterization, and emerging applications. *Journal of Materials Chemistry A* **4**, 5002-5025 (2016)10.1039/C5TA10599D).
111. R. Yadav, C. K. Dixit, Synthesis, characterization and prospective applications of nitrogen-doped graphene: A short review. *Journal of Science: Advanced Materials and Devices* **2**, 141-149 (2017); published online Epub2017/06/01/ (<https://doi.org/10.1016/j.jsamd.2017.05.007>).
112. Y. Chen, Y.-j. Liu, H.-x. Wang, J.-x. Zhao, Q.-h. Cai, X.-z. Wang, Y.-h. Ding, Silicon-Doped Graphene: An Effective and Metal-Free Catalyst for NO Reduction to N₂O? *ACS Applied Materials & Interfaces* **5**, 5994-6000 (2013); published online Epub2013/07/10 (10.1021/am400563g).
113. Y. Wang, Y. Shao, D. W. Matson, J. Li, Y. Lin, Nitrogen-Doped Graphene and Its Application in Electrochemical Biosensing. *ACS Nano* **4**, 1790-1798 (2010); published online Epub2010/04/27 (10.1021/nn100315s).
114. Y. R. Choi, Y.-G. Yoon, K. S. Choi, J. H. Kang, Y.-S. Shim, Y. H. Kim, H. J. Chang, J.-H. Lee, C. R. Park, S. Y. Kim, H. W. Jang, Role of oxygen functional groups in graphene oxide for reversible room-temperature NO₂ sensing. *Carbon* **91**, 178-187 (2015); published online Epub2015/09/01/ (<http://dx.doi.org/10.1016/j.carbon.2015.04.082>).
115. D. S. Shin, H. G. Kim, H. S. Ahn, H. Y. Jeong, Y.-J. Kim, D. Odkhuu, N. Tsogbadrakh, H.-B.-R. Lee, B. H. Kim, Distribution of oxygen functional groups of graphene oxide obtained from low-temperature atomic layer deposition of titanium oxide. *RSC Advances* **7**, 13979-13984 (2017)10.1039/C7RA00114B).

116. H. J. Han, Y. N. Chen, Z. J. Wang, Effect of microwave irradiation on reduction of graphene oxide films. *RSC Advances* **5**, 92940-92946 (2015)10.1039/C5RA19268D).
117. R. Kumar, J.-H. Oh, H.-J. Kim, J.-H. Jung, C.-H. Jung, W. G. Hong, H.-J. Kim, J.-Y. Park, I.-K. Oh, Nanohole-Structured and Palladium-Embedded 3D Porous Graphene for Ultrahigh Hydrogen Storage and CO Oxidation Multifunctionalities. *ACS Nano* **9**, 7343-7351 (2015); published online Epub2015/07/28 (10.1021/acsnano.5b02337).
118. A. A. C. Braga, G. Ujaque, F. Maseras, A DFT Study of the Full Catalytic Cycle of the Suzuki–Miyaura Cross-Coupling on a Model System. *Organometallics* **25**, 3647-3658 (2006); published online Epub2006/07/01 (10.1021/om060380i).
119. L. J. Goossen, D. Koley, H. L. Hermann, W. Thiel, The Palladium-Catalyzed Cross-Coupling Reaction of Carboxylic Anhydrides with Arylboronic Acids: A DFT Study. *Journal of the American Chemical Society* **127**, 11102-11114 (2005); published online Epub2005/08/01 (10.1021/ja052435y).
120. Y.-L. Huang, C.-M. Weng, F.-E. Hong, Density Functional Studies on Palladium-Catalyzed Suzuki–Miyaura Cross-Coupling Reactions Assisted by N- or P-Chelating Ligands. *Chemistry – A European Journal* **14**, 4426-4434 (2008)10.1002/chem.200800011).
121. M. Jakt, L. Johannissen, H. S. Rzepa, D. A. Widdowson, R. Wilhelm, A computational study of the mechanism of palladium insertion into alkynyl and aryl carbon-fluorine bonds. *Journal of the Chemical Society, Perkin Transactions 2*, 576-581 (2002)10.1039/B108727B).
122. M. Pérez-Rodríguez, A. A. C. Braga, M. Garcia-Melchor, M. H. Pérez-Temprano, J. A. Casares, G. Ujaque, A. R. de Lera, R. Álvarez, F. Maseras, P. Espinet, C–C Reductive

- Elimination in Palladium Complexes, and the Role of Coupling Additives. A DFT Study Supported by Experiment. *Journal of the American Chemical Society* **131**, 3650-3657 (2009); published online Epub2009/03/18 (10.1021/ja808036j).
123. L. K. Tímea R. Kégl, Tamás Kégl, DFT Study on the Oxidative Addition of 4-Substituted Iodobenzenes on Pd(0)-Phosphine Complexes. *Advances in Physical Chemistry* **2015**, 6 (2015)10.1155/2015/985268).
124. S. Wen-jing, C. Wei, Y. Liang-jun, J. Cheng-fa, Ligand Size Effect on PdL n Oxidative Addition with Aryl Bromide: A DFT Study. *Chinese Journal of Chemical Physics* **23**, 175 (2010).
125. S. Sabaqian, F. Nemati, H. T. Nahzomi, M. M. Heravi, Palladium acetate supported on amidoxime-functionalized magnetic cellulose: synthesis, DFT study and application in Suzuki reaction. *Carbohydrate Polymers*, (2017); published online Epub2017/08/31/ (<http://dx.doi.org/10.1016/j.carbpol.2017.08.109>).
126. R. ski, O. M. Demchuk, D. Babyuk, A Quantum-Chemical DFT Approach to Elucidation of the Chirality Transfer Mechanism of the Enantioselective Suzuki–Miyaura Cross-Coupling Reaction. *Journal of Chemistry* **2017**, 12 (2017)10.1155/2017/3617527).
127. A. A. C. Braga, N. H. Morgon, G. Ujaque, F. Maseras, Computational Characterization of the Role of the Base in the Suzuki–Miyaura Cross-Coupling Reaction. *Journal of the American Chemical Society* **127**, 9298-9307 (2005); published online Epub2005/06/01 (10.1021/ja050583i).
128. A. Sundermann, O. Uzan, J. M. L. Martin, Computational Study of a New Heck Reaction Mechanism Catalyzed by Palladium(II/IV) Species. *Chemistry – A European Journal* **7**,

- 1703-1711 (2001)10.1002/1521-3765(20010417)7:8<1703::AID-CHEM17030>3.0.CO;2-K).
129. S. Boonseng, G. W. Roffe, M. Targema, J. Spencer, H. Cox, Rationalization of the mechanism of in situ Pd(0) formation for cross-coupling reactions from novel unsymmetrical pincer palladacycles using DFT calculations. *Journal of Organometallic Chemistry* **845**, 71-81 (2017); published online Epub2017/09/15/ (<http://dx.doi.org/10.1016/j.jorganchem.2017.02.040>).
130. A. V. Gaikwad, A. Holuigue, M. B. Thathagar, J. E. ten Elshof, G. Rothenberg, Ion- and Atom-Leaching Mechanisms from Palladium Nanoparticles in Cross-Coupling Reactions. *Chemistry – A European Journal* **13**, 6908-6913 (2007)10.1002/chem.200700105).
131. H. Yan, H. Cheng, H. Yi, Y. Lin, T. Yao, C. Wang, J. Li, S. Wei, J. Lu, Single-Atom Pd1/Graphene Catalyst Achieved by Atomic Layer Deposition: Remarkable Performance in Selective Hydrogenation of 1,3-Butadiene. *Journal of the American Chemical Society* **137**, 10484-10487 (2015); published online Epub2015/08/26 (10.1021/jacs.5b06485).
132. A. Leyva-Pérez, J. Oliver-Meseguer, P. Rubio-Marqués, A. Corma, Water-Stabilized Three- and Four-Atom Palladium Clusters as Highly Active Catalytic Species in Ligand-Free C–C Cross-Coupling Reactions. *Angewandte Chemie International Edition* **52**, 11554-11559 (2013)10.1002/anie.201303188).
133. M. Pérez-Lorenzo, Palladium Nanoparticles as Efficient Catalysts for Suzuki Cross-Coupling Reactions. *The Journal of Physical Chemistry Letters* **3**, 167-174 (2012); published online Epub2012/01/19 (10.1021/jz2013984).

134. Y. Yang, C. E. Castano, B. F. Gupton, A. C. Reber, S. N. Khanna, A fundamental analysis of enhanced cross-coupling catalytic activity for palladium clusters on graphene supports. *Nanoscale* **8**, 19564-19572 (2016)10.1039/C6NR06793J).
135. M. Liu, R. Zhang, W. Chen, Graphene-Supported Nanoelectrocatalysts for Fuel Cells: Synthesis, Properties, and Applications. *Chemical Reviews* **114**, 5117-5160 (2014); published online Epub2014/05/28 (10.1021/cr400523y).
136. A. Balanta, C. Godard, C. Claver, Pd nanoparticles for C-C coupling reactions. *Chemical Society Reviews* **40**, 4973-4985 (2011)10.1039/C1CS15195A).
137. A. Fürstner, A. Leitner, M. Méndez, H. Krause, Iron-Catalyzed Cross-Coupling Reactions. *Journal of the American Chemical Society* **124**, 13856-13863 (2002); published online Epub2002/11/01 (10.1021/ja027190t).
138. T. Hatakeyama, T. Hashimoto, K. K. A. D. S. Kathriarachchi, T. Zenmyo, H. Seike, M. Nakamura, Iron-Catalyzed Alkyl-Alkyl Suzuki-Miyaura Coupling. *Angewandte Chemie International Edition* **51**, 8834-8837 (2012)10.1002/anie.201202797).
139. S. D. Ramgren, L. Hie, Y. Ye, N. K. Garg, Nickel-Catalyzed Suzuki-Miyaura Couplings in Green Solvents. *Organic Letters* **15**, 3950-3953 (2013); published online Epub2013/08/02 (10.1021/ol401727y).
140. B. M. Rosen, K. W. Quasdorf, D. A. Wilson, N. Zhang, A.-M. Resmerita, N. K. Garg, V. Percec, Nickel-Catalyzed Cross-Couplings Involving Carbon-Oxygen Bonds. *Chemical Reviews* **111**, 1346-1416 (2011); published online Epub2011/03/09 (10.1021/cr100259t).
141. S. K. Gurung, S. Thapa, A. Kafle, D. A. Dickie, R. Giri, Copper-Catalyzed Suzuki-Miyaura Coupling of Arylboronate Esters: Transmetalation with (PN)CuF and

- Identification of Intermediates. *Organic Letters* **16**, 1264-1267 (2014); published online Epub2014/02/21 (10.1021/o1500310u).
142. Y.-Y. Sun, J. Yi, X. Lu, Z.-Q. Zhang, B. Xiao, Y. Fu, Cu-Catalyzed Suzuki-Miyaura reactions of primary and secondary benzyl halides with arylboronates. *Chemical Communications* **50**, 11060-11062 (2014)10.1039/C4CC05376A).
143. J. Mao, J. Guo, F. Fang, S.-J. Ji, Highly efficient copper(0)-catalyzed Suzuki–Miyaura cross-coupling reactions in reusable PEG-400. *Tetrahedron* **64**, 3905-3911 (2008); published online Epub2008/04/28/ (<http://dx.doi.org/10.1016/j.tet.2008.02.068>).
144. M. Baghbanzadeh, C. Pilger, C. O. Kappe, Rapid Nickel-Catalyzed Suzuki–Miyaura Cross-Couplings of Aryl Carbamates and Sulfamates Utilizing Microwave Heating. *The Journal of Organic Chemistry* **76**, 1507-1510 (2011); published online Epub2011/03/04 (10.1021/jo1024464).
145. N. A. Weires, E. L. Baker, N. K. Garg, Nickel-catalysed Suzuki–Miyaura coupling of amides. *Nat Chem* **8**, 75-79 (2016); published online Epub01//print (10.1038/nchem.2388 <http://www.nature.com/nchem//journal/v8/n1/abs/nchem.2388.html#supplementary-information>).
146. S. Xu, E. H. Kim, A. Wei, E.-i. Negishi, Pd- and Ni-catalyzed cross-coupling reactions in the synthesis of organic electronic materials. *Science and Technology of Advanced Materials* **15**, 044201 (2014); published online Epub2014/08/01 (10.1088/1468-6996/15/4/044201).
147. M. Tobisu, T. Xu, T. Shimasaki, N. Chatani, Nickel-Catalyzed Suzuki–Miyaura Reaction of Aryl Fluorides. *Journal of the American Chemical Society* **133**, 19505-19511 (2011); published online Epub2011/12/07 (10.1021/ja207759e).

148. B. H. Lipshutz, B. A. Frieman, C.-T. Lee, A. Lower, D. M. Nihan, B. R. Taft, Microwave-Assisted Heterogeneous Cross-Coupling Reactions Catalyzed by Nickel-in-Charcoal (Ni/C). *Chemistry – An Asian Journal* **1**, 417-429 (2006)10.1002/asia.200600031).
149. K. Bhowmik, D. Sengupta, B. Basu, G. De, Reduced graphene oxide supported Ni nanoparticles: a high performance reusable heterogeneous catalyst for Kumada-Corriu cross-coupling reactions. *RSC Advances* **4**, 35442-35448 (2014)10.1039/C4RA04834B).
150. Y. Zhong, X. Gong, X. Zhu, Z. Ni, H. Wang, J. Fu, W. Han, In situ generated nickel nanoparticle-catalyzed carbonylative Suzuki reactions of aryl iodides with arylboronic acids at ambient CO pressure in poly(ethylene glycol). *RSC Advances* **4**, 63216-63220 (2014)10.1039/C4RA10739J).
151. S. Handa, E. D. Slack, B. H. Lipshutz, Nanonickel-Catalyzed Suzuki–Miyaura Cross-Couplings in Water. *Angewandte Chemie International Edition* **54**, 11994-11998 (2015)10.1002/anie.201505136).
152. E. A. Standley, T. F. Jamison, Simplifying Nickel(0) Catalysis: An Air-Stable Nickel Precatalyst for the Internally Selective Benzylolation of Terminal Alkenes. *Journal of the American Chemical Society* **135**, 1585-1592 (2013); published online Epub2013/01/30 (10.1021/ja3116718).
153. T. Schaub, M. Backes, U. Radius, Nickel(0) Complexes of N-Alkyl-Substituted N-Heterocyclic Carbenes and Their Use in the Catalytic Carbon–Carbon Bond Activation of Biphenylene. *Organometallics* **25**, 4196-4206 (2006); published online Epub2006/08/01 (10.1021/om0604223).

154. J. Magano, S. Monfette, Development of an Air-Stable, Broadly Applicable Nickel Source for Nickel-Catalyzed Cross-Coupling. *ACS Catalysis* **5**, 3120-3123 (2015); published online Epub2015/05/01 (10.1021/acscatal.5b00498).
155. N. A. Weires, D. D. Caspi, N. K. Garg, Kinetic Modeling of the Nickel-Catalyzed Esterification of Amides. *ACS Catalysis* **7**, 4381-4385 (2017); published online Epub2017/07/07 (10.1021/acscatal.7b01444).
156. R. Miyakoshi, K. Shimono, A. Yokoyama, T. Yokozawa, Catalyst-Transfer Polycondensation for the Synthesis of Poly(p-phenylene) with Controlled Molecular Weight and Low Polydispersity. *Journal of the American Chemical Society* **128**, 16012-16013 (2006); published online Epub2006/12/01 (10.1021/ja067107s).
157. C. A. Tolman, W. C. Seidel, D. H. Gerlach, Triarylphosphine and ethylene complexes of zerovalent nickel, palladium, and platinum. *Journal of the American Chemical Society* **94**, 2669-2676 (1972); published online Epub1972/04/01 (10.1021/ja00763a019).
158. A. F. Littke, G. C. Fu, Palladium-Catalyzed Coupling Reactions of Aryl Chlorides. *Angewandte Chemie International Edition* **41**, 4176-4211 (2002)10.1002/1521-3773(20021115)41:22<4176::AID-ANIE4176>3.0.CO;2-U).
159. D.-G. Yu, B.-J. Li, S.-F. Zheng, B.-T. Guan, B.-Q. Wang, Z.-J. Shi, Direct Application of Phenolic Salts to Nickel-Catalyzed Cross-Coupling Reactions with Aryl Grignard Reagents. *Angewandte Chemie International Edition* **49**, 4566-4570 (2010)10.1002/anie.200907359).
160. F. Schoenebeck, K. N. Houk, Ligand-Controlled Regioselectivity in Palladium-Catalyzed Cross Coupling Reactions. *Journal of the American Chemical Society* **132**, 2496-2497 (2010); published online Epub2010/03/03 (10.1021/ja9077528).

161. A. Kumbhar, Functionalized nitrogen ligands for palladium catalyzed cross-coupling reactions (part I). *Journal of Organometallic Chemistry* **848**, 22-88 (2017); published online Epub2017/10/15/ (<https://doi.org/10.1016/j.jorganchem.2017.07.009>).
162. T. Brenstrum, J. Clattenburg, J. Britten, S. Zavorine, J. Dyck, A. J. Robertson, J. McNulty, A. Capretta, Phosphorinanes as Ligands for Palladium-Catalyzed Cross-Coupling Chemistry. *Organic Letters* **8**, 103-105 (2006); published online Epub2006/01/01 (10.1021/ol052579h).
163. D. S. Surry, S. L. Buchwald, Biaryl Phosphane Ligands in Palladium-Catalyzed Amination. *Angewandte Chemie International Edition* **47**, 6338-6361 (2008)10.1002/anie.200800497).
164. B. J. Stokes, S. M. Opra, M. S. Sigman, Palladium-Catalyzed Allylic Cross-Coupling Reactions of Primary and Secondary Homoallylic Electrophiles. *Journal of the American Chemical Society* **134**, 11408-11411 (2012); published online Epub2012/07/18 (10.1021/ja305403s).
165. D. S. Surry, S. L. Buchwald, Dialkylbiaryl phosphines in Pd-catalyzed amination: a user's guide. *Chemical Science* **2**, 27-50 (2011)10.1039/C0SC00331J).
166. R. Martin, S. L. Buchwald, Palladium-Catalyzed Suzuki–Miyaura Cross-Coupling Reactions Employing Dialkylbiaryl Phosphine Ligands. *Accounts of Chemical Research* **41**, 1461-1473 (2008); published online Epub2008/11/18 (10.1021/ar800036s).
167. A. F. Schmidt, A. A. Kurokhtina, A. N. Svechkarev, V. V. Smirnov, A. Al-Halqiqa, Problems of distinguishing the homogeneous and heterogeneous mechanisms of the Suzuki reaction. *Kinetics and Catalysis* **51**, 113-118 (2010); published online EpubFebruary 01 (10.1134/s0023158410010180).

168. P. Wang, Q. Lu, J. Li, In situ Formation of Palladium Nanoparticles Inside the Pore Channels of Ordered Mesoporous Silica. *Catalysis Letters* **131**, 444-450 (2009)10.1007/s10562-009-9892-3).
169. P. J. Ellis, I. J. S. Fairlamb, S. F. J. Hackett, K. Wilson, A. F. Lee, Evidence for the Surface-Catalyzed Suzuki–Miyaura Reaction over Palladium Nanoparticles: An Operando XAS Study. *Angewandte Chemie International Edition* **49**, 1820-1824 (2010)10.1002/anie.200906675).
170. J. D. Jason, H. Yuki, Mechanistic studies of AFM probe-driven Suzuki and Heck molecular coupling. *Nanotechnology* **21**, 265302 (2010).
171. S. Li, J. Wang, Y. Kou, S. Zhang, Ionic-Liquid-Grafted Rigid Poly(p-Phenylene) Microspheres: Efficient Heterogeneous Media for Metal Scavenging and Catalysis. *Chemistry – A European Journal* **16**, 1812-1818 (2010)10.1002/chem.200902495).
172. M. Pagliaro, V. Pandarus, R. Ciriminna, F. Béland, P. Demma Carà, Heterogeneous versus Homogeneous Palladium Catalysts for Cross-Coupling Reactions. *ChemCatChem* **4**, 432-445 (2012)10.1002/cctc.201100422).
173. A. F. Schmidt, A. A. Kurokhtina, Distinguishing between the homogeneous and heterogeneous mechanisms of catalysis in the Mizoroki-Heck and Suzuki-Miyaura reactions: Problems and prospects. *Kinetics and Catalysis* **53**, 714-730 (2012)10.1134/s0023158412060109).
174. S. Mukhopadhyay, G. Rothenberg, D. Gitis, H. Wiener, Y. Sasson, Kinetics and mechanism of heterogeneous palladium-catalyzed coupling reactions of chloroaryls in water. *Journal of the Chemical Society, Perkin Transactions 2*, 2481-2484 (1999)10.1039/A905625D).

175. N. T. S. Phan, M. Van Der Sluys, C. W. Jones, On the Nature of the Active Species in Palladium Catalyzed Mizoroki–Heck and Suzuki–Miyaura Couplings – Homogeneous or Heterogeneous Catalysis, A Critical Review. *Advanced Synthesis & Catalysis* **348**, 609-679 (2006)10.1002/adsc.200505473).
176. F. Proutiere, F. Schoenebeck, Solvent Effect on Palladium-Catalyzed Cross-Coupling Reactions and Implications on the Active Catalytic Species. *Angewandte Chemie International Edition* **50**, 8192-8195 (2011)10.1002/anie.201101746).
177. C. Amatore, A. Jutand, G. Le Duc, Kinetic Data for the Transmetalation/Reductive Elimination in Palladium-Catalyzed Suzuki–Miyaura Reactions: Unexpected Triple Role of Hydroxide Ions Used as Base. *Chemistry – A European Journal* **17**, 2492-2503 (2011)10.1002/chem.201001911).
178. S. Lambert, N. Job, L. D'Souza, M. F. R. Pereira, R. Pirard, B. Heinrichs, J. L. Figueiredo, J.-P. Pirard, J. R. Regalbuto, Synthesis of very highly dispersed platinum catalysts supported on carbon xerogels by the strong electrostatic adsorption method. *Journal of Catalysis* **261**, 23-33 (2009); published online Epub2009/01/01/ (<https://doi.org/10.1016/j.jcat.2008.10.014>).
179. L. D'Souza, J. R. Regalbuto, in *Studies in Surface Science and Catalysis*, E. M. Gaigneaux, M. Devillers, S. Hermans, P. A. Jacobs, J. A. Martens, P. Ruiz, Eds. (Elsevier, 2010), vol. 175, pp. 715-718.
180. L. Jiao, J. R. Regalbuto, The synthesis of highly dispersed noble and base metals on silica via strong electrostatic adsorption: I. Amorphous silica. *Journal of Catalysis* **260**, 329-341 (2008); published online Epub2008/12/10/ (<https://doi.org/10.1016/j.jcat.2008.09.022>).

181. D. Voiry, J. Yang, J. Kupferberg, R. Fullon, C. Lee, H. Y. Jeong, H. S. Shin, M. Chhowalla, High-quality graphene via microwave reduction of solution-exfoliated graphene oxide. *Science* **353**, 1413-1416 (2016)10.1126/science.aah3398).
182. J. Rebek, F. Gavina, Three-phase test. Detection of free cyclobutadiene. *Journal of the American Chemical Society* **97**, 3453-3456 (1975); published online Epub1975/06/01 (10.1021/ja00845a029).
183. J. Rebek, D. Brown, S. Zimmerman, Three-phase test for reaction intermediates. Nucleophilic catalysis and elimination reactions. *Journal of the American Chemical Society* **97**, 454-455 (1975); published online Epub1975/01/01 (10.1021/ja00835a057).
184. H. Gruber-Woelfler, P. F. Radaschitz, P. W. Feenstra, W. Haas, J. G. Khinast, Synthesis, catalytic activity, and leaching studies of a heterogeneous Pd-catalyst including an immobilized bis(oxazoline) ligand. *Journal of Catalysis* **286**, 30-40 (2012); published online Epub2012/02/01/ (<https://doi.org/10.1016/j.jcat.2011.10.013>).
185. G. Wang, X. Shen, J. Yao, J. Park, Graphene nanosheets for enhanced lithium storage in lithium ion batteries. *Carbon* **47**, 2049-2053 (2009); published online Epub2009/07/01/ (<https://doi.org/10.1016/j.carbon.2009.03.053>).
186. F. Kokai, R. Sorin, H. Chigusa, K. Hanai, A. Koshio, M. Ishihara, Y. Koga, M. Hasegawa, N. Imanishi, Y. Takeda, Ultrasonication fabrication of high quality multilayer graphene flakes and their characterization as anodes for lithium ion batteries. *Diamond and Related Materials* **29**, 63-68 (2012); published online Epub2012/09/01/ (<https://doi.org/10.1016/j.diamond.2012.07.011>).
187. S. S. Lee, Y.-S. Byoun, S.-H. Jeong, Y. M. Kim, H. Gil, B.-Y. Min, M. H. Seong, E. S. Jang, J.-W. Kim, Type and cause of liver disease in Korea: single-center experience, 2005-

2010. *Clin Mol Hepatol* **18**, 309-315 (2012); published online Epub9 (10.3350/cmh.2012.18.3.309).
188. Y. Zou, J. Kan, Y. Wang, Fe₂O₃-Graphene Rice-on-Sheet Nanocomposite for High and Fast Lithium Ion Storage. *The Journal of Physical Chemistry C* **115**, 20747-20753 (2011); published online Epub2011/10/27 (10.1021/jp206876t).